SENSOR PLACEMENT OPTIMIZATION UNDER UNCERTAINTY FOR STRUCTURAL HEALTH MONITORING SYSTEMS OF HOT AEROSPACE STRUCTURES

By

Robert Frank Guratzsch

Dissertation

Submitted to the Faculty of the

Graduate School of Vanderbilt University

in partial fulfillment of the requirements

for the degree of

DOCTOR OF PHILOSOPHY

in

Civil Engineering

May, 2007

Nashville, Tennessee

Approved:

Professor Sankaran Mahadevan

Professor Gautam Biswas

Professor Mark Ellingham

Professor Prodyot K. Basu

To my infinitely supportive parents: Frank and Elke Guratzsch

ACKNOWLEDGEMENTS

It is with great sincerity that I thank my mentor and advisor – Dr. Sankaran Mahadevan – for his constant support throughout my career at Vanderbilt University. I thank him for his encouragement, constructive criticism, and belief in my abilities. I thank him especially for his patience during the countless hours we spent working together. I also wish to thank the members of my committee, Dr. P.K. Basu, Dr. Gautam Biswas, and Dr. Mark Ellingham, for their advice and great attitude toward working with me.

This research is supported by the National Science Foundation through funding of the Integrative Graduate Education, Research, and Training (IGERT) Program, and by the Air Force Research Laboratory (AFRL) at Wright Patterson Air Force Base through subcontract to Anteon Corporation. Special thanks are given to Dr. Sankaran Mahadevan, Dr. Chris Pettit and Mark Derriso for initiating this project and assuring continued progress.

Thanks also go to Dr. Martin DeSimio, Dr. Steven Olson, Kevin Brown, and Todd Bussey, of AFRL, for their mentoring, technical support, and great wisdom on the subjects at hand.

I am grateful to all of those with whom I had the pleasure to work during my time at Vanderbilt University. Especially, Yongming Liu, Kenneth "Nedster" Mitchel, Candice Griffith, John McFarland, Alan Tackett, Hugo Valle, and all members of the Reliability and Risk Engineering and Management IGERT Program, as well as the supporting staff of the Civil and Environmental Engineering Department.

I would like to sincerely thank my family, friends, and loved ones. Without the endearing support of mom and dad, I might not have conquered this. And finally, I would like to thank my wife, Joana, for giving me a reason to finish.

TABLE OF CONTENTS

Page

DEDICATION iii

ACKNOWLEDGEMENTS iv

LIST OF TABLES vii

LIST OF FIGURES ix

Chapter

I. INTRODUCTION 1

1.1 Overview 1
1.2 Research Objectives 3
1.3 General Methodology 4
1.3.1 Structural Simulation and Probabilistic Analysis 5
1.3.2 Stochastic Finite Element Model Validation 5
1.3.3 Damage Detection 6
1.3.4 Sensor Layout Performance Prediction Validation 7
1.3.5 Sensor Placement Optimization 7
1.4 Test Article 7
1.5 Dissertation Outline 9

II. STRUCTURAL SIMULATION AND PROBABILISTIC ANALYSIS 11

2.1 Finite Element Method 11
2.2 Stochastic Finite Element Analysis 14

III. VALIDATION ASSESSMENT OF SFEM 23

3.1 Introduction 23
3.2 Model Validation Metrics 25
3.2.1 Modal Assurance Criterion 25
3.2.2 Model Reliability Metric 26
3.2.3 Classical and Bayesian Hypothesis Testing 27
3.3 Modal Analysis 28
3.4 Model Calibration 38
3.4.1 Modal Comparison 41
3.4.2 Model Reliability Metric 44
3.4.3 Joint-MRM via Bootstrapping 50
3.4.4 Classical and Bayesian Hypothesis Testing 54

3.4.5 Conclusions 55
3.5 Independent Model Validation 56
3.6 Validation Conclusions 61

IV. SHM SENSORS AND DAMAGE DETECTION 65

4.1 Sensors 65
4.2 Damage Detection 67
4.3 Sensor Layout Performance Measures 68
4.4 Signal Analysis, Feature Extraction, and State Classification 72
4.4.1 Introduction to Feature Extraction 72
4.4.2 Introduction to Feature Selection 76
4.4.3 Introduction to State Classification 78
4.4.4 Additional Signal Processing 82
4.4.5 Evaluation of Damage Detection Methods 83
4.5 Applied Damage Detection Methodology 97

V. VALIDATION ASSESSMENT OF SENSOR LAYOUT PERFORMANCE PREDICTION 101

5.1 Introduction 101
5.2 Experimental Observations 104
5.3 Methodology Validation 107
5.3.1 Comparison and Correlation 108
5.3.2 Model Reliability Metric 110
5.3.3 Classical and Bayesian Hypothesis Tests and Confidence Bounds 115
5.3.4 Multivariate Validation via Bootstrapping 119
5.3.5 Validation Assessment Inferences 122
5.4 Comparison of Predicted and Observed Displacement Response 123
5.5 Conclusions 128

VI. SENSOR PLACEMENT OPTIMIZATION 130

6.1 Introduction 130
6.2 Investigation of Performance Measure Variability 133
6.3 Snobfit Method 137
6.4 Sensor Placement Optimization Method 142
6.5 SPO Results 144

VII. SENSOR SENSITIVITY, RELIABILITY, REDUNDANCY 148

VIII. SUMMARY, CONCLUSIONS, AND FUTURE WORK 153

8.1 Conclusions 155
8.2 Future Work 158

REFERENCES 162

LIST OF TABLES

Table Page

1. Mean and COV values used for random field simulation..... 18
2. EMA modal frequency results (Hz). 31
3. EMA-based mean mode shape vectors for healthy model..... 32
4. FEM-based modal analysis results..... 34
5. FEM-based mode shape vectors for healthy model. 35
6. Model discretization error quantification..... 39
7. MAC matrix for the healthy model. 43
8. MRM for modal frequencies of damaged test article. 44
9. MRM for modal frequencies of healthy test article. 47
10. MRM for mode shape vectors of healthy test article. 48
11. MRM for mode shape vectors of healthy test article. 49
12. Hypothesis test results of calibrated model prediction-observation comparison..... 54
13. Independent EMA modal frequency results (Hz). 57
14. Mean mode shape vectors of independent EMA of healthy and damaged test article. 57
15. Natural frequencies via Blevins' formulation (Hz). 57
16. MAC matrix for the healthy model for validation of SFEMs. 59
17. MRM for validation of modal frequencies of the healthy test article. 60
18. MRM for validation of modal frequencies of the damaged test article. 60
19. Classical hypothesis test results for model validation. 61
20. Sample classification matrix for a given sensor layout. 69
21. Randomly selected sensor layouts shown in Figure 23. 71
22. Summary of DDM definitions and combinations. 86

23. Probability of false alarm for various DDM for sensor layouts of Table 21. 87

24. Probability of missed detection for various DDM for sensor layouts of Table 21. 89

25. Probability of correct classification for various DDM for sensor layouts of Table 21. 90

26. Performance measures corresponding to randomly selected sensor layouts of Table 21. 99

27. Results: predicted performance measures corresponding to seven different sensor layouts. 105

28. Performance measures corresponding to sensor arrays of Table 27. 107

29. Trend lines and coefficient of determination. 108

30. MAC values for seven sets of performance measures. 108

31. Geometric distance between seven performance measure vectors. 109

32. Results of random partitioning of analytically predicted data set. 110

33. Results: hypothesis test via Student's *t*-statistic. 118

34. Results: Bayes' Factor. 119

35. Correlation coefficients of performance measures. 121

36. Central moments of autocorrelation and PSD. 126

37. Results: optimal sensor arrays for various objective functions. 145

LIST OF FIGURES

Figure Page

1. TPS test article; a) photograph[11], b) schematic. 9
2. Finite element model of TPS test article. 12
3. Piezoelectric actuator with force excitation at nodes. 13
4. A realization of a random process via Shinozuka's formulation. 16
5. Sample realization of random field for plate thickness. 17
6. Healthy simulated structural response for two realizations of the random model inputs. 21
7. Damaged simulated structural response for two realizations of the random model inputs. 22
8. EMA test layout. 29
9. Curve fitting FRF measurements.[56] 30
10. EMA mode shape results. 33
11. Analytically determined mode shapes for healthy test article. 36
12. Analytically determined and superimposed mode shapes for coupled modes. 36
13. Analytically determined mode shapes for damaged test article 37
14. Plots of correlated mode pairs (axes show frequency - Hz). 42
15. Natural frequency difference diagrams. 43
16. Bootstrap MRM for modal frequencies of damaged test article. 51
17. Bootstrap MRM for modal frequencies of healthy test article. 51
18. Bootstrap MRM for uncoupled mode shape vectors of healthy test article. 53
19. Bootstrap MRM for coupled mode shape vectors of healthy test article. 53
20. Plots of correlated mode pairs for validation of SFEM (axes show frequency - Hz). 59
21. General comparison of predictions (P), first set of observations (1st), and second set of observations (2nd) for modes of vibration 1, 2, and 3. Natural frequencies are shown along the vertical axis in Hz. 62

22. General comparison of predictions (P), first set of observations (1^{st}), and second set of observations (2^{nd}) for modes of vibration 4, 5, and 6. Natural frequencies are shown along the vertical axis in Hz. 63

23. Five randomly selected sensor layouts. 71

24. Optimal number of features to search for via SFS vs. DDM performance. 93

25. N_{opt} vs. P(Correct Classification) for DDM 3a. 94

26. Order of regression model vs. performance criteria. 95

27. N_{order} vs. performance metrics for DDM 5b. 95

28. Propagation of error and uncertainty through general SPO methodology. 102

29. Sensor layout performance prediction methodology. 103

30. Experimental SHM and data acquisition systems as applied to test article. 105

31. MRM vs. ε for P(CC) performance measure. 111

32. MRM vs. ε for P(FA) performance measure. 112

33. MRM vs. ε for P(MD) performance measure. 113

34. Graphical comparison of confidence bounds corresponding to P(CC). 116

35. Graphical comparison of confidence bounds corresponding to P(FA). 116

36. Graphical comparison of confidence bounds corresponding to P(MD). 117

37. MRM vs. ε for joint MRM of performance measures. 120

38. Healthy observed structural response for two measurements. 124

39. Healthy simulated structural response for two realizations of the random model inputs. 124

40. Autocorrelation of analytical prediction and experimental observation. 126

41. PSD of analytical prediction and experimental observation. 126

42. Performance measures versus sensor S2 location (X1, X2). 135

43. Multi-objective performance measures versus sensor S2 location (X1, X2). 136

44. Optimal sensor arrays corresponding to different objective functions. 146

45. Graphical presentation of SPO under uncertainty for SHM systems methodology. 154

46. Laboratory setup of realistic TPS panel and sensor layout. a) schematic; b) photograph[9]... 159

47. Realistic TPS component model. 160

CHAPTER I

INTRODUCTION

1.1 Overview

Next generation flight vehicles will fly higher, faster, and for longer periods of time and will therefore be subjected to much more extreme and uncertain maneuvers and environments. The application of non-destructive testing and evaluation methods for the inspection of these advanced flight structures contributes greatly to their safety and reliability; however, current forms of inspections significantly increase the operational expense, while rendering much of the fleet useless, due to the required labor-intensive dismantling of the flight vehicle. Additionally, current methods are subjective and highly dependent on the condition of inspectors as well as the inspection environment. Therefore in order to meet the demanding goals of increasing flight vehicle safety, reliability, and availability while reducing vehicle-operating costs, the technology development of structural health monitoring (SHM) systems is ongoing. Health monitoring systems that report in real-time any adverse changes in the integrity of the flight vehicle in terms of loads, reactions, stresses, strains, and displacements are central to this development.[1] Such sensing systems will minimize the requirement for costly inspections and focus maintenance to specific vehicle areas where damage was indicated and reported by the SHM system.[2] Condition-based instead of schedule-based, maintenance can then be performed, yielding faster turn-around times and much more efficient vehicle utilization. Additional cost savings will be seen through the replacement of system components due to their impending failure, rather than due to a scheduled replacement. Subjectivity will also be reduced due to the fact that

quantitative damage detection algorithms for SHM systems are more objective than human inspection procedures.[3]

A generally implemented, global, online SHM system has the advantage of producing health reports not just for any one individual vehicle, but for the fleet as a whole and will allow owners, operators, and maintenance crews to move from forensics to diagnostics and onto prognostics.[4] Forensics allows the pilot to know the condition of the flight vehicle at the point in time the inspection was performed. Since then critical maneuvers may have inflicted damage to the structure. Diagnostics of the structure via an online SHM system provides the flight crew with a real-time update on the system's health status. Prognostics takes this idea one step further, by generating forecasts of how many more flight hours, maneuvers, or missions the vehicle can endure. The bottom line of an implemented comprehensive SHM system is improved safety, increased reliability, and a much more effective maintenance program through condition-based asset management.[5]

Given these SHM system performance requirements and their impending benefits, it is easily seen that the SHM system must be the most reliable subsystem on board the flight structure and provide dependable and consistent inferences about the structural condition. This requires that the SHM system be designed optimally not just in terms of minimizing the weight and impact that the SHM system has on the flight structure, but also in terms of maximizing the probability that the SHM system will be able to reliably detect damage before it turns critical with sufficiently low false alarm and missed detection error rates. Due to the fact that the SHM systems are to be installed in *next* generation flight structures that are currently still in the developmental stage, finite element methods are utilized for their development via model-based design methodologies. The inclusion of uncertainties associated with the geometry, loads, and

material properties within a probabilistic finite element analysis framework is vital towards the success of a robust optimal SHM system design. The proposed methodology for optimal sensor placement of SHM systems includes design parameter uncertainty.

1.2 Research Objectives

Methodology development for optimizing the sensor layout design of SHM systems under uncertainty is the objective of this research. The optimal placement of SHM system sensors in order to detect with high probability and reliability any damage before it becomes critical is the specific goal of this study. In order to minimally affect the flight structure's design via the addition of an SHM system, the number of sensors comprising the SHM system must be held small while simultaneously maximizing the probability of being able to detect any damage before it negatively affects the operation of the flight structure. This study develops a methodology to address these issues, by integrating finite element analysis under various mechanical loading scenarios, uncertainty quantification methods for the inclusion of the stochastic nature of all model input parameters, damage detection methods and optimization algorithms. Additional project objectives consist of addressing the sensitivity of the sensor system to environmental variations and validating the basic probabilistic finite element model as well as the sensor layout performance estimation method with experimental data. The robustness of the methodology is critical towards its implementation into next generation flight vehicles; therefore, a thorough investigation of damage detection schemes used for SHM is included to identify the most robust/effective algorithm from a candidate pool of methods. Thus the proposed objectives are:

1. Stochastic finite element analysis: Integrate uncertainty quantification methods with transient finite element analysis in order to estimate response variability. Incorporate spatial variability of material and geometric parameters through random process and field simulation techniques.
2. Damage detection: Integrate advanced signal processing, feature extraction, feature selection, and state classification schemes to distinguish damaged structures from healthy ones and classify them according to their damage state.
3. Model validation: Quantitatively assess the validity of the basic stochastic finite element model (Objective 1) and the sensor layout performance prediction methodology (Objective 2) via several validation metrics, such as the modal assurance criterion, classical and Bayesian hypothesis tests, and the model reliability metric.
4. Sensor placement optimization: Optimize under uncertainty the sensor configuration for a prototype thermal protection system component with respect to probabilistic performance measures.
5. Sensitivity, reliability, and redundancy: Investigate the effects of issues, such as sensor sensitivity, reliability, and redundancy within the general SPO under uncertainty methodology.

1.3 General Methodology

The proposed methodology for optimal SHM sensor layout design under uncertainty includes the following components: (1) structural simulation, (2) probabilistic analyses, (3) damage detection, and (4) sensor placement optimization (SPO). The proposed methodology integrates these individual disciplines with effectiveness and efficiency taken into account.

1.3.1 Structural Simulation and Probabilistic Analysis

For most realistic structures, the response due to various loads cannot be determined via a closed-form function of the input variables. The response of the structure under consideration must be computed through numerical procedures such as a finite element method (FEM). Several finite element software packages are available; Ansys Release 9.0[6] is utilized in this study. Care must be taken to assure that structural models and their corresponding simulations capture all physical phenomena and include all relevant input parameters. The appropriate analysis may include linear, nonlinear, and/or coupled structural-thermal simulations. A transient mode superposition analysis is used to evaluate the FEM simulations in this study.

Structural model parameters such as distributed loads and material and geometric properties have temporal and spatial variability. Probabilistic FEM analyses, of analytical models incorporate this uncertainty via the substitution of discretized simulated random processes and fields as model input parameters. Random process/field simulation is a key step in probabilistic finite element analysis. Once the model input parameters are randomly generated via the discretization of random processes/fields and applied as inputs to FEM models, repeated simulations of the stochastic finite element model (SFEM) at each realization are used to generate statistical and/or sensitivity information on model outputs.

1.3.2 Stochastic Finite Element Model Validation

Model calibration, verification, and validation are of extreme importance before employing the model results in subsequent procedures such as damage detection and sensor layout optimization. Validation of numerical models by comparison of model predictions against experimental observations has to account for errors and uncertainties in both the predictions and the measured

observations. Several validation metrics are available to asses the predictive capability of models. It should be noted that model calibration may be necessary to achieve good agreement between model predictions and experimental observations.

1.3.3 Damage Detection

From the calibrated and validated probabilistic FEM analysis the statistics of model outputs such as the stresses, strains, and deformations are calculated. Additional analysis is needed to estimate performance measures such as the probability of correctly identifying the structural state of a component for a given sensor layout. This can be accomplished via any appropriate diagnostics signal analysis procedure (i.e. damage detection algorithm). Most structural damage detection methods and algorithms examine the changes in the measured structural vibration response and analyze the modal frequencies, mode shapes, and flexibility/stiffness coefficients of the structure.[7] The signal analysis procedure employed in this study follows the general concepts of Duda, Hart, and Stork[8] and utilizes the feature extraction and state classification methodologies defined by DeSimio, et al.[9] Repeated analyses using different realizations of the random inputs to healthy and damaged structural FEM models and state classification of their respective outputs, allows the construction of a classification matrix. Several probabilistic performance measures, such as the likelihood of correctly classifying a given realization of the SFEM output, can be estimated from the classification matrix for any given sensor layout. Combining these concepts into one algorithm yields a sensor layout performance prediction methodology.

1.3.4 Sensor Layout Performance Prediction Validation

Similar to the stochastic finite element model validation, an assessment of the predictive capabilities of the sensor layout performance prediction methodology is required prior to its utilization for sensor placement optimization. Validation metrics such as the ones utilized for model validation of the SFEM are again utilized.

1.3.5 Sensor Placement Optimization

The underlying idea of sensor placement optimization (SPO) is to identify the sensor layout, which will optimize one or more of the probabilistic performance measures. The Snobfit[10] (Stable Noisy Optimization by Branch and Fit) optimization scheme is applied for this purpose. The method is designed for bound-constrained optimization of noisy objective functions, which are costly to evaluate due to computational or experimental complexity. Snobfit iteratively constructs several globally-distributed local quadratic response surfaces of the objective function from a number of sensor configurations and their corresponding probabilistic performance measures to identify the best sensor layout.

1.4 Test Article

For the purpose of illustration, the sensor placement optimization (SPO) under uncertainty methodology for SHM systems as previously defined in Section 1.3 is implemented using the following example problem relevant to hot aerospace structures. The Air Force Research Laboratory's Air Vehicles Directorate at Wright-Patterson Air Force Base conducts research to implement integrated systems health management (ISHM) systems on future space vehicles, such as the space operations vehicle (SOV). In concept the fuselage of an SOV is covered with a

thermal protection system (TPS) consisting of a network of mechanically attached panels. If the fastening mechanism of any one such panel were to fail (e.g. lose one or more fastening bolts), the effectiveness of the SOV's fuselage TPS could become compromised, exposing the vehicle's entrails to the environment, thereby compromising vehicle integrity and ultimately jeopardizing mission safety and success. Additionally, the TPS of an SOV is its first line of defense against exposure to space debris impact, and extreme thermal loads during re-entry. Although the actual TPS concept is comprised of much more sophisticated components incorporating composite materials and highly advanced attachment mechanisms, the example problem discussed here provides a prototype SHM system to detect loose bolts on a simplified TPS component that is described in detail by Olson, et al.[11]

The test article shown in Figure 1 consists of a heat-resistant, 0.25 inch thick aluminum panel, 12 inches x 12 inches, held in place via four 0.25 inch diameter bolts located 0.50 inches from the edges of the panel. Different structural conditions are obtained by loosening one bolt at a time from the panel. The TPS panel or plate is considered healthy when all bolts are tightened to a nominal torque of 120 in-lbs. A loose bolt condition corresponding to 25% of the nominal bolt torque (30 in-lbs) represents a damaged TPS structure. There are four damaged structural states each corresponding to one of the four bolts being loose and one healthy structural state, where all four bolts are tightened to 100% nominal torque.

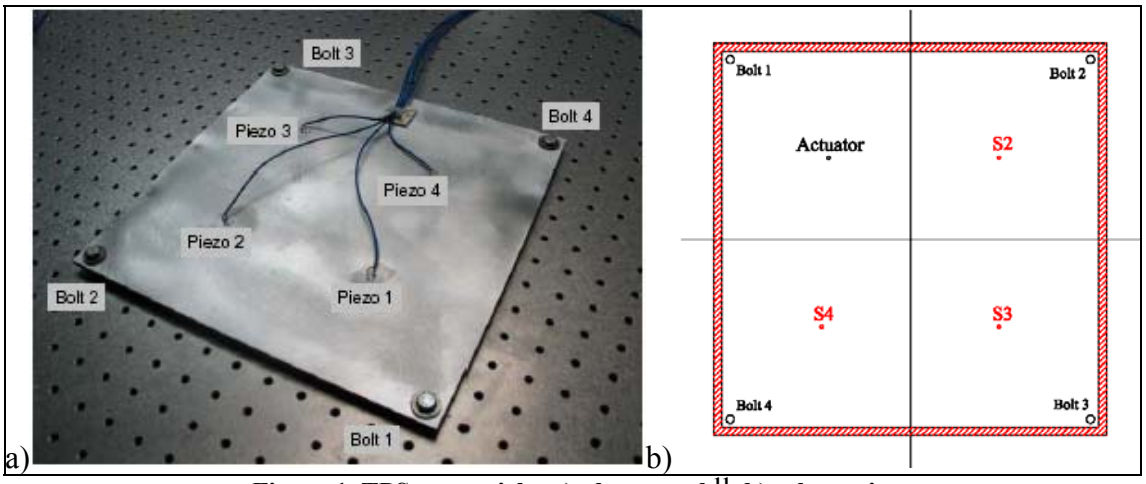

Figure 1. TPS test article; a) photograph[11], b) schematic.

Figure 1b shows a typical sensor layout, where piezoelectric sensor location 1, labeled as "Actuator," is the point of input excitation (for active SHM) and stationary, while sensor locations S2, S3, and S4 are the points of sensing and variable. Also shown in Figure 1 are the locations of the 4 bolts, which hold the test structure in place and are the locations of damage. The hatched area in Figure 1b is the region where it is infeasible to place SHM sensors.

Additionally, Derriso, Olson, and DeSimio[12,13,14,15,16] have worked on testing and modeling other SHM system components as well as compiling different damage detection and state classification schemes. Experimental work at Wright Patterson Air Force Base – where Derriso, Olson, and DeSimio are researchers – is substantially used for validation of the methods developed in this research study.

1.5 Dissertation Outline

The remainder of this dissertation follows the general structure of Section 1.3. Each chapter of this dissertation covers one particular component of the methodology and provides background, specific details, and its implementation on a prototype thermal protection system component.

The test article is described in Section 1.4. Chapter 2 discusses structural simulation and the stochastic finite element model (SFEM), while Chapter 3 provides calibration and a validation assessment thereof. Chapter 4 covers the basics of structural health monitoring starting with sensors and architectures, and investigates different damage detection schemes to identify the most efficient algorithm for this particular application. A prediction methodology for the performance of different sensor configurations is provided. Chapter 5 assesses the predictive capability of the sensor layout performance prediction methodology. Chapter 6 utilizes the performance predictions of different sensor layouts for optimization and optimizes probabilistic performance measures with respect to the location of the SHM sensors. Sensor sensitivity, reliability, and redundancy are discussed generally in Chapter 7. Chapter 8 concludes the dissertation with a brief summary and future research needs.

CHAPTER II

STRUCTURAL SIMULATION AND PROBABILISTIC ANALYSIS

This chapter is related to research Objective 1. Finite element modeling of the test article described in Section 1.4 and the inclusion of randomness in model input parameters through stochastic finite element analysis are discussed. In addition, high performance computing is introduced as a solution to computationally intensive Monte Carlo simulations of finite element models.

2.1 Finite Element Method

For most realistic structures, the response due to various loads cannot be determined via a closed-form function of the input variables, but must be computed through numerical procedures such as a finite element method (FEM). Models range from simple static analyses to complex investigations including transient analyses that incorporate dynamic thermal and mechanical loads. Due to the computational power of today's computers, high fidelity nonlinear models, which incorporate 10^6 or more degrees of freedom via elements with up to 20 nodes, are no longer considered infeasible. Several commercially available finite element software packages are Patran/Nastran/Dytran,[17,18] Ansys,[6] and Abaqus[19]. Open source codes, which can also be utilized, include CalculiX[20] and Impact.[21]

The structure under consideration as described in Section 1.4 is modeled using the commercial finite element software Ansys.[6] A portion of the FEM model is shown in Figure 2. Four-noded shell elements (Shell63) and two-noded spring elements (Combin14) are utilized to model the

aluminum plate and bolted boundary conditions. Approximately 3,300 nodes and 2,800 elements comprise the 19,836 degree of freedom (DOF) models. Five FEM models are considered: one for each structural state. In Figure 2, the four points located near the corners of the plate simulate the bolted boundary conditions via 48 spring elements per bolt location with varying stiffness coefficients. Depending on which structural state a particular model assumed, damage was simulated analytically by altering the stiffness constants of the spring elements surrounding the particular bolt location considered to be damaged. The point near the center of the upper left quadrant of the plate in Figure 2 simulates the piezoelectric actuator.

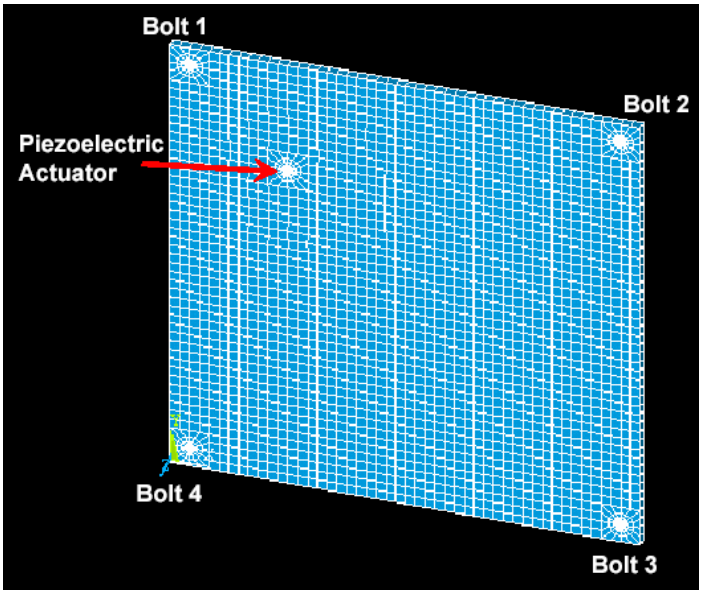

Figure 2. Finite element model of TPS test article.

The analysis is transient and includes a dynamic mechanical load consisting of a sinusoidal frequency sweep, exciting the structure from 0 to 1500 Hz over approximately 2.0 seconds. This excitation represents the auxiliary input used with active damage detection algorithms. This force excitation is applied via a simulated piezoelectric actuator at the location shown in Figure 2. The forces are in-plane and are applied radially as shown in Figure 3. It is assumed that the

actuator induced moment has a negligible effect on the plate and therefore is not included in the simulation. The sine sweep is defined as $\Delta(t) = A \cdot \sin\left(2\pi\omega_{MAX}/T \cdot t^2\right)$, where A is the amplitude, ω_{MAX} is the upper bound of the frequency sweep, and T is the time over which the sweep is to be completed. The frequency increases linearly. ω_{MAX} is equal to 1,500Hz and T is set to 2.0 seconds for this example implementation.

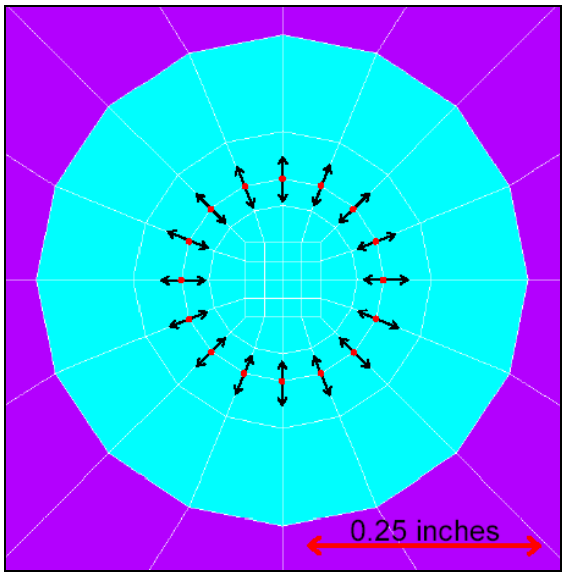

Figure 3. Piezoelectric actuator with force excitation at nodes.

Due to the high frequency of the excitation function, a mode superposition (MSP) transient analysis was used to evaluate the FEM model simulations. MSP analysis sums factored mode shapes, obtained from a modal analysis, to calculate the dynamic response.[6] MSP assumes that the structure behaves linearly. The first 15 modes of vibration are included in the MSP and cover the natural modes of vibration of the plate up to approximately 2,200Hz, which is considered sufficient for an analysis with an excitation function in the 0-1,500Hz range.

2.2 Stochastic Finite Element Analysis

Stochastic finite element analysis incorporates the uncertainty in model input parameters into the above described computational models to estimate the variability in the structural response. The structural input parameters may also vary spatially or temporally; model parameters such as distributed loads, material properties and geometric inputs cannot be expressed as a single random variable but must be represented as a collection of several correlated random variables or more specifically, as random processes and random fields.[22] Random process (temporal) and random field (spatial) simulation is a key step in this analysis and several methods are available. For example, the Karhunen-Loeve (K-L) expansion has been used to simulate random processes.[23] This method represents a given covariance function as a K-L series expansion to efficiently simulate the stochastic process over a given time or space domain. The Karhunen-Loeve expansion method is quite general and not limited to any specific type of process (stationary, non-stationary; Gaussian, non-Gaussian). It is also applicable to the generation of random fields. The K-L expansion method receives its efficiency from the condensation of a significant amount of computational effort into an analytical pre-preprocessing step, which drastically reduces the subsequent computational effort while preserving accuracy.[23] This is accomplished by determining the eigenvalues and eigenfunctions of the covariance function and utilizing them directly within the K-L series summation; however, this poses the difficulty of solving an integral equation, which usually requires numerical methods.[24] The wavelet transform method is an extension of the Karhunen-Loeve simulation algorithm and is most applicable to non-stationary Gaussian random processes and fields.[25]

An alternate Fourier series-based approach is the "spectral representation method."[26,27] Shinozuka[28,29] proposed the application of spectral representation for the simulation of multi-

dimensional, multi-variate, and nonstationary random processes and fields. Yang[30,31] introduced the Fast Fourier Transform (FFT) technique and demonstrated that it could be utilized to significantly reduce the computational expense of the Fourier series-based algorithm. Yang also proposed a formulation to simulate random envelope processes. Shinozuka[32] then extended the application of the FFT technique to multi-dimensional cases and Deodatis and Shinozuka[33] applied the resulting method to simulate stochastic waves. Yamazaki and Shinozuka proposed an iterative procedure to simulate non-Gaussian stochastic fields[34] and a method involving statistical preconditioning to reduce the sample size.[35] Additionally, Shinozuka and Deodatis wrote two review papers on the subject of simulation using the spectral representation method.[36,37] Other random process and random field generation sequences include the Pierson-Moskowitz Wave Spectra or the JONSWAP spectra[38] as well as Sakamoto's Polynomial Chaos Decomposition[39] and Deodatis and Micaletti's formulation[40] for highly skewed non-Gaussian stochastic processes.

The one-dimensional Gaussian stochastic process in Figure 4 was generated using Shinozuka's formulation,[41] which can be simulated using the following series as N goes to infinity.

$$g_o(t,\phi) = \sqrt{2}\sum_{k=0}^{N-1}\left[\sqrt{2S_{gg}(\omega_k)\Delta\omega}\cos(\omega_k t + \phi_k)\right], \quad \text{where} \quad \Delta\omega = \omega_u / N, \quad \omega_k = k\Delta\omega, \quad \text{and}$$

$k = 0,1,...,N-1$. Here ω_u is the upper cutoff frequency beyond which $S_{gg}(\omega)$ can be considered to be zero for all practical purposes. $S_{gg}(\omega)$ is the two-sided power spectral density function of the random process that is to be generated and ϕ_k are the independent random phase angles uniformly distributed between 0 and 2π radians.[40]

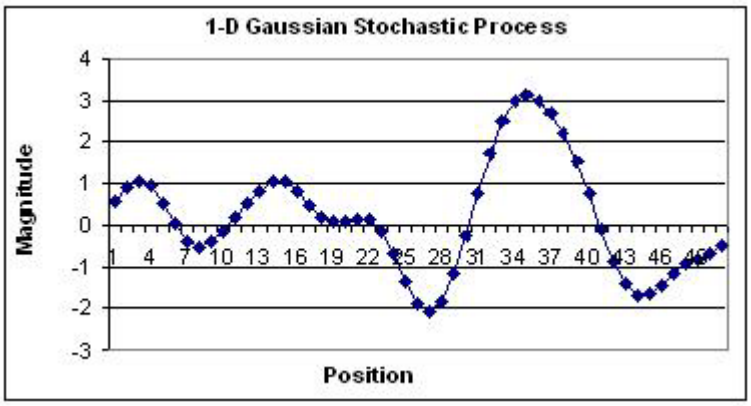

Figure 4. A realization of a random process via Shinozuka's formulation.

For the example application, plate thickness, Young's modulus, Poison's ratio, and density are modeled as Gaussian random fields with independent, but equal correlation structures along orthogonal axes. A two-dimensional stochastic process was generated for these model inputs using the spectral representation as defined in Equation (1) via Shinozuka's formulation[41] and the Wiener-Khinchine relations.[42] The Gaussian random field $g_o(x_1, x_2, \phi)$ can be simulated by the following series as N_1 and N_2 approach infinity.

$$g_o(x_1, x_2, \phi) = 2\sum_{k_1=1}^{N_1-1}\sum_{k_2=1}^{N_2-1}\left[\sqrt{S(\omega_{k_1})S(\omega_{k_2})\Delta\omega_1\Delta\omega_2}\,\cos(\omega_{k_1}x_1 + \omega_{k_2}x_2 + \phi_{k_1,k_2})\right] \qquad (1)$$

where $\Delta\omega_i = \omega_{u_i}/N_i$, $\omega_{k_i} = k_i\Delta\omega_i$, for $i = 1,2$. Here ω_{u_i} is the upper cutoff frequency beyond which $S(\omega_{k_i})$ is considered zero. $S(\omega_{k_i})$ is the two-sided power spectral density function of the random field in the i direction and ϕ_{k_1,k_2} an array containing the independent random phase angles uniformly distributed between 0 and 2π radians. N_i defines the number of terms to be included in the dual summation in the i direction. All the random fields in this study utilize the following power spectral density functions: $S(\omega_{k_i}) = \frac{1}{4}\sigma_i^2 b_i^3 \omega_{k_i}^2 \cdot \exp(-b_i\omega_{k_i})$ for $i = 1,2$. Here

σ_i is the standard deviation of the stochastic process in the i direction and b_i its corresponding "correlation distance."[40] An example of such a random field realization is provided in Figure 5. For the random fields considered as SFEM inputs to the models of the test article, $b_1 = b_2 = 3$ and $\sigma_1 = \sigma_2 = 1$, where the magnitude of $g_o(x_1, x_2, \phi)$ is scaled after the fact to match the mean and coefficient of variation (COV) of the random field to be simulated. $\omega_{u_1} = \omega_{u_2} = 5\pi$, while $N_1 = N_2 = 35$. These values were chosen such that the simulated random fields were unique (i.e. non-repeating) over an area of 16 inches by 16 inches (sufficiently large for a test article of size 12 inches x 12 inches) and the computational effort was manageable. Table 1 lists the means and COV used for each of the random fields simulated with Equation (1). Random field parameters for panel thickness were obtained by measurement of the test structure, while the random field parameters for Young's modulus, Poisson's ratio, and density were assumed.

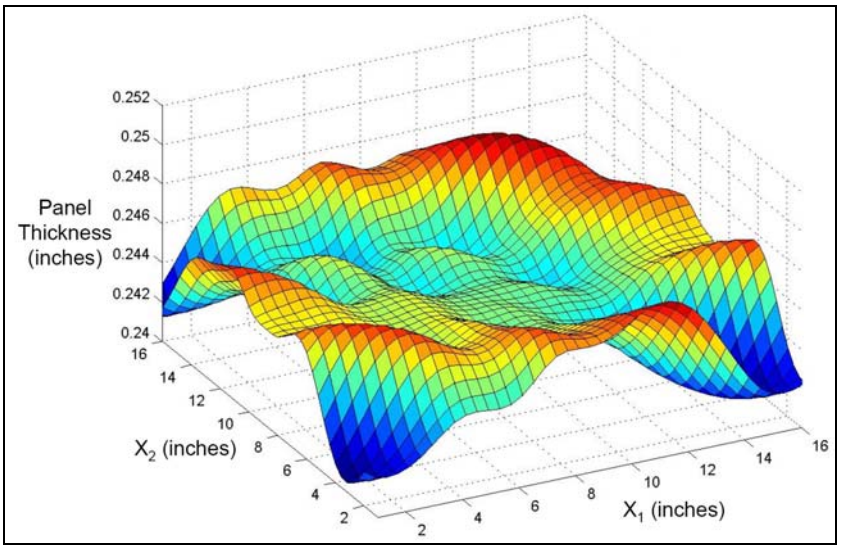

Figure 5. Sample realization of random field for plate thickness.

Table 1. Mean and COV values used for random field simulation.

	Panel Thickness (in)	Young's Modulus (psi)	Poison's Ratio	Density (lb-mass/in^3)
Mean	0.2458	9.75E+06	0.3	2.59E-04
COV	0.02	0.02	0.02	0.02

Temperature uncertainty was also included as a random variable uniformly distributed between 65 and 75 degrees Fahrenheit. These bounds reflect the approximate temperature variations of the laboratory environment at Wright Patterson Air Force Base, while the shape of the distribution was assumed. The following temperature effect model was constructed via a quadratic regression analysis of data published by the North Atlantic Treaty Organization (NATO) Advisory Group for Aerospace Research and Development (AGARD):[43]

$$F(t) = (-1.151525E-6)t^2 + (2.75775E-5)t + 1.00067 \qquad (2)$$

where $F(t)$ is a scale factor for Young's modulus and t is the plate temperature in degrees Fahrenheit.

Repeatedly evaluating deterministic finite element analyses using realizations of the model inputs provides data for statistical analysis of the model responses. For the example at hand, 500 simulations using 500 realizations of the random inputs were executed; 100 simulations of the healthy model, 100 simulations of the model damaged at bolt 1, 100 simulations of the model damaged at bold 2, and so on, where a damaged bolt refers to a bolt at 25% nominal torque and is simulated as previously specified (see Section 2.1). These 5 sets of simulations and their corresponding structural responses are used for damage detection.

The Monte Carlo approach described in the previous paragraph yields an excessive computational burden of approximately 5 hours of processing time per simulation on a Dell Workstation PWS650 with a 2.40GHz Xeon CPU and 1.00GB of RAM. The utilization of a

single personal computer, 24 hours per day, would require approximately 104 days of processing time, rendering the methodology infeasible. Therefore high performance computing (HPC) via a parallel computing cluster is employed. The Advanced Computing Center for Research and Education (ACCRE) at Vanderbilt University is an HPC facility available to researchers, scientists, engineers, and developers across many disciplines. ACCRE's mission is to permit Vanderbilt researchers to refine, benefit from, and explore a great number of newly evolved computationally intense problems and their corresponding solutions.

The above defined Monte Carlo analyses/simulations can be summarized into the following general problem, where many (100's, perhaps 1,000's) computationally intensive (hours, perhaps days) simulations, analyses, or function evaluations have to be performed using as inputs different parameter realizations. This translates into the following. For one, simulation input files, though unique, are essentially identical. Only file names and input parameters such as the seeds to random number generators, material properties, and geometric parameters are distinct from one input file to another. In addition each of the many analyses is performed using the same analysis/simulation tool (e.g. Ansys). Second, simulation management is an encumbrance due to the fact that an individual may not be able to monitor the simulation process 24 hours on end. Thus inefficiencies are introduced when a CPU only operates a limited number of hours per day. Also, manually starting or “submitting” each simulation to a CPU introduces room for human error. It is inefficient and impractical to manually supervise the analyses/simulations corresponding to 100’s of realizations of the random inputs. A "job manager" (JM) is required to automatically initiate the simulations, organize the results, and report any malfunctions to the user. Some requirements of such a job manger are as follows. All simulation input files must be of the same format and stored in one directory on the high performance parallel computing

cluster. In addition, an appropriate amount of storage space must be made available on the cluster for simulation results. Once those requirements are met, the JM can be initiated on one processor of the cluster. It will initially submit simulation input files as "jobs" to each of a user-specified/identified *n* number of processors (i.e. cluster nodes). Once each node is occupied with a unique simulation, the job manager waits for a response, which is initiated by a node once it has completed a simulation and sent the result file with a unique result file name to the designated storage space. Upon receiving this response, the JM retrieves another input file and doles it to the node which became available. This procedure continues until the JM no longer finds simulation input files in the designated input directory. Once this is true, the job manager notifies each of the processors as they complete their assigned simulation. An alternate version of the JM might run on the "gateway" computer of the parallel computing cluster and would submit portable batch system (PBS) files to the queue corresponding to unique simulation input files. This type of job manager has the additional advantage of not requiring the continuous use of *n* user specified nodes on the cluster, but rather runs the simulations on as many nodes as are currently available (which could potentially be many times *n*). In addition the applicability of this alternate version of the JM is increased through the submission of PBS files instead of simulation input files directly.

This HPC solution provides the advantage of speed-up. Using 15 nodes on ACCRE's HPC system, the computational burden is reduced from 104 days to a feasible 7 days. HPC improves the simulation process by decreasing the analysis time by the factor of nodes available to the user for parallel computing. Applications that were previously prohibitively large can now be completed in a practical amount of time with the use of a JM on an HPC network, including the example application of this study.

The simulated structural response consists of time series data. Nodal displacements along the three axial directions (rotational displacement is assumed to be negligible, as well as irrelevant, since the piezoelectric wafers utilized during laboratory experiments are likely unable to monitor the minute rotational displacement that might actually take place) are recorded for the duration of the input excitation (i.e. approximately 2.0 seconds) for each of the 2801 nodes that make up the structural components of the test article (i.e. shell elements). Figure 6 shows a normalized (i.e. $response \in [-1,1]$ and $\max(|response|) = 1.0$) randomly selected structural response of a healthy test article, while Figure 7 illustrates a simulated response obtained from a model representing the damaged test article. The plots show that in the time domain there is no significant observable difference between two realizations of the model output stemming from the same structural state and between different realizations of the output stemming from different structural states.

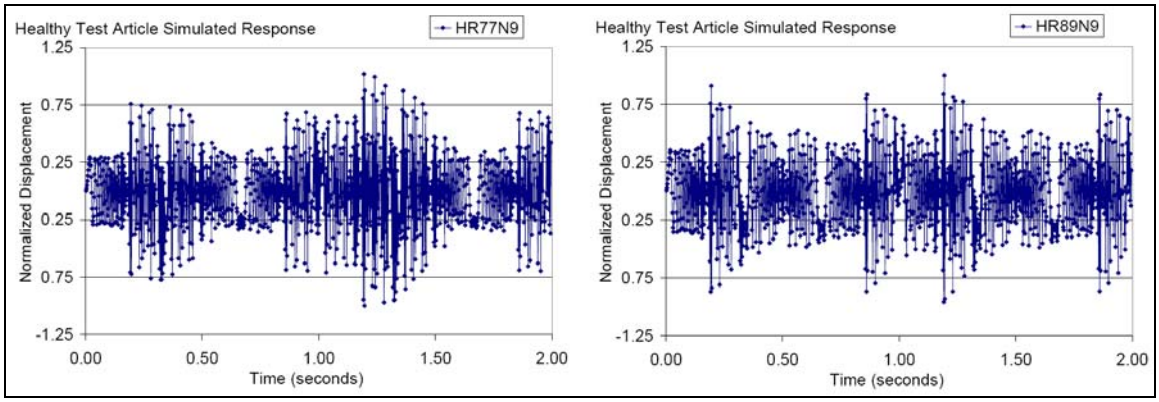

Figure 6. Healthy simulated structural response for two realizations of the random model inputs.

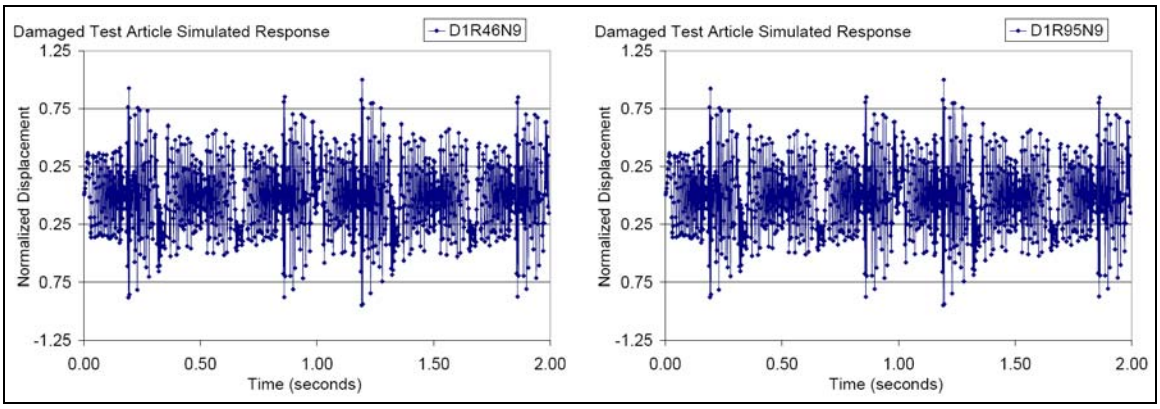

Figure 7. Damaged simulated structural response for two realizations of the random model inputs.

From the pool of simulation output of the probabilistic FEM analysis consisting of temporal displacement data along axial directions, an equivalenced von Mises stress, as defined in the Ansys Release 9.0 Documentation,[6] is calculated via Equation (3) for each node.

$$\sigma_{vM} = \sqrt{\sigma_x^2 - \sigma_x \sigma_y + \sigma_y^2 + 3\tau_{xy}^2} \tag{3}$$

where σ_x, σ_y, and τ_{xy} are the in-plane stress components, which are estimated from the displacement records of the four nearest neighboring nodes. Plane stress conditions are assumed. The equivalenced von Mises stresses of the pool of simulation output are then used directly for damage detection.

The stochastic finite element models (SFEM), as defined in this chapter are utilized to generate many realizations of the structural response, which are necessary for damage detection and sensor layout performance prediction. Prior to their utilization, it must be assured that the SFEM response predictions are of adequate accuracy. A validation assessment is required. This objective is pursued in the next chapter.

CHAPTER III

VALIDATION ASSESSMENT OF SFEM

This chapter is related to research Objective 3 and is concerned with assessing the validity of the stochastic finite element analysis discussed in Chapter 2. The second part of Objective 3 (i.e. the validation of the sensor layout performance prediction) will be addressed in Chapter 5. Several validation metrics are defined, and calibration and validation assessments of the stochastic finite element analysis are conducted. In order to calibrate and assess the accuracy of the models, experimental modal analyses (EMA) are performed and the resulting natural frequencies and mode shapes compared to analytical predictions, obtained via SFEM-based modal analysis.

3.1 Introduction

Systematic guidelines for model verification and validation, assessing the accuracy of models and computer simulations, and to build confidence and credibility in them, are under development in recent years. Sources of model uncertainty include incorrect model form (e.g. a linear model is used when the actual behavior is nonlinear), omitted variables (either for sake of simplicity or due to lack of awareness of their impact), parameter variability, information uncertainty, and inadequate model fidelity. All these sources of error need to be accounted for in assessing a model's predictive capability and usefulness. On the other hand, instrumentation and measurement errors, and variability of experimental conditions cloud experimental results.

Thus – to address uncertainties and errors in both prediction and observation – model validation under uncertainty can be viewed as comparing two sets of uncertain quantities, and assessments

about their agreement can be made using qualitative methods, decision-theoretic methods, or statistical hypothesis testing methods.[44] Several types of metrics have been proposed for the validation of analytical models in the areas of fluid dynamics,[45] heat transfer,[46] and structural dynamics[47]. The validation metrics utilized in this study are introduced and discussed in Section 3.2.

A common method of comparison between predictions for the dynamic behavior of a structure and those actually observed in the field is modal testing.[48] The qualitative formation of correlated mode pairs (CMP) followed by the quantitative assessment of modal frequencies and mode shapes via the modal assurance criterion (MAC) are well established methods of model validation[48] and are further explained in Section 3.2.1. A model reliability metric (MRM) was recently defined,[44] and is an estimation of the probability of success of a model (i.e. the probability that the difference between predicted and observed measurements is within specified limits). MRM is described in detail in Section 3.2.2. Recently Bayesian statistics have been exploited for the validation of reliability prediction models[49] and computational physics models[50]. Bayesian methods have also been extended to the validation of more generalized model outputs, both univariate and multivariate.[51] Bayesian hypothesis testing is presented in Section 3.2.3.

The difference between model calibration and validation should be noted at this point. The process associated with calibration involves "training" a model to generate output that is highly correlated and statistically equal to a set of experimentally observed measurements. Generally this consists of systematically adjusting model input parameters, such as structural damping coefficients, stiffness constants, boundary conditions, and so on, until model predictions and experimental observations are sufficiently similar as assessed heuristically or via model

validation metrics. This process is obviously highly subjective and constraints on model size, available computational power, and model output storage capacity, are usually most restrictive. Once the model is considered calibrated, model validation can be achieved by obtaining an independent set of experimental observations and utilizing the validations metrics of Section 3.2 to quantitatively (and independently) assess the predictive capabilities of the model. Section 3.4 discusses the calibration of the stochastic finite element models (SFEM) of the TPS test article, while independent experimental observations are presented in Section 3.5 and model validation metrics are applied to assess the SFEM accuracy.

3.2 Model Validation Metrics

3.2.1 Modal Assurance Criterion

Traditional model validation assessments in structural dynamics include a correlation analysis between model prediction and experimental observation. A metric known as modal assurance criterion (MAC)[48] has been commonly used for dynamic FEM model validation. MAC provides a measure of the statistical correlation between model predictions and experimental observations. The strength of correlation is measured by the least-squares deviation or scatter of the data points from a straight line. In this context, data points refer to the elements of the column vectors defining the experimentally measured mode shape $\{\Psi_X\}$ and the theoretically predicted mode shape $\{\Psi_A\}$. MAC is defined as

$$\frac{\left|\{\Psi_X\}^T \cdot \{\Psi_A\}\right|^2}{\left(\{\Psi_X\}^T \cdot \{\Psi_X\}\right)\left(\{\Psi_A\}^T \cdot \{\Psi_A\}\right)} \tag{4}$$

and is a scalar quantity close to 1.0 if the experimental and theoretical mode shapes are in fact from the same mode. If the two mode shapes, which are being compared, actually relate to two different modes of vibration, a value close to 0.0 should be obtained.[48] It should be noted that MAC is related to the correlation coefficient between two random variables given by $\rho_{X,Y} = \frac{Cov(X,Y)}{\sigma_X \bullet \sigma_Y}$, where $Cov(X,Y)$ is the covariance of the two random variables X and Y, and σ_X and σ_Y their variances, respectively; however, MAC does not adjust for the means of the random variables.

3.2.2 Model Reliability Metric

Although a correlation assessment via MAC provides a means to evaluate a predictive model, it does not give any estimate on the confidence with which the model predictions can be accepted or rejected. The probabilistic nature of and the uncertainty associated with model predictions and laboratory observations was not considered in the above comparison. In addition, for a decision maker a quantitative measure of the validity or reliability of a model is of significant value. Rebba and Mahadevan[44] defined a reliability measure for the case of comparing a single-valued model prediction with multiple experimental measurements taken for the same input. This model reliability is measured through a simple metric $r = P(-\varepsilon < D < \varepsilon)$, i.e. the probability that the observed difference, D, between model prediction and experimental observation is within a small interval $[-\varepsilon, \varepsilon]$. Here ε can be viewed as an allowable difference between prediction and observation. The model reliability metric (MRM) is calculated as

$$r = \Phi\left[\frac{\sqrt{n}\left(\varepsilon - |\bar{x} - \Theta|\right)}{s}\right] - \Phi\left[\frac{\sqrt{n}\left(-\varepsilon - |\bar{x} - \Theta|\right)}{s}\right], \qquad (5)$$

where Θ is the single-valued model prediction, while $\bar{x}$ is the sample mean and s the sample standard deviation of the experimentally observed measurements, which are assumed to follow a Gaussian distribution. n is the number of data points utilized to calculate $\bar{x}$ and s. The cumulative distribution function (CDF) of the standard normal distribution is denoted as $\Phi[\cdot]$.

3.2.3 Classical and Bayesian Hypothesis Testing

Rigorous statistical model validation approaches can also be based on hypothesis testing methods.[52] Classical hypothesis testing is based on the multivariate Hotelling's T^2 statistic, a multivariate generalization of Student's t^2 statistic, which is applicable for one-sample as well as two-sample testing. It tests whether a p-dimensional mean vector, μ, is element-wise equal to a prescribed vector, μ_0. In case of high correlation among the p variables to be tested, a principal component analysis may be used to transpose the correlated variables into an uncorrelated, lower-dimensional variable space. Multivariate hypothesis testing via Hotelling's T^2 statistic is then available on the principal components.[53]

One particular downside to traditional point null hypothesis tests is that they test whether the mean is exactly equal to a prescribed value. As the sample size increases, the hypothesis will always be rejected, even if the mean deviates only slightly from μ_0. This can prove to be problematic, since it may be acceptable to observe a small difference between model prediction and experimental observation. Thus an interval hypothesis test formulation is also available. Finally, classical metrics include the calculation of power of the hypothesis test, which indicates the benefit of gathering additional data. The power is the probability of rejecting the null hypothesis given that the alternative hypothesis is true. It is an indication of the effectiveness of the test in discerning between the two competing hypotheses. It should be noted that the power

of a hypothesis test is equal to $(1 - P(TypeII))$, where $P(TypeII)$ is the probability of a Type II error, which occurs when one fails to reject a false null hypothesis. Conversely, a Type I error occurs when one rejects a true null hypothesis.

Additionally Bayesian hypothesis testing[54] enables the estimation of relative support for two competing hypotheses given that the experimental observations, O_E, were made. Formally, the posterior probability ratio of the two competing hypotheses is calculated.[51] The validation metric, Bayes' factor, is defined through a likelihood ratio as

$$B = \frac{P(O_E|H_0)}{P(O_E|H_1)} \tag{6}$$

and is used to assess which hypothesis the data supports more. If $B = 1$, H_0 and H_1 are equally supported by the data. If $B > 1$, the data supports H_0 more, and if $B < 1$, there is more support for H_1. In addition, a confidence estimate, C, for H_0 is given by the ratio $B/(B+1)$, e.g. if $B = 1$, the data gives equal support for both hypotheses and the confidence level for H_0 is 50%. The Bayes' factor is applicable for one-sample as well as two-sample testing and the corresponding power of the hypothesis test can also be calculated. For multivariate data, as is normally the case for model validation, it is usually assumed that the data follow a multivariate normal distribution, in order to easily apply the Bayesian perspective to hypothesis testing.[51] If this assumption does not hold, the use of a response surface approximation, such as polynomial chaos, may be employed to estimate the shape of the probability density functions.[55]

3.3 Modal Analysis

The model calibration and validation presented in this chapter is approached through modal analysis. Two stochastic finite element models (SFEM) – one model to simulate the healthy

structure and one model to simulate one of the four damaged test articles – for structural dynamics analysis are evaluated, calibrated, and validated using data obtained from experimental observations. SFEM incorporating the variability in input parameters are utilized to predict the statistics of the natural modes of vibration (i.e. frequencies and mode shapes) of the two test article conditions. Experimental modal analyses (EMA) are performed on laboratory specimens of the TPS test article in the same two conditions to predict their natural modes of vibration and corresponding mode shapes. Modal analysis results from predictions and observations are then compared.

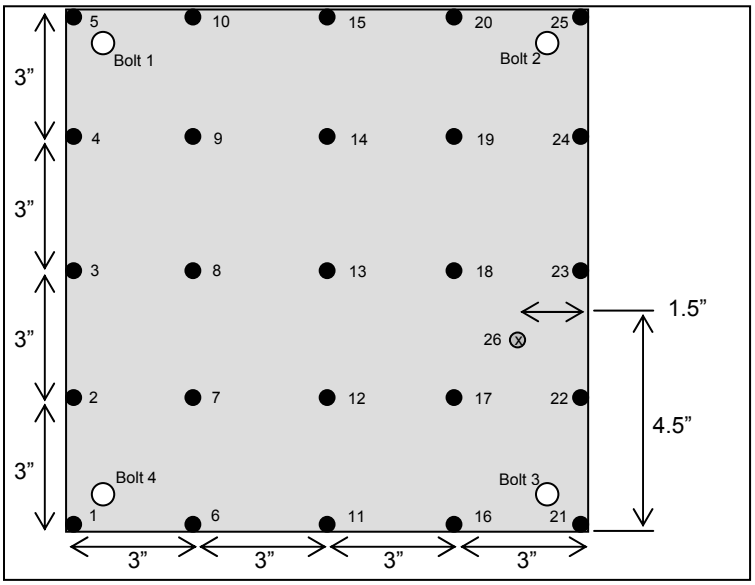

Figure 8. EMA test layout.

Experimental modal analysis (EMA) was performed on the prototype TPS component described in Section 1.4, where the first eight modes of vibration (modal frequencies and mode shapes) were extracted (resolution limitations of EMA restricted the consideration to the first eight modes of vibration). Figure 8 is a schematic showing the EMA measurement points as well as the impact locations. EMA was performed on both healthy and damaged structures where the

plate was impacted with the instrumented hammer at location 26. An additional EMA of the healthy plate was performed where the plate was impacted at location 7.

EMA consists of impacting a test article with an instrumented hammer at carefully selected locations (locations 7 and 26 in Figure 8) and measuring the structural response of the test article via an array of accelerometers (locations 1 through 25 in Figure 8). EMA utilizes the input signal (as measured with the instrumented hammer) and the response signal (as collected by the array of accelerometers) to establish frequency response functions (FRF) between each response location and the impact site. FRF are defined as the ratio of the Fourier transforms of the response and the input. The modal parameters are then identified by curve fitting the set of FRF as shown in Figure 9 for a simply supported vibrating beam.[56]

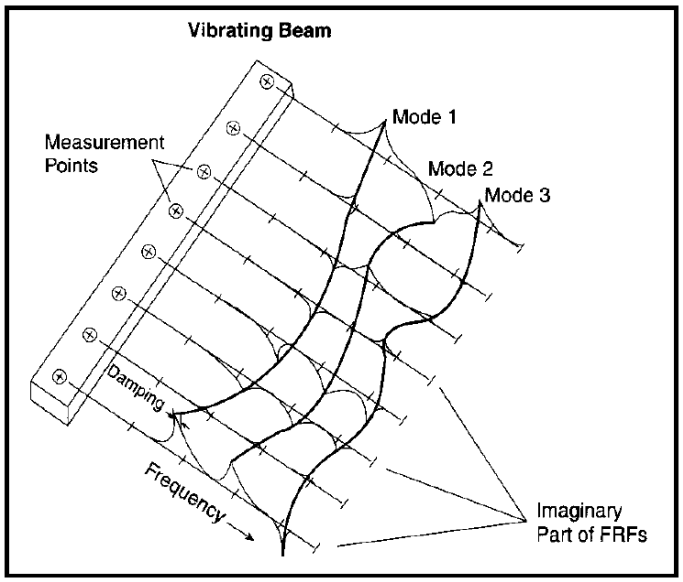

Figure 9. Curve fitting FRF measurements.[56]

Uncertainties associated with EMA include variability of accelerometer placement as well as variability of impact location of the instrumented hammer. In addition, the operator's subjectivity in accepting or rejecting a given impact and its corresponding response produces

uncertainty in EMA results. Also, since the data acquisition system utilized for EMA is limited to four channels of input, multiple experiments were required to obtain the response of the plate for all 25 locations shown in Figure 8. Other experimental variability also influences the results obtained via EMA. The assumptions and approximations associated with the signal processing (such as transforming a finite discrete signal using a transformation that is theoretically derived for infinite continuous functions) required to establish FRF, add additional uncertainties to EMA results.

The state classification problem defined in Section 1.4 considers four damage states (fastener damage at each of the four bolt locations simulated by a bolt with 25% nominal torque) and the healthy condition (all four fasteners at 100% nominal torque). This requires the simulation of five different state models; however, due to symmetry of the test article (e.g. damage state 2, i.e. 25% nominal torque at bolt location 2, is simply a 90° clockwise rotation of test article damage state 1, i.e. 25% nominal torque at bolt location 1, etc.) only two conditions were analyzed for validation purposes: 1) healthy structure, and 2) damaged structure with damage at bolt location 4. Two EMA were performed on the healthy test article; one EMA was performed on the damaged test article. The results are presented in Table 2, Table 3, and Figure 10. Due to resolution limitations of EMA, the mode shape vectors of a damaged test article could not be differentiated from the mode shape vectors of Table 3. Therefore mean results are provided only for the healthy condition.

Table 2. EMA modal frequency results (Hz).

Mode of Vibration	1	2	3	4	5	6	7	8
1st EMA - Healthy	218.23	404.19	404.19	462.41	833.95	929.32	1010.00	1010.00
2nd EMA - Healthy	217.71	400.35	400.35	461.34	831.30	928.02	1010.00	1010.00
1st EMA - Damaged	213.48	394.68	394.68	454.43	826.63	919.27	953.42	953.42

Table 3. EMA-based mean mode shape vectors for healthy model.

	Mode Number							
	1	2	3	4	5	6	7	8
Mode Shape Vectors	0.027	-0.023	-0.023	-0.008	0.041	-0.062	0.075	0.075
	-0.270	0.518	0.518	-0.535	-0.537	0.720	0.630	-0.630
	-0.535	0.970	0.970	-0.953	-1.000	-0.103	0.005	-0.005
	-0.267	0.513	0.513	-0.530	-0.574	-0.836	1.000	1.000
	0.023	-0.018	-0.018	-0.002	0.018	0.034	-0.033	-0.033
	-0.279	-0.139	-0.139	0.503	-0.532	0.852	-0.114	0.114
	-0.627	0.358	0.358	0.017	-0.045	0.937	0.552	-0.552
	-0.874	0.563	0.563	-0.316	0.292	-0.003	0.006	-0.006
	-0.612	0.428	0.428	0.030	-0.041	-0.825	-0.234	0.234
	-0.248	0.112	0.112	0.541	-0.460	-0.646	-0.846	-0.846
	-0.581	-0.231	-0.231	0.933	-0.995	0.048	-0.778	0.778
	-0.855	-0.132	-0.132	0.297	0.202	0.013	0.180	-0.180
	-1.000	0.003	0.003	-0.003	0.920	-0.008	0.013	-0.013
	-0.856	0.137	0.137	0.346	0.249	-0.024	0.191	0.191
	-0.491	0.223	0.223	1.000	-0.963	-0.059	-0.751	-0.751
	-0.279	-0.132	-0.132	0.513	-0.585	-0.937	0.811	0.811
	-0.656	-0.433	-0.433	-0.010	-0.051	-1.000	-0.248	-0.248
	-0.831	-0.518	-0.518	-0.319	0.231	-0.031	0.005	0.005
	-0.613	-0.346	-0.346	0.003	-0.049	0.878	0.531	0.531
	-0.277	0.125	0.125	0.582	-0.612	0.741	0.170	-0.170
	0.014	0.015	0.015	-0.003	0.038	0.022	0.017	0.017
	-0.249	-0.499	-0.499	-0.496	-0.421	-0.741	-0.872	-0.872
	-0.550	-1.000	-1.000	-0.960	-0.963	0.124	-0.035	-0.035
	-0.251	-0.493	-0.493	-0.496	-0.503	0.878	0.617	0.617
	0.029	0.018	0.018	0.000	0.026	-0.014	0.075	-0.075

Mode shapes 1, 4, 5, and 6 are very well defined and have unique modal frequencies. However, two sets of paired natural modes of vibration, modes 2 and 3, and modes 7 and 8, were not well defined due to resolution limitations. EMA was unable to isolate distinctive natural frequencies or mode shapes for each of the contributing modes of the two mode pairs. Figure 10 shows a single mode shape for each of these sets of paired modes where the mode shape includes contributions from each of the paired modes. As becomes evident from the FEM-based modal analyses (see below), the paired mode shapes shown in Figure 10 are a result of superimposing mode shape 3 onto mode shape 2 and mode shape 8 onto mode shape 7. It should also be noted that the mode shapes contributing to each coupled pair are approximately identical to each other, but rotated 90° in plane about the center of the plate with respect to each other. In addition, the

mode shapes obtained via EMA of the damaged structure were very similar to those of the healthy panel: small variations in the paired modes due to the loose bolt exist; however, EMA did not have sufficient resolution to discern these variations.

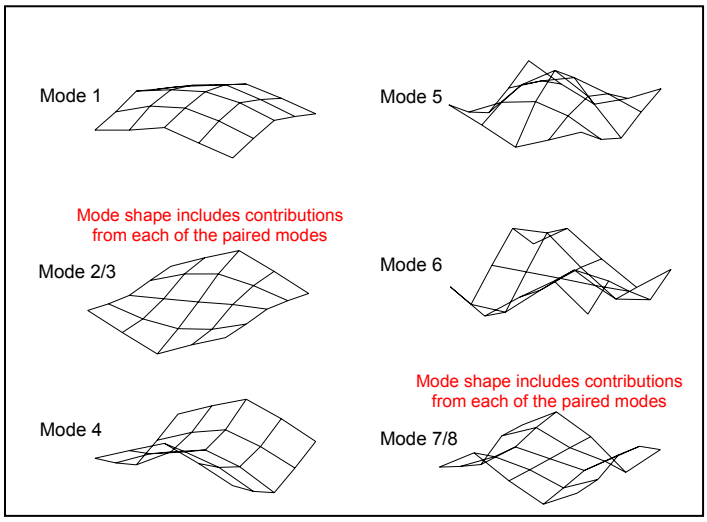

Figure 10. EMA mode shape results.

The FEM-based modal analysis consists of generating 100 random realizations of the model input quantities as discussed and demonstrated in Section 2.2, using 50 of them as inputs to the healthy model and the other 50 as inputs to the damaged model, performing a modal analysis for each realization, and extracting and expanding the first eight modes of vibration. The Block Lanczos eigenvalue solver within the Ansys[6] software package is used to determine the natural frequencies and corresponding mode shape vectors. The block Lanczos algorithm is a variation of the classical Lanczos algorithm, where the Lanczos iterations are performed using a block of vectors, as opposed to a single vector. Additional theoretical details on the classical Lanczos method can be found in Rajakumar and Rogers.[57] The Block Lanczos method, as employed by Ansys, uses a sparse matrix solver and is especially powerful when searching for eigenfrequencies in a given part of the eigenvalue spectrum of a system (i.e. 0-1500Hz in this

case). Other benefits to using this extraction method are medium memory and low disk-space requirements.[6] This FEM-based modal analysis approach yields two sets (healthy and damaged) of 50 mode shapes with corresponding modal frequencies corresponding to the two condition models. Table 4 and Table 5 summarize the FEM-based modal analyses results of the calibrated models of a healthy and a damaged test article. Calibration was achieved as described in Section 3.4.

Table 4. FEM-based modal analysis results.

Healthy Model			Damaged Model		
Mode	Mean Modal Frequency (Hz)	Standard Deviation	Mode	Mean Modal Frequency (Hz)	Standard Deviation
1	222.68	1.10	1	208.23	0.74
2	406.00	1.69	2	382.81	3.30
3	408.76	1.84	3	388.97	1.80
4	461.22	2.23	4	460.37	3.56
5	798.00	3.32	5	816.52	4.40
6	929.22	2.14	6	924.51	3.29
7	1001.97	3.55	7	979.52	5.71
8	1006.80	3.43	8	1046.39	4.10

Figure 11 shows the mode shapes corresponding to the modal frequencies of Table 5 for the model of the healthy test article. As stated earlier, it is easily seen that the 3rd mode shape is simply a 90° rotation of the 2nd mode shape. The same is true for mode shapes 7 and 8. Also, superimposing mode shape 2 onto mode shape 3, and mode shape 7 onto mode shape 8, produces the plots in Figure 12, which are similar to the ones shown in Figure 10 labeled as paired modes.

Table 5. FEM-based mode shape vectors for healthy model.

	Mode Number							
	1	2	3	4	5	6	7	8
Mean Mode Shape Vectors	0.007	-0.005	-0.006	0.000	0.013	-0.032	0.008	0.007
	-0.213	0.336	0.371	-0.499	-0.496	0.737	-0.294	-0.305
	-0.470	0.666	0.738	-0.943	-0.975	0.001	0.330	0.199
	-0.214	0.336	0.371	-0.499	-0.498	-0.737	0.625	0.504
	0.007	-0.005	-0.005	0.000	0.013	0.032	-0.003	-0.003
	-0.213	-0.010	0.018	0.501	-0.496	0.734	0.125	0.182
	-0.599	0.218	0.266	0.001	-0.042	0.968	-0.466	-0.367
	-0.815	0.380	0.421	-0.303	0.185	-0.001	-0.084	-0.056
	-0.599	0.237	0.232	0.005	-0.044	-0.969	0.169	0.184
	-0.213	0.015	-0.031	0.506	-0.499	-0.727	-0.569	-0.443
	-0.469	-0.029	0.041	0.946	-0.975	-0.002	0.689	0.620
	-0.815	-0.019	0.027	0.305	0.185	-0.001	-0.189	-0.163
	-1.000	-0.002	0.000	0.000	0.814	-0.003	0.001	0.001
	-0.815	0.013	-0.032	0.311	0.184	0.001	0.189	0.164
	-0.468	0.022	-0.058	0.956	-0.977	0.010	-0.695	-0.622
	-0.213	-0.018	0.021	0.501	-0.498	-0.735	0.564	0.438
	-0.599	-0.239	-0.232	-0.005	-0.045	-0.968	-0.172	-0.189
	-0.814	-0.382	-0.416	-0.314	0.183	0.000	0.086	0.057
	-0.599	-0.221	-0.266	-0.002	-0.044	0.968	0.469	0.375
	-0.212	0.006	-0.027	0.504	-0.496	0.736	-0.125	-0.179
	0.007	0.005	0.005	0.000	0.013	0.032	0.003	0.003
	-0.212	-0.333	-0.361	-0.507	-0.499	-0.726	-0.625	-0.508
	-0.467	-0.661	-0.720	-0.960	-0.981	0.005	-0.330	-0.202
	-0.211	-0.332	-0.361	-0.506	-0.498	0.730	0.294	0.307
	0.007	0.005	0.006	0.000	0.013	-0.031	-0.008	-0.007

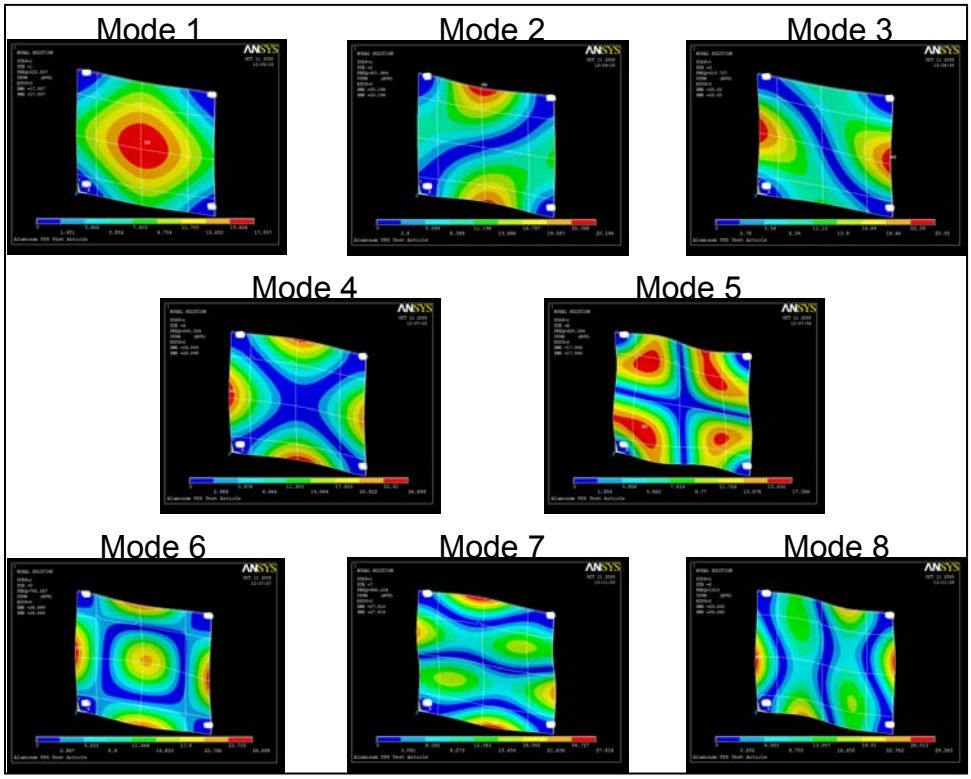

Figure 11. Analytically determined mode shapes for healthy test article.

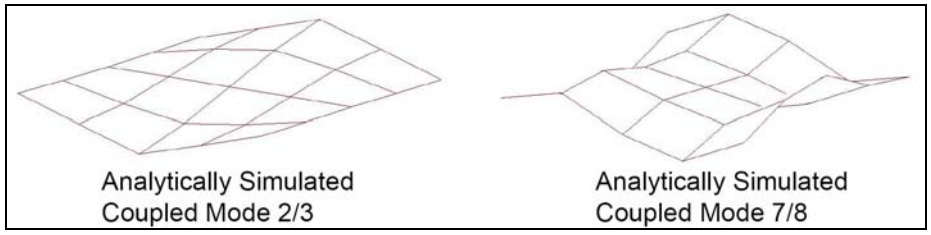

Figure 12. Analytically determined and superimposed mode shapes for coupled modes.

Figure 13 shows the mode shapes corresponding to the modal frequencies of Table 4 for the model of the damaged test article. The mode shapes of the damaged test article model are similar to the ones extracted from the healthy plate model, with the exception of modes 2, 3, 7, and 8. These coupled modes are highly affected by the loosened bolt in the lower left corner of the plate (i.e. bolt 4 in Figure 1b), creating a dominant and a recessive line of symmetry (LOS). The dominant LOS connects the lower left corner of the plate with the upper right corner, while

the recessive LOS connects the upper left corner with the lower right corner. It is worth noting that for the healthy model these LOS also exist; however, they are of equal dominance, causing the plots in Figure 11 to appear much more symmetric than the ones in Figure 13.

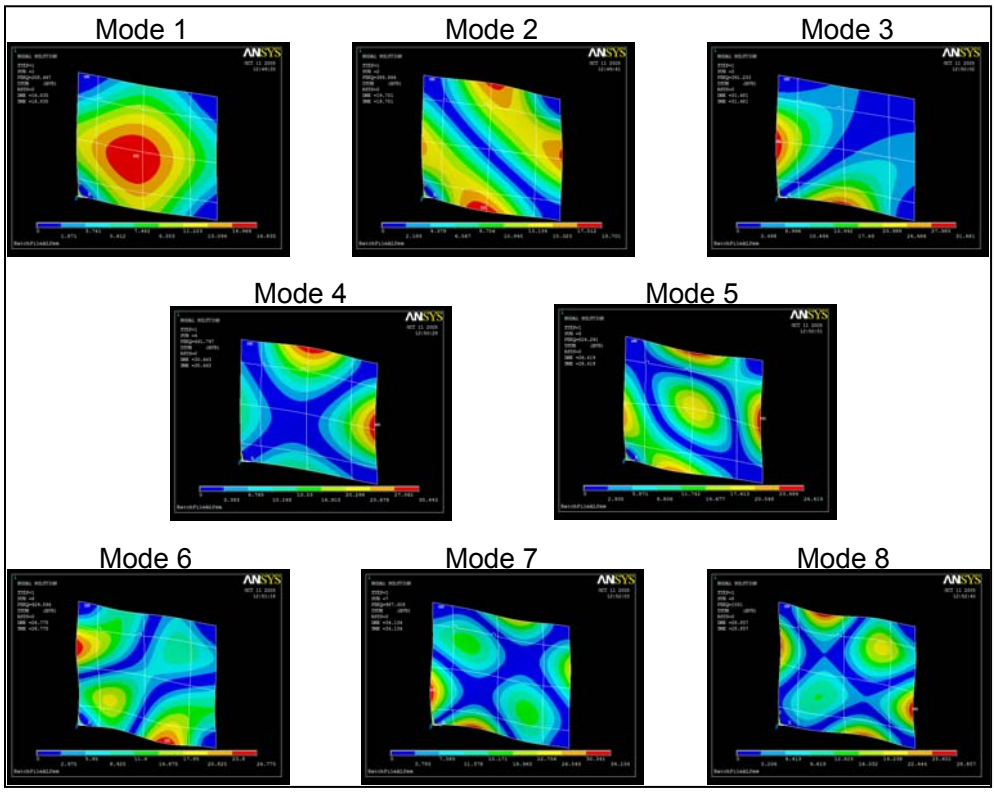

Figure 13. Analytically determined mode shapes for damaged test article.

The dominant and recessive LOS may also help explain the rise in the FEM-based natural frequency of the 8th mode of vibration of the damaged structure. Physics-based intuition indicates that damage (e.g. a loose bolt) should cause a reduction in structural stiffness and thus a decrease in natural frequency magnitudes. As shown in Table 4 this is true for almost all modes except the 8th mode of vibration (the 5th mode of vibration also portrays this property; however, much less prevalently). This coupled mode is achieved by rotating mode shape 7 by 90° about the center of the plate. When doing so, the previously dominant LOS now coincides with the

recessive LOS. To overcome this unsymmetrical condition created by the loosened bolt in the lower left corner of the plate, a higher modal frequency is required for the 8th mode of vibration. In addition it should be noted that modes of vibration 9 and higher do not have a one-to-one correspondence between the healthy panel and damaged panels (i.e. the mode shapes for modes 9 and higher of the healthy state model do not correlate with those of the damaged state model).

In general, it is concluded that analytical predictions of the natural frequencies and mode shapes of the test article, obtained via modal analysis of the SFEM, correspond very well to EMA results. Significant discrepancies between prediction and observation are due to resolution limitations of EMA. The above qualitative assessment therefore concludes that eight correlated mode pairs (CMP) exist.

3.4 Model Calibration

Calibration was performed via systematically altering certain inputs to the FEM model. The model input parameter available for adjustment that was analyzed first was finite element mesh size. Due to constraints associated with model size, available run time, and model output capacity, a mesh size of 0.25 inches was chosen as the nominal element size (i.e. average element size; elements surrounding the bolt locations, as well as elements making up the simulated actuator, have a smaller element size – as small as 0.025 inches).

The finite element discretization error was estimated based on the Richardson extrapolation method[58]. In this method, the estimated numerical solution error due to mesh size h_1 (coarse mesh) is calculated as defined in Equation (7).

$$\varepsilon_{Richardson} = \frac{y_2 - y_1}{1 - r^p} \tag{7}$$

where the mesh refinement ratio $r = h_2/h_1$, and y_1 and y_2 are the model outputs via a coarse and finer mesh, respectively. The order of convergence, p, can be estimated as $p = \ln\left(\left(y_3 - y_2\right)/\left(y_2 - y_1\right)\right)/\ln\left(r\right)$, where y_3 is the model output with the finest mesh size possible, and $r = h_2/h_1 = h_3/h_2$. It should be noted that for a particular realization of the random model inputs, discretization error is by itself deterministic. Also the estimated error will not be accurate if even the finest mesh used in an analysis is not fine enough and asymptotic convergence of the finite element solution when mesh size is reduced, is not observed (i.e. y_1, y_2, and y_3 should either progressively decrease or increase).[59]

Table 6. Model discretization error quantification.

Mode of Vibration	Nominal Element Size (inches)			Richardson Error
	0.25	0.125	0.0625*	
1	225.93	225.62	225.59	-0.34
2	413.45	412.88	412.82	-0.64
3	413.45	412.88	412.82	-0.64
4	467.93	467.12	467.06	-0.87
5	810.56	810.2	810.17	-0.39
6	943.42	942.54	942.43	-1.01
7	1019.9	1018.9	1018.8	-1.11
8	1019.9	1018.9	1018.8	-1.11
9	1361.9	1359.5	1359.3	-2.62
10	1488.9	1488.2	1488.2	-0.70
11	1488.9	1488.2	1488.2	-0.70
12	1843.1	1842.3	1842.2	-0.91
13	2033.9	2033.0	2032.9	-1.01
14	2202.5	2199.8	2199.6	-2.92
15	2202.7	2199.8	2199.6	-3.11
*** Maximum number of nodes (128,000) supported by Ansys 9.0 (University Advanced - Research License)**				

Table 6 shows the results of three modal analyses of the FEM model of the healthy test article corresponding to three different mesh sizes. Note that these FEM analyses did not include the uncertainty of the model input parameters and were of an un-calibrated model. Hence, the

results of Table 6 do not echo the results shown in Table 4. A refinement ratio of 0.5 was applied twice to the model containing elements of nominal size 0.25 inches to obtain models with nominal mesh size 0.125 inches and 0.0625 inches. In this context, "nominal size" refers to the average size of the majority of elements of the model (i.e. the model contains smaller elements, as well as elements where at least one side is greater than the nominal size – especially near the simulated bolt and actuator locations). It should be noted that for the model with nominal mesh size 0.0625, the maximum number of nodes (128,000) for Ansys 9.0 (University Advanced – Research License) was surpassed and not all elements of the model received perfect mesh refinement of 0.5. Therefore, the nominal mesh size of the finest model is only approximately 0.0625 inches.

From Table 6 it was concluded that the discretization error of the FEM model was insignificant. The largest percent error occurred in predicting the 9^{th} mode of vibration and was estimated as 0.19%. Therefore, a nominal mesh size of 0.25 inches is adequate given the restrictions on available analysis run time and model output storage capacity.

Calibration was continued via systematically altering the boundary conditions of the SFEM. A major contribution to calibration was obtained by investigating the effect of the stiffness constants of the spring elements that were used to simulate the bolted condition in each corner of the plate, as well as changing the number and configuration of those spring elements. The final calibrated boundary conditions at each bolt location consisted of 48 spring elements arranged in two circles (24 spring elements per circle) of radii 0.1366 inches and 0.2 inches around the bolt hole center such that the spring force acts perpendicular to the TPS plate. The area impacted by the spring elements approximately covers the area contacted by the bolt head and washer. The calibrated spring constants are 100,000 pounds/inch for healthy bolt conditions and 52,000

pounds/inch for a damaged bolt condition. All nodes contained within a 0.125 inch radius of each bolt hole center, are fixed in translation, while the nodes contained within 0.1134 inches of each bold hole center are additionally fixed in rotation.

Systematic permutations were applied to the previously mentioned boundary conditions and modal analyses for both healthy and damaged test articles were performed via SFEM. For each set of evaluations the model validation metrics of Section 3.2 were considered. The results corresponding to the calibrated models are presented in the following sections.

3.4.1 Modal Comparison

This section presents the assessment of the calibrated FEM models via modal testing, which provides a quantitative comparison between the predicted dynamic behavior of the test article (in both healthy and damaged states) as estimated by the calibrated models and those actually observed in the laboratory. The first step of this comparison consists of ordering the modes of vibration (mode shapes and corresponding natural frequencies) for both the predictor models as well as the observed experiments. See Figure 10, Figure 11, and Figure 13 and Table 2 through Table 5 . From a visual comparison, as summarized in Section 3.3, it can be concluded that the modes as predicted by the FEM model, actually correspond to the observed modes of vibration and that 8 correlated mode pairs (CMP) exist.

The next step is to quantitatively check how well the two sets of CMP are in fact correlated with one another. This is first investigated by plotting the experimentally observed modal frequency value against the predicted one for each of the 8 modes included in the comparison. The plots, along with trend lines and R^2-values are shown in Figure 14.

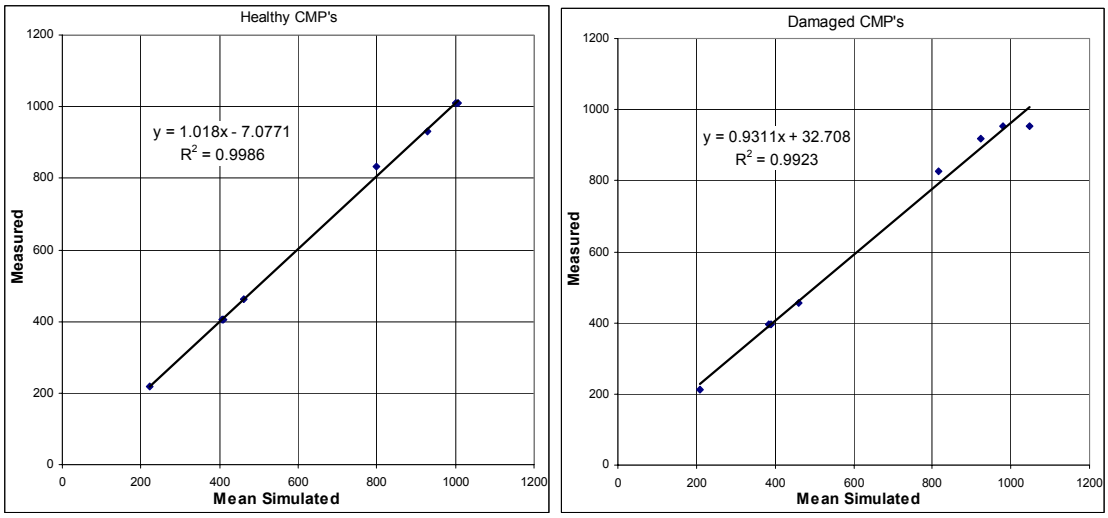

Figure 14. Plots of correlated mode pairs (axes show frequency - Hz).

Both plots in Figure 14 show that each set of points lies on a straight line with slope approximately equal to 1.0. In addition the scatter as measured by the R^2-values is minimal, leading to the conclusion that the model predictions for the natural frequencies of the test specimen are highly correlated with the experimental observations. Natural frequency difference (NFD) diagrams have also been generated and are shown in Figure 15. NFD diagrams plot the natural frequency difference between all possible combinations of experimental and analytical model modes, showing any discrepancies in the CMP set. As can be seen from the plots in Figure 15, the difference between the predicted and observed is least for the given sets of CMP.[48]

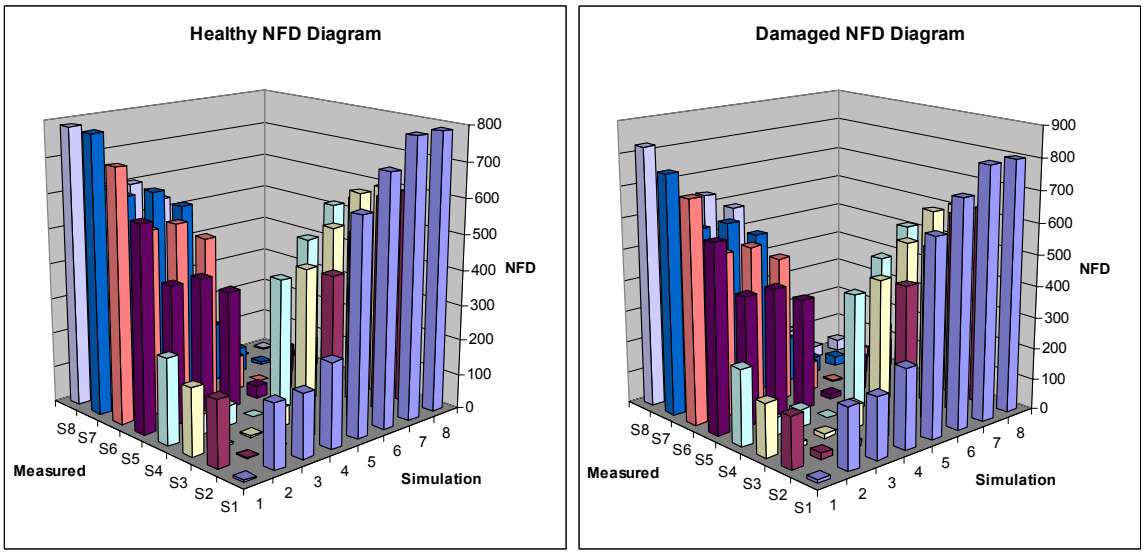

Figure 15. Natural frequency difference diagrams.

In addition to the above comparisons of natural frequencies, the mode shapes also need to be compared quantitatively. Given a set of 8 experimental mode shapes and a set of 8 predicted mode shapes, the 8x8 MAC-matrix shown in Table 7 can be constructed.

Table 7. MAC matrix for the healthy model.

		Experimental Mode Shape Number							
		1	2	3	4	5	6	7	8
Predicted Mode Shape Number	1	**0.994**	0.001	0.001	0.000	0.066	0.001	0.000	0.000
	2	0.000	**0.359**	0.641	0.003	0.000	0.001	0.000	0.177
	3	0.000	0.359	**0.641**	0.003	0.000	0.001	0.000	0.177
	4	0.000	0.006	0.000	**0.993**	0.001	0.000	0.000	0.001
	5	0.027	0.000	0.001	0.000	**0.986**	0.010	0.001	0.003
	6	0.000	0.001	0.002	0.000	0.002	**0.960**	0.000	0.018
	7	0.002	0.004	0.058	0.115	0.020	0.111	**0.177**	0.077
	8	0.000	0.097	0.033	0.000	0.000	0.001	0.925	**0.000**

Generally speaking, a value in excess of 0.9 implies well correlated modes[48]. Table 7 shows that modes of vibration 1, 4, 5, and 6 are very well correlated with MAC values greater than 0.95. The two sets of paired modes, modes 2 and 3, and modes 7 and 8, however, stand out as insufficiently correlated at best. This is due to the fact that EMA does not clearly differentiate

the mode shapes of these paired modes. Instead, EMA lumps coupled modes into a single combined mode shape, causing the experimental results to include contributions from both of the paired modes. It is unwise to place much significance on the MAC values of these coupled modes. Therefore, it can generally be inferred from the modal comparison that analytical predictions and experimental observations correspond very well with one another.

3.4.2 Model Reliability Metric

The model reliability metric (MRM) can be applied directly to data corresponding to the damaged test article. In this case Θ represents a single experimental observation, while $\bar{x}$ and s are the observed sample mean and sample standard deviation of the modal frequency predictions, respectively. n is the number of data points utilized to estimate $\bar{x}$ and s.

Table 8. MRM for modal frequencies of damaged test article.

Mode #	Epsilon					
	0.04*MF	0.03*MF	0.025*MF	0.02*MF	0.015*MF	0.01*MF
	r	r	r	r	r	r
1	1.000	1.000	0.353	0.000	0.000	0.000
2	1.000	0.206	0.000	0.000	0.000	0.000
3	1.000	1.000	1.000	1.000	0.689	0.000
4	1.000	1.000	1.000	1.000	0.972	0.004
5	1.000	1.000	1.000	1.000	1.000	0.001
6	1.000	1.000	1.000	1.000	1.000	1.000
7	1.000	1.000	1.000	0.000	0.000	0.000
8	0.000	0.000	0.000	0.000	0.000	0.000

Table 8 shows the results for the damaged test article, where ε takes on values of 4%, 3%, 2.5%, 2%, 1.5%, and 1% of each corresponding modal frequencies (MF). Note that since it is unknown which of the two sets of measurements (observation and prediction) is indeed true, the MF for a given mode of vibration is the average of all predicted and observed measurements combined (i.e. the comparison is not biased towards model prediction nor towards experimental

observation). However, it is also worth noting that utilizing a percent of MF for ε does cause the results to be biased towards passing modes of vibration with high modal frequencies; however, due to the increased uncertainty associated with modes of vibration greater than approximately 900Hz (due to EMA's decreased resolution at higher modes of vibration), utilizing a percent difference between observation and prediction is warranted. The tendency of more easily passing modes of vibration with high modal frequencies, which is associated with using a percent difference, might also help explain the poor performance of the model with respect to MRM when evaluating the first mode of vibration (i.e. excluding the coupled modes of vibration, MRM passes each mode of vibration with increasing ease as the modal frequency increases).

Table 8 shows that for the first seven modes of vibration the experimentally observed frequencies are within 4% of the corresponding predicted values with 100% probability (i.e. $r = 1.000$). It also shows that as the allowable difference, ε, decreases from 4% to 1% of MF, the reliability measure, r, also decreases as is expected. The results in Table 8 also show that the eighth mode of vibration as observed during experiments has zero probability of being within 4% of its corresponding predicted modal frequency. In fact, an allowable difference of 10% of MF is required to yield a MRM of 100% for the eighth mode of vibration. These results are similar to the comparisons made with MAC in that they clearly identify the coupled EMA modes of vibration as insufficiently similar to FEM predictions. In addition, the results show that MRM is a stricter and more discriminating measure for validation and better identifies differences between model predictions and laboratory observations than the previous correlation assessment.

In order to apply MRM to data corresponding to the healthy test article, additional considerations must be made since multiple (two) experimental observations in addition to the (50) SFEM

prediction measurements are available. First it is assumed that both the predicted modal frequencies and the experimentally observed modal frequencies are normally distributed. A simple normality test verifies this assumption for the predicted data sets; however, due to there being only two samples in the experimentally observed data sets, normality is difficult to verify for the experimental observations; however, due to the nature of experimental error (a major source of uncertainty in experimentally observed data) the assumption is reasonable. The mean of the difference between predicted and observed modal frequencies is then defined as $\overline{D} = \bar{x}_1 - \bar{x}_2$, where $\bar{x}_1$ is the observed sample mean and $\bar{x}_2$ is the predicted sample mean. If $\bar{x}_1 \sim N\left(\mu_1, \frac{\sigma_1}{\sqrt{n_1}}\right)$ and $\bar{x}_2 \sim N\left(\mu_2, \frac{\sigma_2}{\sqrt{n_2}}\right)$, where μ_1 and μ_2 are the true means and σ_1 and σ_2 are the true standard deviation of the observed and predicted data, respectively, then $\overline{D} \sim N\left(\mu_1 - \mu_2, s_{\overline{D}}\right)$, where $s_{\overline{D}}$ is the pooled standard deviation of $\overline{D}$, defined as $s_{\overline{D}} = \sqrt{\left(\frac{\sigma_1^2}{n_1} + \frac{\sigma_2^2}{n_2}\right)}$. n_1 and n_2 are the number of data points in the observed and predicted data sets, respectively. MRM can then be estimated for the model of the healthy test article as follows:

$$r = \Phi\left[\frac{\varepsilon - \overline{D}}{s_{\overline{D}}}\right] - \Phi\left[\frac{-\varepsilon - \overline{D}}{s_{\overline{D}}}\right], \tag{8}$$

where s_1 and s_2 are estimators of σ_1 and σ_2 in $s_{\overline{D}}$, respectively.

Table 9 shows the MRM results for the healthy test article, where ε takes on values of 5%, 4%, 3%, 2%, 1%, and 0.5% of the corresponding modal frequencies, MF. Table 9 indicates that the mean frequencies of all modes of vibration as observed through experimental measurements are

within 5% of the corresponding predicted modal frequencies with 100% probability. The results in Table 9 are in agreement with previous comparisons.

Table 9. MRM for modal frequencies of healthy test article.

Mode #	Epsilon					
	0.05*MF	0.04*MF	0.03*MF	0.02*MF	0.01*MF	0.005*MF
	r	r	r	r	r	r
1	1.000	1.000	1.000	0.197	0.000	0.000
2	1.000	1.000	1.000	0.988	0.568	0.189
3	1.000	1.000	0.999	0.808	0.108	0.011
4	1.000	1.000	1.000	1.000	1.000	0.996
5	1.000	0.030	0.000	0.000	0.000	0.000
6	1.000	1.000	1.000	1.000	1.000	1.000
7	1.000	1.000	1.000	1.000	1.000	0.000
8	1.000	1.000	1.000	1.000	1.000	1.000

Applying MRM to mode shapes corresponding to the modal frequencies tested above requires a multivariate formulation of r and the joint probability density functions describing the elements of each mode shape vector. Rebba, et al,[44] suggest $r^* = P\left(|D_1| < \varepsilon_1 \cap |D_2| < \varepsilon_2 \cap |D_3| < \varepsilon_3 \cap \cdots \cap |D_m| < \varepsilon_m\right)$ for m number of elements and using bootstrap or analytical approximations to estimate the joint probability density functions. For the example at hand, bootstrapping is investigated and presented in Section 3.4.3. As a simpler alternative, a minimum threshold approach is implemented here, where it is required that at least 23 of the 25 elements (i.e. 92%) in each mode shape vector be within a defined ε with a minimum confidence of $r_{\min}$. Table 10 and Table 11 show the results for the healthy test article. This validation assessment was not carried out for the damaged test article since the EMA resolution was insufficient to distinguish between damaged and healthy mode shapes.

The results in Table 10 were obtained, one mode shape vector at a time, by adjusting $r_{\min}$ until at least 23 of the 25 elements in $\{\Psi_A\}$ were within ε of $\{\Psi_X\}$, where ε was fixed at 0.15 units.

From Table 10 it can be stated that all elements in $\{\Psi_A\}$ corresponding to the first mode of vibration are within 0.15 units of the elements in $\{\Psi_X\}$ with 100% confidence; 23 of 25 elements in $\{\Psi_A\}$ corresponding to the second mode of vibration are within 0.15 units of the elements in $\{\Psi_X\}$ with 3.5% confidence; and so on. Note that the mode shape vectors were normalized, such that the largest element in each mode shape vector is 1.0 unit in absolute magnitude. Again it is apparent that elements in $\{\Psi_X\}$ corresponding to coupled mode sets, modes 2 and 3, and modes 7 and 8, do not match well with their counterparts in $\{\Psi_A\}$. However, $\{\Psi_X\}$ corresponding to modes 1, 4, 5, and 6 is in good agreement with $\{\Psi_A\}$, and not much significance should be placed on the MRM values of coupled modes.

Table 10. MRM for mode shape vectors of healthy test article.

Mode #	Epsilon	Min. Model Reliability Metric	# of Passing Elements
1	0.15	1.000	25 of 25
2	0.15	0.035	23 of 25
3	0.15	0.028	23 of 25
4	0.15	1.000	25 of 25
5	0.15	1.000	25 of 25
6	0.15	0.983	23 of 25
7	0.15	1.E-11	21 of 25
8	0.15	9.E-09	23 of 25

Table 11, similar to Table 10, shows the probability levels with which the difference between corresponding elements of $\{\Psi_A\}$ and $\{\Psi_X\}$ are expected to be less than ε for the healthy test article. The results in Table 11 were obtained, one mode shape vector at a time, by adjusting ε until at least 23 of the 25 elements in that mode shape vector were equal to or greater than $r_{\min}$, which was fixed at 0.9. From Table 11 it can be stated that 23 of 25 elements in $\{\Psi_A\}$

corresponding to the first mode of vibration are within 0.0672 units of the elements in $\{\Psi_X\}$ with 90% confidence; 23 of 25 elements in $\{\Psi_A\}$ corresponding to the second mode of vibration are within 0.3048 units of the elements in $\{\Psi_X\}$ also with 90% confidence; and so on. As previously explained, the experimentally observed mode shape vectors for coupled mode sets, modes 2 and 3, and modes 7 and 8, do not compare well to their analytical counterparts and this is once again evident in the results obtained from the MRM analysis in Table 11. Analytically predicted mode shape vectors 1, 4, 5, and 6 are very comparable to their experimentally observed counterparts.

Table 11. MRM for mode shape vectors of healthy test article.

Mode #	Epsilon	Min. Model Reliability Metric	# of Passing Elements
1	0.0672	0.9	23 of 25
2	0.3048	0.9	23 of 25
3	0.3216	0.9	23 of 25
4	0.0395	0.9	23 of 25
5	0.1086	0.9	23 of 25
6	0.1474	0.9	23 of 25
7	0.9940	0.9	23 of 25
8	0.4279	0.9	23 of 25

Table 10 and Table 11 provide probabilistic comparisons between $\{\Psi_X\}$ and $\{\Psi_A\}$ for the 8 modes of vibration considered. It is easily recognized that mode shape vectors corresponding to the 1st, 4th, 5th, and 6th mode of vibration compare very well and that the elements of $\{\Psi_A\}$ are well within 0.15 units of the elements of $\{\Psi_X\}$ corresponding to those modes of vibration. At least 23 of 25 elements in $\{\Psi_A\}$ corresponding to these 4 modes of vibration are within 0.15 units of the elements in $\{\Psi_X\}$ with greater than 98% confidence.

From the MRM assessment of the SFEM it can be concluded that given an allowable difference of approximately 5%, the model predictions can be accepted with respect to natural frequency predictions (a 10% allowable difference is needed for mode 8 of the damaged test article). With respect to mode shapes, an allowable difference of approximately 15% is required to accept the model predictions with high confidence.

3.4.3 Joint-MRM via Bootstrapping

In the previous comparisons conflicting inferences were made for individual modes of vibration. In order to obtain an overall measure of how well the FEM models predict the modal properties of the test article, bootstrapping is used to estimate the joint probability density function required to calculate the joint MRM, $r*$. Rebba and Mahadevan[44] suggest $r* = P\left(\left|D_1\right| < \varepsilon_1 \cap \left|D_2\right| < \varepsilon_2 \cap \left|D_3\right| < \varepsilon_3 \cap \cdots \cap \left|D_m\right| < \varepsilon_m\right)$, where D_1 to D_m are the errors between observation and prediction of modal frequencies 1 to m, and ε_1 to ε_m are the corresponding allowable differences. Bootstrapping is a data-based simulation method for statistical inferences.[60] n_B number of bootstrap samples are generated from an original data set. Each bootstrap sample has m elements, generated by sampling with replacement m times from the original data set. Bootstrap replicates $s(x*_1)$, $s(x*_2)$, ..., $s(x*_{n_B})$ are obtained by calculating the value of the statistic $s(x)$ (in this case, the mean modal frequencies and mean mode shape vectors) on each set of bootstrap samples. Finally $r*$ is estimated by finding the ratio between the number of samples for which $\left|D_1\right| < \varepsilon_1 \cap \left|D_2\right| < \varepsilon_2 \cap \left|D_3\right| < \varepsilon_3 \cap \cdots \cap \left|D_m\right| < \varepsilon_m$ is true and n_B. Utilizing the bootstrap method in this way preserves the correlation structure inherently present

among modes of vibration and, perhaps more importantly, within each mode shape vector. The results are shown in Figure 16 and Figure 17.

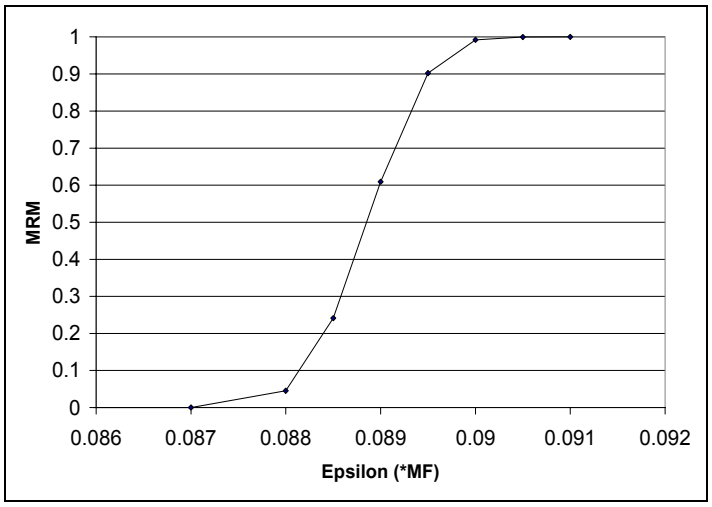

Figure 16. Bootstrap MRM for modal frequencies of damaged test article.

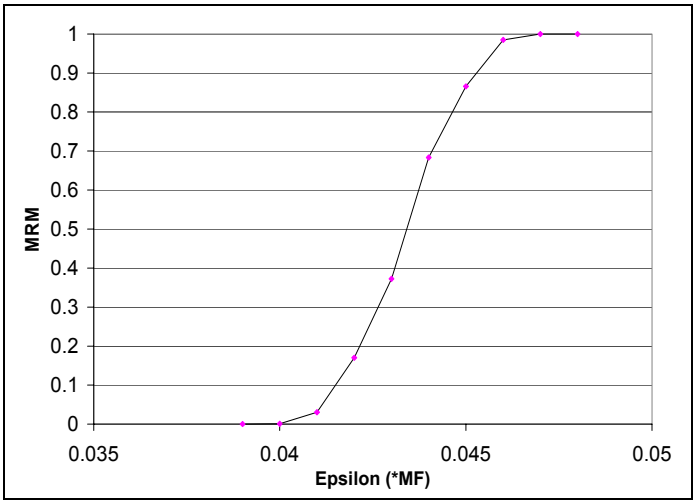

Figure 17. Bootstrap MRM for modal frequencies of healthy test article.

The plots in Figure 16 and Figure 17 show the joint cumulative probability distributions (CDF) $P\left(\left|D_1\right| < \varepsilon_1 \cap \left|D_2\right| < \varepsilon_2 \cap \left|D_3\right| < \varepsilon_3 \cap \ldots \cap \left|D_7\right| < \varepsilon_7 \cap \left|D_8\right| < \varepsilon_8\right)$ of the modal frequencies for different values of ε_i (i.e. joint-MRM). For the damaged test article, the first eight modal

frequencies as observed experimentally fall well within 10% of the corresponding mean predicted modal frequencies with 100% probability. The results shown in Figure 16 are in agreement with previous results. For the healthy test article, the first eight modal frequencies as observed experimentally and sampled via bootstrapping fall well within 5% of the corresponding mean predicted modal frequencies with 100% confidence. These results are also in good agreement with previous conclusions (i.e. an allowable difference of approximately 10% is needed to pass the model of the damaged test article, while the model of the healthy structure achieves an MRM value of 1.0 with an allowable difference of only 5%).

Figure 18 and Figure 19 show the joint cumulative probability distributions $P\left(|d_1| < \varepsilon \cap |d_2| < \varepsilon \cap \ldots \cap |d_{24}| < \varepsilon \cap |d_{25}| < \varepsilon\right)$ of the elements in the mode shape vectors of the healthy test article for different values of ε (i.e. joint-MRM) as determined via bootstrapping. Here, d_1 to d_{25} are the errors between observation and prediction of the mode shape vector elements 1 to 25, and ε the allowable difference. 23 of 25 elements of a given mode shape vector were required to have a MRM greater than or equal to a given value of ε. As it is evident from the results shown (i.e. an allowable difference of approximately 15% is required to pass all uncoupled modes of vibrations simultaneously), including the correlation structure of mode shape vectors decreases the joint probability of corresponding mode shape vectors for a given ε. The results shown in Figure 18 and Figure 19 agree with previous observations in that they clearly identify the coupled EMA modes of vibration as insufficiently similar to FEM predictions. In addition, the results also show that MRM is a stricter and more discriminating measure for validation and better specifies exact differences between model predictions and laboratory observations.

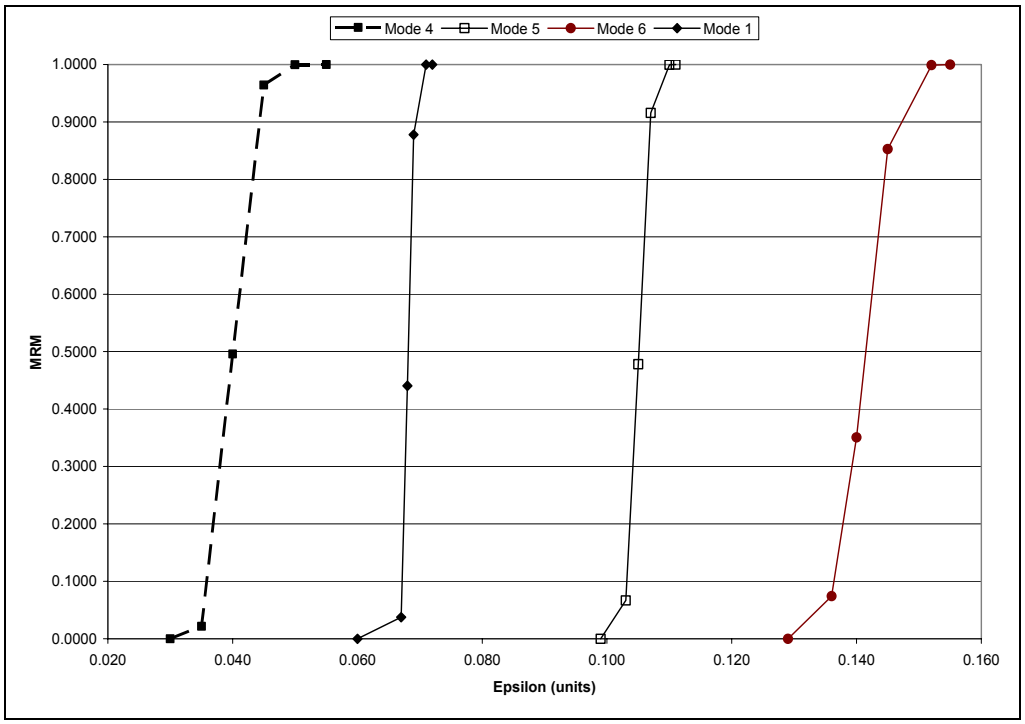

Figure 18. Bootstrap MRM for uncoupled mode shape vectors of healthy test article.

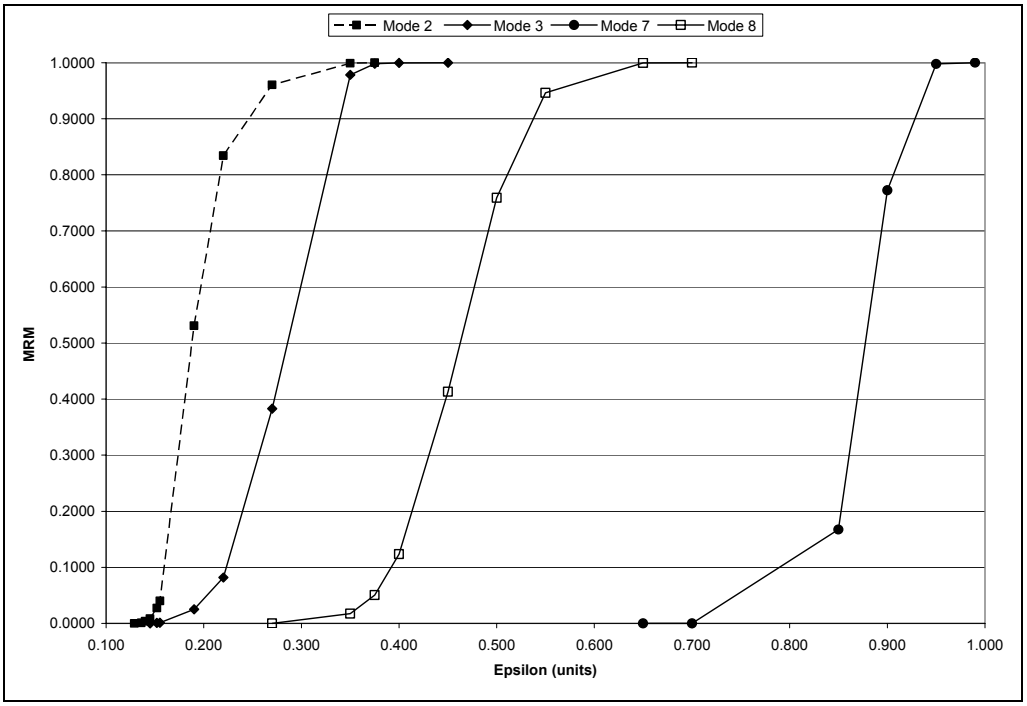

Figure 19. Bootstrap MRM for coupled mode shape vectors of healthy test article.

From the above investigations it is concluded that the calibrated analytical models produce results similar to experimentation. Natural frequency predictions are generally within 5% of observations; however, mode shape predictions require an allowable difference of approximately 15% in order to be considered equal to experimental observations. Similar to the correlation analysis of Section 3.4.1, MRM easily identified the coupled modes of vibration as insufficiently similar.

3.4.4 Classical and Bayesian Hypothesis Testing

In addition to the conclusions drawn from the applications of MAC and MRM, the discrepancies between prediction and observation are found to be statistically significant, such that classical and Bayesian hypothesis testing required the rejection of the null hypothesis, $H_0 : \mu_{prediction} = \mu_{observation}$. Table 12 shows the Bayes' factors as well as the *p*-values corresponding to a one-sample *t*-test of the first eight natural frequencies of the test article, where $n = 50$.

Table 12. Hypothesis test results of calibrated model prediction-observation comparison.

Natural Mode of Vibration	Bayes' Factor		p-Value	
	Healthy	Damaged	Healthy	Damaged
1	1.39E-195	0.00E+00	1.10E-32	2.08E-44
2	1.63E-51	1.44E-137	8.36E-10	2.90E-30
3	2.01E-131	8.85E-107	5.79E-23	9.83E-28
4	8.66E-01	1.62E-29	4.26E-04	4.60E-16
5	0.00E+00	5.31E-56	1.74E-53	1.41E-21
6	1.37	7.18E-27	0.752	2.54E-15
7	3.03E-54	6.59E-222	2.75E-21	3.71E-35
8	3.88E-09	0.00E+00	2.56E-08	1.73E-69

It should be noted that due to the limited number of experimental measurements (i.e. two samples from healthy test articles, and one sample from a damaged test article), the mean of the observations of the natural frequencies of the experimental modal analysis is considered constant for the application of classical and Bayesian hypothesis testing. Note that due to the limited number of experimental measurements, laboratory observations are considered to be constant for the application of classical and Bayesian hypothesis testing (hence a one-sample *t*-test).

3.4.5 Conclusions

Calibration via systematic perturbation of several model input parameters identified the previously defined models (of healthy and damaged test article) as best by assessment via the validation metrics of Section 3.2. It can be concluded that the calibrated model predictions are highly correlated with experimental observations and within small allowable differences of experimental observations; however, model predictions and experimental observations are statistically different.

A more highly refined mesh of the finite element model and a more detailed modeling of the bolted fastening mechanism of the test article might produce results in better agreement with experimental observations; however, model size, run time, and output storage capacity requirements were significant constraints with respect to the model's consequent use. These issues had to be taken into consideration when it was concluded that the stochastic FEM model produced results sufficiently similar to experimental observation, such that the models can be considered calibrated and one could proceed with model utilization in the next step: independent model validation.

3.5 Independent Model Validation

Additional independent experimental modal analyses (EMA) were performed to obtain the experimental observations of Table 13. Due to the restrictions associated with EMA resolution it proved prohibitive to obtain estimates for modal frequencies and corresponding mode shapes greater than approximately 900Hz. Note that modes of vibration greater than 900Hz were previously obtained (Table 2); however, due to changes in laboratory equipment/conditions, the capability to detect modes of vibration higher than 900Hz was not available during independent EMA testing. Therefore only the first six modes of vibration are included in the independent model validation. It should also be noted that previously, no calibration comparisons were made in regard to a free-free suspended test article condition. During independent EMA testing, natural frequencies of the test article in a free-free suspended state were extracted. The natural frequencies corresponding to the healthy, damaged, and free-free suspended structural conditions are listed in Table 13 for two test article specimens. The mean mode shape vectors corresponding to the healthy and damaged structural conditions are provided in Table 14. These independent experimental observations are compared to the calibrated model predictions of Table 4 and Table 5.

In addition, Table 15 provides the natural frequencies of the test article in healthy and free-free suspended states as defined by Blevins.[61] Blevins' formulations for the exact natural frequencies of rectangular plates are derived from the numerical results of Leissa[62] and assume ideal material, geometric, and boundary conditions. Therefore the results in Table 15 are provided here only for guidance, where the healthy condition is considered to be a point supported plate. A point support boundary condition applies translational constraints at the point of application, but places no restrictions on the rotation of the plate about that point. The test article in the

healthy condition, however, is fully bolted to the optical table via bolts and washers, which certainly constrain the plate to some degree in both translation *and* rotation at each bolt location.

Table 13. Independent EMA modal frequency results (Hz).

Mode of Vibration	1	2	3	4	5	6
1st Independent EMA - Healthy	227.1	411.7	411.7	472.8	838.7	937.5
2nd Independent EMA - Healthy	226.7	410.9	410.9	471.2	840.8	939.7
1st Independent EMA - Damaged	225.7	410.3	410.3	470.8	837.5	934.1
2nd Independent EMA - Damaged	224.2	407.8	407.8	466.7	838.6	933.5
1st Independent EMA - Free	215.5	320.6	404.8	560.8	560.8	
2nd Independent EMA - Free	214.5	319.1	406.1	559.5	559.5	

Table 14. Mean mode shape vectors of independent EMA of healthy and damaged test article.

	Healthy Test Article						Damaged Test Article					
Mode	1	2	3	4	5	6	1	2	3	4	5	6
Mean Mode Shape Vectors	0.023	-0.015	-0.015	-0.003	0.021	-0.033	0.023	-0.016	-0.016	-0.003	0.020	-0.038
	-0.262	0.526	0.526	-0.521	-0.533	0.926	-0.259	0.527	0.527	-0.519	-0.517	0.936
	-0.522	0.987	0.987	-0.945	-0.983	-0.033	-0.520	1.000	1.000	-0.950	-0.970	-0.111
	-0.266	0.554	0.554	-0.522	-0.520	-0.929	-0.272	0.554	0.554	-0.559	-0.563	-0.851
	0.022	-0.009	-0.009	-0.002	0.015	0.041	0.039	-0.034	-0.034	-0.002	0.035	0.092
	-0.245	-0.049	-0.049	0.509	-0.521	0.746	-0.243	-0.278	-0.278	0.560	-0.552	0.697
	-0.628	0.306	0.306	0.007	-0.043	0.985	-0.621	0.258	0.258	0.025	-0.031	0.948
	-0.849	0.566	0.566	-0.299	0.242	-0.009	-0.841	0.560	0.560	-0.295	0.254	-0.007
	-0.637	0.407	0.407	0.012	-0.032	-1.000	-0.640	0.417	0.417	0.013	-0.050	-1.000
	-0.257	0.085	0.085	0.565	-0.518	-0.813	-0.286	0.301	0.301	0.569	-0.564	-0.822
	-0.501	-0.144	-0.144	0.965	-1.000	0.197	-0.491	-0.437	-0.437	1.000	-1.000	0.034
	-0.823	-0.078	-0.078	0.311	0.221	0.008	-0.816	-0.269	-0.269	0.333	0.218	0.008
	-1.000	0.009	0.009	-0.003	0.879	-0.003	-1.000	0.012	0.012	-0.001	0.883	-0.020
	-0.832	0.031	0.031	0.328	0.224	-0.008	-0.838	0.292	0.292	0.286	0.237	-0.009
	-0.510	0.063	0.063	1.000	-0.952	-0.110	-0.529	0.516	0.516	0.927	-0.940	-0.163
	-0.242	-0.105	-0.105	0.503	-0.490	-0.822	-0.232	-0.234	-0.234	0.535	-0.511	-0.752
	-0.621	-0.396	-0.396	-0.016	-0.036	-0.894	-0.613	-0.412	-0.412	-0.015	-0.039	-0.876
	-0.833	-0.554	-0.554	-0.316	0.188	-0.016	-0.823	-0.547	-0.547	-0.331	0.197	-0.021
	-0.634	-0.315	-0.315	0.007	-0.038	0.903	-0.627	-0.264	-0.264	0.031	-0.041	0.938
	-0.249	0.016	0.016	0.529	-0.497	0.831	-0.253	0.272	0.272	0.521	-0.510	0.930
	0.027	0.008	0.008	-0.003	0.041	0.022	0.030	0.001	0.001	-0.002	0.046	0.016
	-0.256	-0.530	-0.530	-0.508	-0.459	-0.793	-0.250	-0.515	-0.515	-0.523	-0.503	-0.741
	-0.529	-1.000	-1.000	-0.939	-0.945	0.047	-0.521	-0.966	-0.966	-0.962	-0.984	0.050
	-0.263	-0.531	-0.531	-0.518	-0.526	0.781	-0.247	-0.505	-0.505	-0.532	-0.536	0.711
	0.017	0.007	0.007	-0.001	0.022	-0.026	0.019	0.007	0.007	-0.002	0.025	-0.023

Table 15. Natural frequencies via Blevins' formulation (Hz).

Mode of Vibration	1	2	3	4	5
Free-Free Boundary Condition	217.916	319.686	394.64	565.711	565.711
Point Supported Plate	208.224	318.071	318.071	387.21	

The validation metrics of Section 3.2 are again utilized (now for actual model validation as oppose to model calibration/assessment), and the details of their implementation are provided below along with general discussions and conclusions regarding the predictive capabilities of the SFEM.

Independent validation is first investigated by plotting the experimentally observed modal frequency value against the predicted one for each of the 6 modes included in the comparison. The plots, along with trend lines and R^2-values are shown in Figure 20. From the plots in Figure 20 it can be concluded that the independent experimentally obtained natural frequencies of the test specimen are highly correlated with calibrated model predictions, similar to the results of Figure 14. In addition, the 6x6 MAC-matrix in Table 16 is constructed to quantitatively compare the predicted and independently observed mode shapes of the healthy test article. The results are strikingly similar to those shown in Table 7, where paired/coupled modes 2 and 3 again stand out as abnormal due to EMA's inability to clearly differentiate the mode shapes of these paired modes. EMA lumps coupled modes into a single combined mode shape, causing the experimental results to include contributions from both of the paired modes. As stated previously, it is unwise to place much significance on the MAC values of coupled modes. The MAC values of the remaining four modes of vibration – namely the first, fourth, fifth, and sixth – are all greater than 0.98 leading to conclude that the mode shapes extracted via independent EMA tests are highly correlated with calibrated analytical predictions.

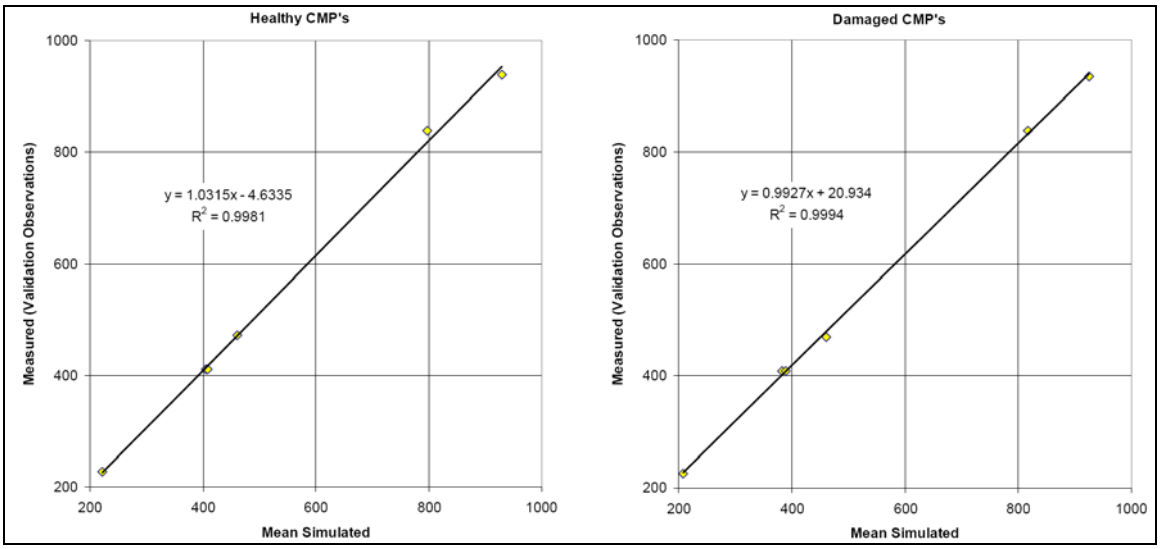

Figure 20. Plots of correlated mode pairs for validation of SFEM (axes show frequency - Hz).

Table 16. MAC matrix for the healthy model for validation of SFEMs.

		Experimental Mode Shape Number					
		1	2	3	4	5	6
Predicted Mode Shape Number	1	0.998	0.000	0.000	0.000	0.032	0.000
	2	0.000	0.992	0.992	0.000	0.000	0.000
	3	0.000	0.966	0.966	0.000	0.000	0.000
	4	0.000	0.000	0.000	0.999	0.000	0.000
	5	0.064	0.001	0.001	0.000	0.997	0.000
	6	0.000	0.000	0.000	0.000	0.000	0.984

Applying the model reliability metric as defined in Equation (8) to the independently observed results of the test article in the healthy condition produces the results shown in Table 17. Results are provided for ε equal to 6%, 5%, 4%, 3%, 2%, and 1% of the corresponding modal frequencies, MF. Table 17 indicates that the mean frequencies of all modes of vibration as observed through independent experimental measurements of the healthy test article are within 6% of the corresponding predicted modal frequencies with 100% probability. These results are in good agreement with previous calibration evaluations, where the first 6 modes of vibrations as observed via EMA are within 5% of the corresponding predicted modal frequencies with 100% probability.

Table 17. MRM for validation of modal frequencies of the healthy test article.

Mode #	Epsilon					
	0.06*MF	0.05*MF	0.04*MF	0.03*MF	0.02*MF	0.01*MF
	r	r	r	r	r	r
1	1.000	1.000	1.000	1.000	0.823	0.000
2	1.000	1.000	1.000	1.000	1.000	0.004
3	1.000	1.000	1.000	1.000	1.000	0.999
4	1.000	1.000	1.000	1.000	0.036	0.000
5	1.000	0.062	0.000	0.000	0.000	0.000
6	1.000	1.000	1.000	1.000	1.000	0.472

Also applying MRM as defined in Equation (8) to the independently observed results of the damaged test article yields the results shown in Table 18, where ε takes on values of 8%, 6%, 5%, 4%, 3%, 2%, and 1% of the corresponding modal frequencies, MF. It should be noted that an allowable difference of 10% of MF is required to yield a MRM of 100% for the first mode of vibration. The results of Table 18 are similar to previous calibration comparisons, where also an allowable difference of 10% was required to yield an MRM of 1.00.

Table 18. MRM for validation of modal frequencies of the damaged test article.

Mode #	Epsilon						
	0.08*MF	0.06*MF	0.05*MF	0.04*MF	0.03*MF	0.02*MF	0.01*MF
	r	r	r	r	r	r	r
1	0.496	0.000	0.000	0.000	0.000	0.000	0.000
2	1.000	0.008	0.000	0.000	0.000	0.000	0.000
3	1.000	0.995	0.321	0.000	0.000	0.000	0.000
4	1.000	1.000	1.000	1.000	0.995	0.654	0.037
5	1.000	1.000	1.000	1.000	1.000	0.000	0.000
6	1.000	1.000	1.000	1.000	1.000	1.000	0.467

In addition, the application of classical and Bayesian hypothesis testing on the natural frequencies of both healthy and damaged test articles again results in the rejection of the null hypothesis, $H_0 : \mu_{prediction} = \mu_{observation}$, similar to previous calibration evaluations. Table 19 shows the Bayes' factors as well as the *p*-values corresponding to a one-sample *t*-test of the first

six natural frequencies of the test articles, where $n = 50$. It should again be pointed out that due to the limited number of experimental measurements (i.e. two samples from healthy test articles, two samples from damaged test articles), the mean of the independent observations of the natural frequencies of the experimental modal analysis is considered constant for the application of classical and Bayesian hypothesis testing.

Table 19. Classical hypothesis test results for model validation.

Natural Mode of Vibration	Bayes' Factor		p-Value	
	Healthy	Damaged	Healthy	Damaged
1	2.55E-157	0.00E+00	1.26878E-31	2.22E-69
2	1.48E-104	0.00E+00	1.58606E-27	7.36E-47
3	4.08E-20	0.00E+00	3.72713E-13	4.10E-54
4	1.70E-249	7.35E-59	2.24682E-36	4.93E-22
5	0.00E+00	1.99E-254	1.03658E-56	1.40E-36
6	5.76E-205	6.34E-85	2.4592E-34	1.70E-25

3.6 Validation Conclusions

In general, the results of the independent model validation yield conclusions similar to those drawn from the model evaluation comparisons of Section 3.4. The calibrated model predictions are highly correlated with independent experimental observations and within small "allowable" differences of independent experimental observations. However, the difference between the calibrated model predictions and the independent experimental observations is statistically significant.

The plots in Figure 21 and Figure 22 show the mean and 95% confidence bounds of the calibrated SFEM predictions (labeled "P"), the first set of EMA observations (labeled "1st"), which was utilized to calibrate the SFEM, and the second set of independent EMA observations (labeled "2nd"), which was utilized for validating the SFEM. The first six modal frequencies of

the healthy and damaged test article are shown. It can be seen that the SFEM of the healthy test article generally over-predicted the natural frequencies of the first set of observations (with a few exceptions), while consistently under-predicting the modes of vibration of the second independent set of observations. For the SFEM of the damaged test article, these trends are not as pronounced: generally the model consistently under-predicts the natural frequencies of both sets of observations with very few exceptions.

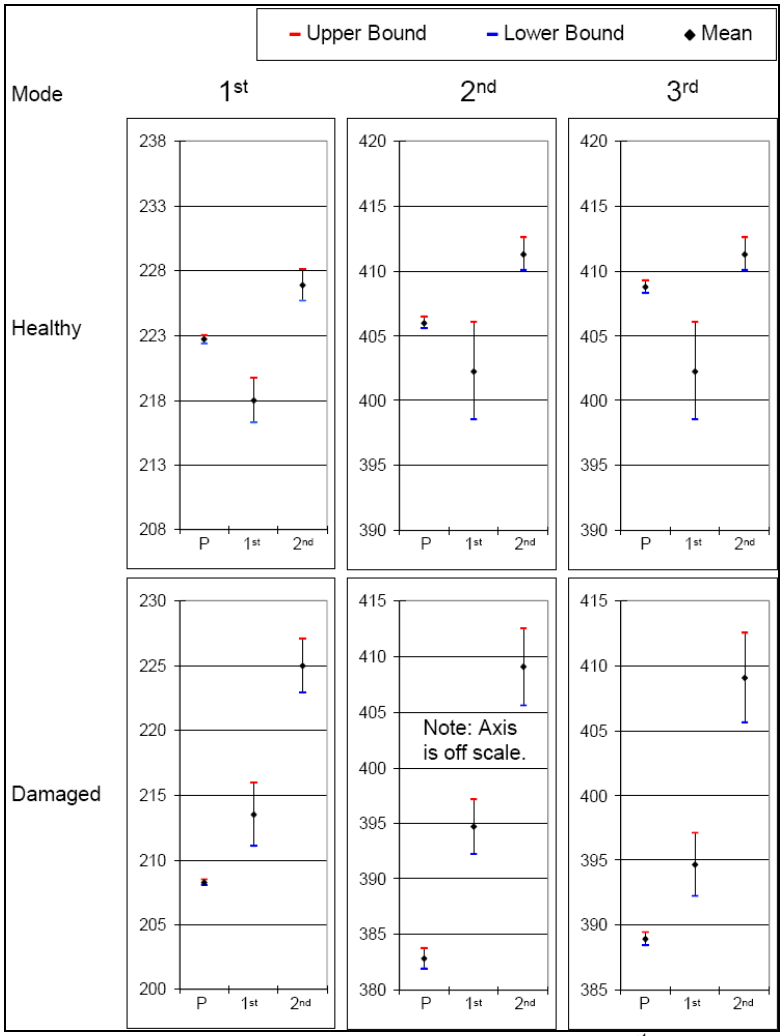

Figure 21. General comparison of predictions (P), first set of observations (1st), and second set of observations (2nd) for modes of vibration 1, 2, and 3. Natural frequencies are shown along the vertical axis in Hz.

Note that confidence bounds for the damaged test article of the first set of experimental observations were constructed utilizing the EMA resolution limit of 0.625Hz as the standard deviation.

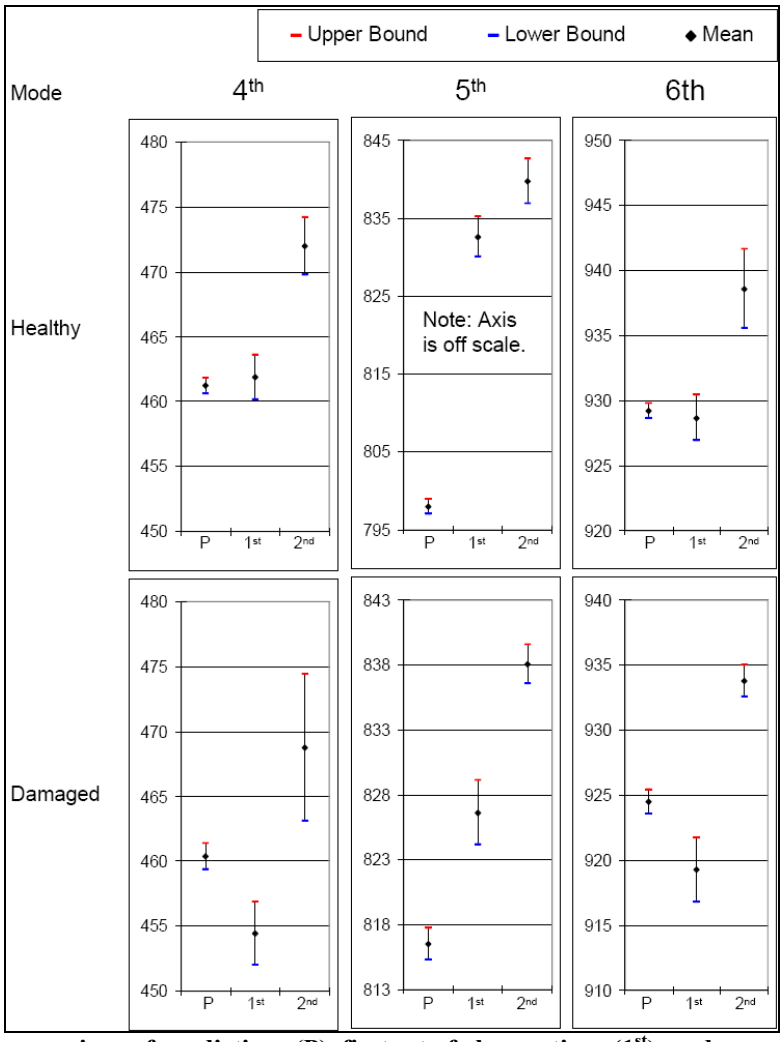

Figure 22. General comparison of predictions (P), first set of observations (1st), and second set of observations (2nd) for modes of vibration 4, 5, and 6. Natural frequencies are shown along the vertical axis in Hz.

It cannot be concluded that the models are validated; however, due to the high correlation that exists between the predicted modes of vibration (modal frequencies and mode shapes) and EMA results, as well as the consideration of modeling constraints (model size, run time, and output

storage capacity), the SFEM analyses do have some level of predictive capability. Later chapters of this dissertation show that this level of predictive capability is insufficient for the subsequent use of the SFEM; however, for sake of demonstration and developing the general methodology of SPO under uncertainty, the SFEM as defined in this chapter and in Chapter 2 will be utilized.

CHAPTER IV

SHM SENSORS AND DAMAGE DETECTION

This chapter relates to Objective 2 and focuses on identifying a damage detection method most effective for the example application. Section 4.1 introduces the SHM sensors utilized during the experimental work of this study, while Section 4.2 reviews damage detection methods. Section 4.3 defines several sensor layout performance measures, which are utilized for evaluating different damage detection methods. Section 4.4 introduces the three components of damage detection – feature extraction, features selection, and state classification – and investigates different combinations for use with the example application. The most effective damage detection methodology is identified in Section 4.5 based on the performance measures defined in Section. 4.3.

4.1 Sensors

Several candidate sensor technologies for the use in SHM systems have been developed. Besides traditional strain gages, thermocouples, and accelerometers, these include fiber-optic sensors,[63] active and passive ultrasonic sensing methods, and some remote wireless technologies and non-contact sensing architectures.[64] In addition, in-situ sensor systems for high temperature applications have been developed.[65] Currently in wide use and utilized in the laboratory experiments of this study, surface-bonded piezoelectric sensors are applied extensively in experimental settings and are well defined in regard to performance characteristics, operability, durability, and survivability under widely varying environmental conditions.[66,67,68] The

popularity of piezoelectric sensor technology is directly related to a set of inherent advantages. The high modulus of elasticity of many piezoelectric materials is comparable to that of many metals and, although piezoelectric sensors are electromechanical systems that react on compression, the sensing elements show almost zero deflection. This is the reason why piezoelectric sensors are robust, have an extremely high natural frequency, and an excellent linearity over a wide amplitude range. Additionally, piezoelectric technology is insensitive to electromagnetic fields and radiation, enabling measurements under harsh conditions. Some piezoelectric materials such as galliumphosphate or tourmaline are extremely stable over a large temperature range enabling sensors to have a working range of 1000°C. The single disadvantage of piezoelectric sensors is that they cannot be used for true static measurements. A static force will result in a fixed amount of charges on the piezoelectric material. Working with conventional electronics, which include imperfect insulating materials, a reduction in internal sensor resistance will result in a constant loss of electrons, yielding an inaccurate signal. Elevated temperatures cause an additional drop in internal resistance; therefore, at higher temperatures, piezoelectric materials that maintain a high internal resistance must be used; however, there are numerous applications that show quasi-static measurements while there are other applications that go to temperatures far beyond 500°C.[69]

In addition to sensors, a major component of SHM systems is the data analysis and signal/information processing of the structural responses collected via SHM sensors. Algorithms that process the data/signals retrieved by SHM sensor networks are generally known as damage detection methods. The remainder of this chapter deals with damage detection and develops a method for sensor layout performance prediction, which is subsequently used for sensor placement optimization (SPO).

4.2 Damage Detection

Damage detection and location identification algorithms include wavelet-based approaches[70], two-stage modal frequency analysis[71], and methods for eddy-current-based damage detection[72]. Also, several methods for structural damage detection use energy dissipative devices, which guarantee closed-loop stability[73]. Property matrix updating, nonlinear response analysis, and damage detection using neural networks are all methods used to manipulate the information gathered by the SHM sensor system for decision making.[7] A comprehensive review of state-of-the-art damage detection and location identification algorithms is provided by Doebling, et al.[7]

Most of the structural damage detection methods and algorithms found in the literature examine the changes in the measured structural vibration response and analyze the modal frequencies, mode shapes, and flexibility coefficients of the structure. This examination of a structure's vibration characteristics can be done actively or passively. During active investigation the structure is excited, usually using one or more piezoelectric actuators and the vibration response is recorded via several, usually piezoelectric, sensors. When the structure is examined passively, sensors are used to record the structure's response due to its own operational excitation from propulsion systems, aerodynamic excitations, or other vibrations.[3]

The signal analysis procedure employed in this study follows the general concepts of Duda, Hart, and Stork[8] and utilizes the feature extraction and state classification methodologies defined by DeSimio, et al.[9] A statistical pattern recognition methodology is employed, where the process begins by simulation via finite element models an applied vibration signal on the test article, such is the case in active SHM approaches. The structural responses from a probabilistic FEM analysis are recorded, such that the statistics of the model outputs are quantified for all SFEM

locations for the damage conditions of interest, and are stored with corresponding structural state information.

Structural response analysis is needed to estimate probabilistic sensor layout performance measures such as the probability of correctly classifying the structural state of a component or system for a given sensor layout, x (i.e. $P(CC) = P(\text{classify structure as } \omega_i \mid \text{structural state is } \omega_i)$). This can be accomplished via any appropriate diagnostics signal analysis procedure (i.e. damage detection algorithm). For the damage detection approach utilized in this study, a set of measurements or features are computed from the responses and associated with the corresponding structural state. The resultant information provides labeled data for classifier design, which involves the specification of discriminant functions estimated from the statistics of the features corresponding to the structural states of interest. The responses utilized for classifier design are known as the "training data set." The performance of the designed classifier is estimated by applying repeated analyses using different realizations, known as the "testing data set," of the random inputs to healthy and damaged structural SFEM and their respective state classification to construct a classification matrix from which several probabilistic performance measures, such as $P(CC)$, can be estimated. Section 4.3 outlines the method for estimating sensor layout performance.

4.3 Sensor Layout Performance Measures

An appropriate damage detection algorithm (as will be defined in Section 4.5 for the example application considered in this study) is applied to sets of independent testing data corresponding to the previously identified structural states of interest: one healthy and four loose bolt conditions of the test article. This yields a classification matrix corresponding to a given sensor layout, x,

from which several performance measures may be estimated. The general form of a classification matrix corresponding to a particular sensor configuration is shown in Table 20.

Table 20. Sample classification matrix for a given sensor layout.

		Classified States				
		Damaged 1	Damaged 2	Damaged 3	Damaged 4	Healthy
True States	Damaged 1	CM11	CM12	CM13	CM14	CM15
	Damaged 2	CM21	CM22	CM23	CM24	CM25
	Damaged 3	CM31	CM32	CM33	CM34	CM35
	Damaged 4	CM41	CM42	CM43	CM44	CM45
	Healthy	CM51	CM52	CM53	CM54	CM55

Using the information contained in the classification matrix, one can estimate the probability of false alarm (Type I Error), the probability of missed detection (Type II Error), the probability of correct classification (Accuracy), and the probability of misdetection (1-Accuracy).[74] $P(\text{False Alarm})$ is defined as the likelihood that the damage detection algorithm classifies a healthy structure as damaged. $P(\text{Missed Detection})$ is the probability that the damage detection method classifies a damaged structure as healthy. Accuracy is measured via $P(\text{Correct Classification})$, which is defined as the probability that the damage detection method will classify a given structure correctly into its proper structural state (i.e. $P(\text{classify structure as } \omega_i \mid \text{structural state is } \omega_i)$). The complement of $P(\text{Correct Classification})$ is $P(\text{Misdetection})$. These probabilities can be used to evaluate a given sensor array. The performance measures are defined as follows.

$$P(\text{False Alarm}) = \frac{\text{Sum of First 4 Elements in Row 5 of CM}}{\text{Sum of All Elements in Row 5 of CM}} = P(TypeI) \quad (9)$$

$$P(\text{Missed Detection}) = \frac{\text{Sum of First 4 Elements Column 5 of CM}}{\text{Sum of All Elements in Column 5 of CM}} = P(TypeII) \quad (10)$$

$$P(\text{Correct Classification}) = \frac{\text{Sum of Diagonal Elements of CM}}{\text{Sum of All Elements of CM}} = P(CC) \quad (11)$$

$$P(\text{Misdetection}) = 1 - P(\text{Correct Detection}) \quad (12)$$

These performance measures can be used to evaluate and assess a given damage detection method, where $P(CC)$ should be maximized, while $P(TypeI)$ and $P(TypeII)$ should be minimized. In order to construct a classification matrix, a particular sensor configuration, x, must be specified. Each sensor layout, x, is uniquely defined by the six coordinates that identify the location of sensors S2, S3, and S4 in Figure 1b. That is $x = (S2_x, S2_y, S3_x, S3_y, S4_x, S4_y)$.

In order to objectively evaluate the different damage detection methods that are presented in this chapter, the performance measures of Equations (9) through (11) are evaluated for multiple sensor configurations (i.e. investigating damage detection methods via the above defined performance measures for *several* sensor configurations provides a thorough evaluation of the damage detection methods in general, and not just with respect to one particular sensor layout). Figure 23 and Table 21 provide five randomly selected sensor configurations for the investigation of damage detection methods.

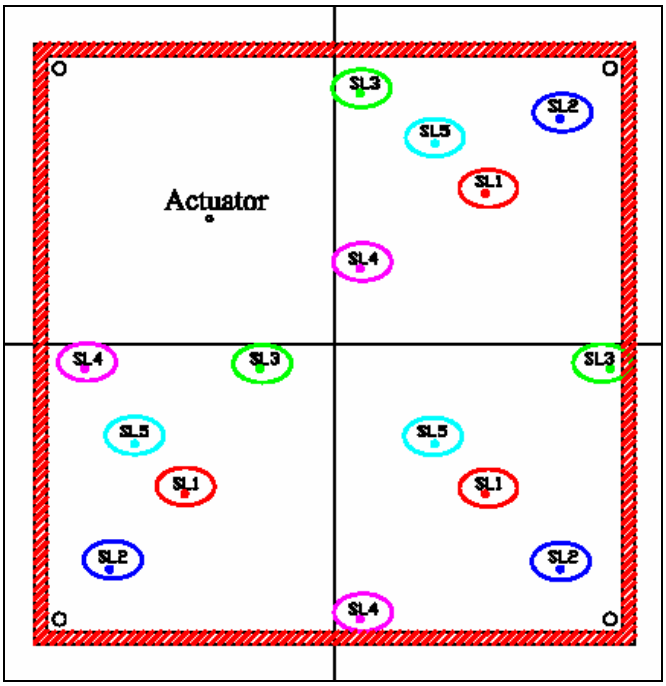

Figure 23. Five randomly selected sensor layouts.

Table 21. Randomly selected sensor layouts shown in Figure 23.

Sensor Layout	Coordinates of Sensors w/r to bottom, left corner of plate		
	S2	S3	S4
SL1	(9.0, 9.0)	(9.0, 3.0)	(3.0, 3.0)
SL2	(10.5, 10.5)	(10.5, 1.5)	(1.5, 1.5)
SL3	(6.5, 11.0)	(11.5, 5.5)	(4.5, 5.5)
SL4	(6.5, 7.5)	(6.5, 0.5)	(1.0, 5.5)
SL5	(8.0, 10.0)	(8.0, 4.0)	(2.0, 4.0)

Section 4.4 introduces the basic components of damage detection and discusses different damage detection methods. Section 4.4.5 implements several of these damage detection algorithms and assesses their efficiency with respect to the probabilistic performance measures defined in this section in order to identify the most appropriate damage detection method for the example application of the test article. The most effective signal processing method is specified in great detail in Section 4.5, where the damage detection algorithm specific parameters are provided.

4.4 Signal Analysis, Feature Extraction, and State Classification

Generally, there are three components that make up damage detection methods (DDM): (1) feature extraction, (2) feature selection, and (3) state classification. This section of Chapter 4 introduces these components and supplementary signal processing techniques and strategies, which aid in implementing the three basic DDM operations. Different combinations of these operations are evaluated using the probabilistic performance measures of Equations (9) through (11).

4.4.1 Introduction to Feature Extraction

The basic objective of feature extraction is to find a transformation, which transforms *n*-dimensional observations into smaller *m*-dimensional features, which retain (and perhaps clarify) the information required for state classification. Although many such transformations are problem specific and are often suggested by the physics involved in obtaining a particular observation, several "automatic" methods for determining features include principal component analysis (PCA), Fisher criterion minimization, entropy maximization or minimization, divergence analyses, as well as Bhattacharya distance analysis.[75,76] These linear transformations use certain 'optimal' properties of the eigenvalues and eigenvectors of the correlation matrices of observed response signals to describe their sufficient statistics or features. While reducing the dimension of the observation space, these optimal properties ensure that there is no increase in the minimum probability of error (i.e. probability of misclassification).[75] That is to say, an optimal feature set contains all the information present in the observation space that is relevant to pattern recognition and state classification.

Nonlinear feature extraction methods are divided into two general groups: 1) computationally intensive iterative algorithms[75], and 2) efficient but less accurate noniterative mapping methods. Noniterative, nonlinear mapping feature extraction methods have been proposed by Sammon[77] and by Koontz and Fukunaga.[78] These methods attempt to identify the inherent structure of the data in *n* dimensions and find a nonlinear transformation to a *m*-dimensional feature set $(m < n)$ that 'more-or-less' preserves that structure.[75]

Other, less automatic, but perhaps with a clearer physical interpretation, feature extraction methods are derived from power spectral density functions, auto- and cross- correlation functions, transfer functions, or probability density estimations. Several of these methods are described in the following sub-sections.

4.4.1.1 Auto- and Cross-Correlation Based Features

Auto- and cross-correlation based features are established in the time-domain and are derived from the auto-correlation and cross-correlation functions of the measured response signal of the structure. Assuming, for example, that the response time histories from three locations are being used (such as the case in the example application of this study), three auto-correlation and three cross-correlation functions may be computed. The envelopes of these functions are computed, where the envelope, $A(t)$, of a function, $x(t)$, is defined as a pair of smoothly varying curves such that $|A(t)| \geq |x(t)|$ for all t and $|A(t)| = |x(t)|$ at, or very nearly at, the peaks of $x(t)$.[79] DeSimio, et al,[9] for example, then estimate the second through fifth central moments of the envelopes of the auto-correlation and cross-correlation functions providing a total of 24 features. The first central moment is purposely omitted since it will assume a value of zero for auto- and cross- correlation functions. In addition, central moments of order higher than five lack physical interpretation and are also omitted.

4.4.1.2 Frequency Domain-Based Features

Features based in the frequency-domain are extracted from the power spectral density (PSD), $S(\omega)$, of a given signal $x(t)$. $S(\omega)$ is the discrete time Fourier transform (DTFT) of the autocorrelation function $R(k)$:[80]

$$S(\omega) = T \sum_{k=-\infty}^{\infty} R(k) e^{-i 2\pi \omega k T} \tag{13}$$

Sampling frequency and sampling interval, T, are important and require careful selection when analyzing a signal and extracting features in the frequency domain. In addition, to obtain a more representative PSD estimate, the signal $x(t)$ may be divided into bins of size n_b with a specified overlap (usually, but not necessarily, 50%). Each bin is windowed (for example, with a Hamming window) and modified periodograms are computed and averaged. This method of estimating the PSD is the well-known Welch method and provides a smoothed spectral density estimate.[81] It is also a clever way to reduce the number of measurements, which is always a desired goal of feature extraction algorithms. Depending on the length of the PSD (i.e. n_b), the measurements may be used directly as features. Should the length of the PSD be considerable, an additional dimensionality reduction may be required.

Extensions to the frequency domain based features defined above are coherence function based features, which may be obtained by taking measurements at discrete values of ω of the following modified coherence function (MCF):

$$\gamma^2(\omega) = \frac{|G_{XY}(\omega)|^2}{G_{XX}(\omega) \cdot G_{YY}(\omega)}, \tag{14}$$

where X is the input signal, Y is the response signal, and $G_{IJ}(\omega)$ is the cross-spectral density of signals I and J. When $I = J$, $G_{IJ}(\omega)$ is the auto-spectral density function. Values of MCF are

calculated from each possible combination of two responses at a time from observed structural responses as signals X and Y. Assuming that the response time histories from three sensors are being used, this signal analysis feature extraction procedure yields six unique MCF. Calculating the first few central moments of these coherence functions may also be another way to reduce the number of features and capture general properties of the MCF.

4.4.1.3 Time Domain-Based Features

In this method, the response signals are discretized in the time domain into bins containing perhaps 100 to 300 data points. The standard deviation is calculated for each bin and is directly used as a feature. Depending on how many data points make up the response signal (i.e. at which frequency data is observed and for how long), this procedure will yield a feature vector with a dimension anywhere between 100 and 500 or higher. This would certainly cause the "curse of dimensionality," which refers to the problems associated with multivariate data analysis as the dimensionality of the feature space increases,[82] to take effect and a feature selection process or dimensionality reduction routine such as principle component analysis (PCA) must be implemented.

The above procedure is based on the following idea. Due to the often-used linear frequency sweep excitation function, the temporal response signal will have a large standard deviation for time intervals (bins) during which the structure is excited at a frequency that closely resembles one of its modal frequencies. Due to the fact that the damaged structure will have different modal frequencies, the response of a damaged structure will have large standard deviations in different bins. In addition to being physics based, this signal analysis procedure and feature extraction method is much less computationally intensive. Also note that other energy based descriptors may be calculated for each bin of the discretized response signals.

4.4.1.4 Transfer Function-Based Features

The transfer function of a system is defined as the ratio between the discrete time Fourier transforms (DTFT) of an output signal, $x(t)$, and its corresponding input signal, $y(t)$:[80]

$$H(f) = \frac{X(f)}{Y(f)} \tag{15}$$

where $X(f)$ and $Y(f)$ are the DTFT of $x(t)$ and $y(t)$, respectively. The coefficients of an autoregressive model of $H(f)$ could then be used as features. Other transfer function approaches utilize the parameter changes of interval models.[83] Alternatively, calculating the first few moments of transfer functions, or perhaps the central moments of the envelopes of transfer functions, obtained from one input signal and several output signals, may represent desirable features.

4.4.2 Introduction to Feature Selection

In addition to feature extraction, further signal processing defined as feature selection can be beneficial. Feature selection provides a subset of N_{opt} features from the *m*-dimensional feature pool most effective for state classification. In general, the fewer features used in a classifier, the more likely the training set performance will be representative of test set performance.[9] This is directly related to the "curse of dimensionality."[82] Optimal methods such as an exhaustive search or the Branch-and-Bound method, which is restricted by the monotonous criteria, are computationally cumbersome for problems of large dimensions. Therefore, more efficient feature selection methods such as sequential backward selection and its counterpart sequential forward selection methods, and Plus-*l*-Minus-*r*[84] search may be utilized. It has been shown that the most effective known suboptimal methods are currently the sequential floating search

methods.[85] Feature selection utilized in this research is performed with sequential forward selection.

4.4.2.1 Sequential Floating Forward Feature Selection

A brief description of the sequential floating forward selection method is provided here. See References 84 and 85 for more detailed derivations. The selection process is initialized by setting the current optimal feature set to the empty set. A 'best' feature is added to the optimal feature set by determining the feature which provides the highest quality metric. A quality metric, usually related to classification accuracy, must be chosen. The current optimal feature set and its corresponding quality metric are saved for comparison in the subsequent step, which is initiated by determining the 'worst' feature. The 'worst' feature is defined as the one, which when removed from the current optimal feature set, provides the greatest increase in the quality metric. The optimal feature set and its corresponding quality metric set from this step are also saved. The quality metrics of the candidate feature sets obtained by adding the 'best' and removing the 'worst' features are compared. The feature set that provides the largest quality metric is chosen. The feature selection continues until a stopping criterion is reached, which typically is an upper bound on the number of features to be used, or until the quality metric stops increasing.[9] The resulting N_{opt} features are used in state classification.

A key element of any feature selection method is the quality metric. Since the ability to classify signals from practical applications, which are not available during the training phase of the damage detection method (DDM) is critical to its performance, the following approach is generally utilized. First, the training data set is randomly partitioned into two subsets with equal number of signals in each state. For a given current optimal feature set, the classifier is trained using one of the two subsets and tested on the other, and vice versa. A quality metric or

performance measure, such as the ones defined in Section 4.3, may then be calculated and averaged over both subsets and utilized for feature selection. This kind of cross validation during the feature selection training phase appears to increase the robustness of the N_{opt} features in applications to practical situations.[9]

4.4.3 Introduction to State Classification

State classification or pattern recognition deals with the assigning of a response signal obtained from a structure to a given state via feature measurements. The goal of the classifier is to assign the signal to a state or category such that feature measurements for signals in the same category are sufficiently similar and appropriately different for signals in different categories.[8] Bayesian decision theory is the fundamental statistical approach to state classification and provides optimal performance.[8] That is to say, Bayes decision rule minimizes the probability of misclassification (i.e. $P(error \mid x)$ is minimized, where $P(error \mid x) = \begin{cases} P(state_k \mid x) \text{ if classified as } state_j \\ P(state_j \mid x) \text{ if classified as } state_k \end{cases}$ for all $k \neq j$, and x is a vector containing the features extracted from a given signal). Several discriminant functions or decision rules that hold their origin in Bayesian decision theory include the Euclidean norm (minimum distance classifier), the Mahalanobis distance, classifiers based on Parzen-window estimation, and nearest-neighbor classifiers.[8] In Section 4.4.3.1 and Section 4.4.3.2 of this chapter, Bayesian decision schemes and Fisher linear discriminants and multiple discriminant analysis are generalized. The Mahalanobis distance (MD) is implemented and evaluated in conjunction with different feature extraction and selection approaches in Section 4.4.5.

4.4.3.1 Bayesian Decision Theory

The most basic and perhaps the most frequently used set of discriminant functions is derived from Bayesian decision theory. The Bayes formula can be written as

$$P(\omega_i \mid x) = \frac{p(x \mid \omega_i)P(\omega_i)}{p(x)}, \tag{16}$$

where $P(\omega_i)$ is the prior probability of the structural state ω_i, x is the feature vector, $p(x)$ can simply be viewed as a scale factor assuring that the posterior probabilities, $P(\omega_i \mid x)$, sum to one. $p(x \mid \omega_i)$ is the conditional probability density function for x given that the structural state is ω_i. Thus for a classification problem of k structural states, Equation (16) yields k discriminant functions. The decision rule then becomes: "Choose ω_i, if $P(\omega_i \mid x) > P(\omega_j \mid x)$ for all $i \neq j$ and $i, j = 1 \ldots k$." It can be shown that Bayes decision rule minimizes the probability of error (i.e. the probability of misclassification) in the classification process.[8]

Obviously one difficulty in using the Bayes formula is the determination of the prior probabilities as well as the conditional densities. The quantity $p(x)$ is of little importance and may be ignored since it is only a scale factor. For the example application at hand, in order to calculate the state-conditional probability density functions, $p(x \mid \omega_i)$, the multivariate PDF of the *m*-dimensional feature vector x must be known for each structural state. Assuming that the feature vector $x \sim N(\mu_x, \Sigma_x)$, the conditional densities can be evaluated using estimates of μ_x and Σ_x, which can be obtained from the training data set. Taking advantage of this information allows for several simplifications of Equation (16) and the derivation of the following set of discriminant functions:

$$g_i(x) = -\frac{1}{2}(x - \mu_i)^t \Sigma_i^{-1}(x - \mu_i) - \frac{1}{m}\ln|\Sigma_i| + \ln P(\omega_i) \tag{17}$$

where the Bayesian decision rule is defined as: If $g_i(x) > g_j(x)$ for all $i \neq j$, then x is classified into state ω_i with minimum probability of error.[8]

In Equation (17), the prior probabilities, $P(\omega_i)$, can be difficult to determine. It is reasonable to assume initially, in the absence of any observations, that each structural state has an equal likelihood of occurring. In practice one might adjust the prior probabilities based on observed experience. However, assuming equal prior probabilities eliminates the bias that would be caused by allowing one structural state to be more likely to occur than another. For example, it may seem to be reasonable to set $P(\omega_{HEALTHY})$ greater than $P(\omega_{DAMAGED})$, since the probability of structural damage occurrence should certainly be low for any structure. Allowing this, however, would cause the Bayesian decision rule to be biased towards classifying the structure as healthy and much more reluctant to identify it as damaged even when it is indeed damaged. Therefore it can and should be assumed that each structural state has an equal likelihood of occurring. This assumption further simplifies Equation (17) as

$$g_i(x) = -\frac{1}{2}(x-\mu_i)^t \Sigma_i^{-1}(x-\mu_i) - \frac{1}{m}\ln|\Sigma_i| \qquad (18)$$

where $(x-\mu_i)^t \Sigma_i^{-1}(x-\mu_i)$ is known as the Mahalanobis distance and each parameter can be estimated from the training data sets. This shall be the basic form of all discriminant functions (i.e. classifiers) used in the following investigations. Several additional assumptions may further reduce Equation (18). However, generally speaking this is the classifier proven (mathematically) to work best (optimally) and will therefore be the foundation of all other applied/derived classifiers in this study.

4.4.3.2 Fisher Linear Discriminant

The Fisher linear discriminant is based on discriminant analysis. Whereas principle component analysis (PCA) finds directions that are ideal for representation, a discriminant analysis attempts to isolate those directions that are efficient for discrimination. For a problem with k structural states, it has been shown[8] that a transformation matrix, W, that maximizes the ratio of between-class scatter, S_B, and within-class scatter, S_W, projects m-dimensional observations into a $(k-1)$-dimensional subspace and simultaneously constructs $(k-1)$ discriminant functions that allow state classification. Scatter matrices are defined as:

$$S_W = \sum_{i=1}^{k} S_{\omega_i}, \text{ where } S_{\omega_i} = \sum_{all\ x \in \omega_i} (x - m_{\omega_i})(x - m_{\omega_i})^t \tag{19}$$

$$S_B = \sum_{i=1}^{k} (m_{\omega_i} - m)(m_{\omega_i} - m)^t \tag{20}$$

where m_{ω_i} is the within-class mean of class ω_i, m is the total mean of all observations, and x is the m-dimensional feature vector corresponding to a given observation. The columns of an optimal W are the eigenvectors that correspond to the largest eigenvalues of $S_W^{-1} S_B$. It should be noted that in general the solution for W is not unique. The W-induced transformation allows for rotation and scaling of the axes in various ways. These are all linear transformations from a $(k-1)$-dimensional space to a $(k-1)$-dimensional space and do not change the fact that W maximizes the ratio between S_B and S_W. It should also be pointed out that the Fisher discriminant only yields a straightforward decision rule for a two-class problem. For a problem with k states, the Fisher linear discriminant yields $(k-1)$ discriminant functions for which it remains to find $(k-1)$ thresholds, that is, points in the resulting $(k-1)$-dimensional subspace separating the projected classes. Searching for these thresholds may prove to be more difficult

than simply using the $(k-1)$ values as features with Bayes classifiers. Regardless, if anything, the Fisher linear discriminant analysis provides another way of reducing the dimensionality of the problem.[8]

4.4.4 Additional Signal Processing

There are several signal processing methods that can be used to normalize, clean (noise reduction), or otherwise transform (simplify) temporal data prior to application of feature extraction and selection methods. With regards to temporal data, there are three fundamental types of signal processing schemes: (1) time history analysis, (2) frequency spectrum analysis, and (3) time-frequency distribution analysis. Time history methods do not require a signal transformation and are therefore good for minimizing digital signal processing errors introduced by such procedures as the DTFT. On the other hand, raw temporal data is usually only conducive for structural state identification when the signal contains relatively few principal components. Otherwise frequency and time-frequency schemes are more appropriate. Linear signal averaging, RMS signal averaging, average time, temporal variance, auto- and cross-correlation, analytic signal, Hilbert transforms, and Poincare sections are all time history signal processing schemes.[3] Discrete Fourier Transforms, auto- and cross- power spectra, and bispectrum are frequency domain analysis methods.[3] Wavelet decomposition and wavelet mapping are two examples of time-frequency distributions,[3] which allow a time dependent frequency analysis to be made. Issues that must be considered when trying to perform any of these signal analysis methods deal with analog to digital signal conversion and discretization in time and frequency. Other fundamental limitations in signal processing are that data is acquired at a finite sampling rate as well as for a finite period of time. Frequency aliasing due to improper

sampling and data leakage due to signal truncation may result. Signal processing techniques such as utilizing the Nyquist sampling rate and windowing may partially solve these problems.

The above review indicates significant overlap between signal processing, feature extraction, feature selection, and state classification methods. These techniques ultimately are used to extract key pieces of information (features) from recorded data, which, in combination with one or more discriminant functions, are used to classify a sampled signal into one of two or more states.[8] There are no clear rules on what kind of features and classifiers are to be derived and combined for different problems and applications; only general guidance with some physical meaning and mathematical proof are available.[8,75,76,80] The following sections of this chapter will investigate in detail some of these general methods and modify them to produce unique feature extraction and selection methods. These methods are combined with one another to generate different damage detection algorithms, which are then evaluated on data obtained from the simplified test article via SFEM simulations described in previous chapters.

4.4.5 Evaluation of Damage Detection Methods

The probabilistic performance measures of Equations (9) though (12), which will used to evaluate different sensor arrays in Chapter 6, can also be used to evaluate a given combination of feature extraction, feature selection, and state classification methods and compare its performance to the performances of other combinations. Due to the nature of this problem, it has been observed that these performance measures are highly dependent on where the structural response is measured. Therefore, in order to identify the most robust combination of feature extractor and state classifier with respect to the location of the sensors, the sensor arrays of Figure 23 and Table 21 are considered and investigated.

In addition to sensor location, it should be noted that the performance measures are highly sensitive to the amount of uncertainty included in the model input parameters. Initial investigations considered a coefficient of variation (COV) of five percent, which yielded classification matrices that appeared to have been constructed at random, regardless of the which combination of feature extraction, feature selection, and state classification algorithms are implemented. On the other hand, a COV of one percent provides a nearly perfect classification matrix with non-zero values only along the diagonal for most of the combinations evaluated. In order to better differentiate between different combinations of feature extraction, selection, and state classification methods, a less than perfect confusion matrix is beneficial. Therefore a COV of two percent was used to perform the probabilistic finite element analyses and subsequent damage detection method evaluation. This produced classification matrices that distinguished very well between different damage detection methods, rendering some as good and others as ill-behaved at best. The results are explained in the following sections, where several combinations of feature extraction, feature selection, and state classification algorithms are implemented. The following combinations of feature extraction and selection methods and state classification algorithms were implemented and evaluated along the criteria defined in Equations (9) through (11). Table 22 summarizes the combinations detailed in Section 4.4.5.1 through Section 4.4.5.5 of this paper. The results are provided in Table 23 through Table 25.

4.4.5.1 DDM 1

Power spectral density (PSD) functions are estimated for each of the structural responses observed by the three piezoelectric sensors according to the modified Welch method as previously described with a bin size, n_b, of 30 data points and an overlap of 15 data points. This produced (3×16) measurements, yielding a 48-D feature vector whose dimension was reduced

to 10 via PCA. The Mahalanobis distance was used for classification. This combination is called DDM 1a.

An additional implementation (DDM 1b) using the PSD functions of the responses as observed by the three piezoelectric sensors was performed, where instead of reducing the dimensions of the 48-D feature vector using PCA, 10 optimal features were selected via the sequential forward selection (SFS) process, where the performance criterion is $P(\text{Correct Classification})$ as defined by Equation (11). This implementation is called DDM 1b.

A third implementation (DDM 1c) using PSD-based features is applied to the sample data, where the modified Welch method used to estimate the PSD functions does so with $n_b = 60$ data points and an overlap of 30 data points. This increases the feature vector's dimension from 48 to 93. The SFS process is used to reduce this feature space to 10-D. The Mahalanobis distance is used for state classification in DDM 1b and DDM 1c.

Utilizing sequential forward selection to identify the best 25 features from the feature pool of 93 features, produces combination DDM 1d, which also utilizes the Mahalanobis distance as the classifier. Three more variations, DDM 1e, DDM 1f, and DDM 1g, whose parameters are defined in Table 22, produce varying results shown in Table 23 through Table 25.

4.4.5.2 DDM 2

This damage detection method attempts to fully capitalize on the capabilities of PCA. A dimensionality reduction is performed on the response signal in the time domain reducing the nearly 1000-D observational space to a 10-D feature domain for each sensor independently, resulting in a total of 30 features, which are used directly with the Mahalanobis distance for classification. This combination is called DDM 2a.

Table 22. Summary of DDM definitions and combinations.

Name of Combination DDM__	Feature Extraction	Feature Selection	Features	PSD Parameters		PR Model	Number of Features Used in Classification
				n_b	Overlap	N_{order}	
1a	Power Spectral Density (PSD)	PCA	As Is	30	15	n/a	10
1b		SFS					10
1c				60	30		10
1d							25
1e				100	50		25
1f							30
1g				150	75		25
2a	Principal Component Analysis (PCA)	None		n/a			30
2b		SFS					10
2c							25
2d							30
2e							25
3a	Auto- and Cross-Correlation	None	2nd-5th CM				24
3b		SFS					10
3c		PCA					10
4a	Modified Coherence Functions (MCF)	None	Coefficients of PR Model	256	0	4	15
4b						7	24
4c						10	33
4d			2nd-5th CM			n/a	12
4e		PCA	As Is				30
4f		PCA & SFS					10
5a	Transfer Function	None	2nd-5th CM	n/a			12
5b			Coefficients of PR Model			10	33
5c						5	18
5d		SFS				10	10
5e		None	2nd-5th CM			n/a	12

A second implementation (DDM 2b) of this general methodology was employed where the nearly 1000-D observational space was projected to a 35-D feature space via PCA of each sensor's response. This yields a total of 105 features from which an optimal 10 were selected using the sequential forward selection process. This 10-D feature vector, in combination with the Mahalanobis distance yields the damage detection method DDM 2b. Utilizing sequential forward selection to identify the best 25 features from the feature pool of 105 features produced implementation DDM 2c. Two more variations, DDM 2d and DDM 2e, are produced by various

parameter changes as indicated in Table 22, yielding different performances as shown in Table 23 through Table 25.

Table 23. Probability of false alarm for various DDM for sensor layouts of Table 21.

Name of Combination DDM__	Sensor Layouts				
	SL1	SL2	SL3	SL4	SL5
1a	0.15	0.18	0.13	0.10	0.09
1b	0.13	0.11	0.07	0.09	0.10
1c	0.13	0.11	0.12	0.09	0.05
1d	0.12	0.09	0.12	0.10	0.14
1e	0.12	0.07	0.11	0.06	0.11
1f	0.13	0.08	0.10	0.09	0.12
1g	0.12	0.07	0.17	0.09	0.09
2a	0.19	0.14	0.21	0.18	0.16
2b	0.12	0.12	0.08	0.04	0.08
2c	0.12	0.09	0.16	0.05	0.14
2d	0.12	0.08	0.12	0.12	0.10
2e	0.11	0.11	0.11	0.08	0.08
3a	0.25	0.29	0.29	0.27	0.24
3b	0.17	0.15	0.10	0.10	0.16
3c	0.19	0.22	0.18	0.19	0.14
4a	0.57	0.45	0.47	0.70	0.55
4b	0.61	0.48	0.66	0.51	0.52
4c	0.41	0.30	0.61	0.50	0.59
4d	0.56	0.40	0.60	0.53	0.78
4e	0.92	0.72	0.76	0.95	0.92
4f	0.37	0.28	0.40	0.24	0.48
5a	0.75	0.52	0.68	0.62	0.67
5b	0.32	0.47	0.30	0.46	0.43
5c	0.47	0.51	0.55	0.65	0.50
5d	0.37	0.31	0.23	0.38	0.29
5e	0.65	0.37	0.69	0.62	0.62

4.4.5.3 DDM 3

This combination of damage detection algorithms utilizes an auto- and cross- correlation based feature extraction method. The auto- and cross- correlation functions of each sensor's recorded response are estimated. With three sensors, this approach generates a total of six functions (three auto- and three cross- correlation functions). The envelopes of these functions are estimated and

their second through fifth moments are approximated and used directly as features for state classification. A 24-D feature vector is employed in combination with the Mahalanobis distance for state identification purpose. This combination is called DDM 3a.

A second implementation of the auto- and cross- correlation based feature extraction method (DDM 3b) utilizes the SFS process to reduce the 24-D feature vector to 10-D. This optimal feature set, in combination with the Mahalanobis distance is used for state classification.

An additional implementation of this general methodology uses PCA instead of SFS to reduce the number of features from 24 to 10. Combining this 10-D feature vector with the Mahalanobis distance provides the combination called DDM 3c. No further variations of DDM 3a, DDM 3b, or DDM 3c were implemented due to their general initial poor performance.

4.4.5.4 DDM 4

Coherence function-based feature extraction is exploited in this DDM combination. The modified coherence function (MCF) as defined in Equation (14) is estimated for all combinations of two responses at a time. This yields three MCF with 128 measurements each (due to the utilization of the unmodified Welch method to estimate the auto- and cross- spectral densities with bin size of 256 data points and an overlap of zero), for which polynomial regression models of order N_{order} are constructed. The $3\times\left(N_{order}+1\right)$ coefficients of these models are used as features in conjunction with the Mahalanobis distance for state classification. This implementation is called DDM 4a. Variations DDM 4b and DDM 4c were performed, where the order N_{order} of the polynomial regression models assumes different values. The implementation specifications are detailed in Table 22. The results are shown in Table 23 through Table 25.

An additional implementation is performed (DDM 4d) that utilizes as features the second through fifth central moments of the MCF as estimated by Equation (14), where the PSD

functions are estimated with the unmodified Welch method. This approach yields a 12-D feature vector that is used with the Mahalanobis distance for state classifications. This combination is called DDM 4d.

Table 24. Probability of missed detection for various DDM for sensor layouts of Table 21.

Name of Combination DDM__	Sensor Layouts				
	SL1	SL2	SL3	SL4	SL5
1a	0.003	0.000	0.005	0.018	0.033
1b	0.023	0.005	0.013	0.023	0.013
1c	0.035	0.005	0.008	0.018	0.010
1d	0.008	0.003	0.005	0.010	0.005
1e	0.010	0.000	0.003	0.013	0.003
1f	0.005	0.003	0.000	0.005	0.003
1g	0.013	0.000	0.003	0.010	0.010
2a	0.003	0.000	0.000	0.005	0.000
2b	0.030	0.003	0.018	0.028	0.030
2c	0.008	0.000	0.000	0.005	0.000
2d	0.008	0.005	0.000	0.003	0.005
2e	0.010	0.003	0.003	0.005	0.008
3a	0.000	0.000	0.000	0.015	0.000
3b	0.015	0.000	0.015	0.030	0.005
3c	0.018	0.003	0.015	0.013	0.005
4a	0.095	0.180	0.248	0.058	0.133
4b	0.078	0.120	0.275	0.125	0.135
4c	0.243	0.450	0.170	0.225	0.220
4d	0.318	0.520	0.425	0.448	0.085
4e	0.000	0.015	0.010	0.000	0.003
4f	0.120	0.300	0.090	0.193	0.063
5a	0.197	0.423	0.256	0.358	0.303
5b	0.095	0.133	0.175	0.145	0.165
5c	0.080	0.160	0.053	0.088	0.153
5d	0.198	0.185	0.263	0.213	0.378
5e	0.265	0.553	0.256	0.360	0.332

A fourth approach using coherence function based features is implemented (DDM 4e), where PCA is employed to reduce the feature space dimension from $(3\times128)=384$ to 10. This reduced feature vector is used with the Mahalanobis distance for state identification. The implementation is called DDM 4e.

A fifth and final implementation of the coherence function based feature extraction method is carried out (DDM 4f), where PCA reduces the number of features from 384 to 105. In addition, SFS is applied to further reduce the feature space to a manageable 10 optimal features. The Mahalanobis distance is used as the classifier.

Table 25. Probability of correct classification for various DDM for sensor layouts of Table 21.

Name of Combination DDM__	Sensor Layouts				
	SL1	SL2	SL3	SL4	SL5
1a	0.696	0.650	0.610	0.666	0.654
1b	0.744	0.726	0.680	0.760	0.780
1c	0.748	0.746	0.704	0.742	0.810
1d	0.880	0.834	0.812	0.868	0.832
1e	0.904	0.862	0.826	0.884	0.858
1f	0.914	0.856	0.814	0.884	0.860
1g	0.888	0.868	0.836	0.884	0.860
2a	0.784	0.754	0.706	0.770	0.732
2b	0.818	0.782	0.794	0.804	0.848
2c	0.888	0.822	0.826	0.874	0.874
2d	0.916	0.860	0.866	0.894	0.872
2e	0.908	0.846	0.830	0.876	0.882
3a	0.680	0.618	0.580	0.716	0.584
3b	0.644	0.618	0.626	0.648	0.712
3c	0.594	0.542	0.582	0.576	0.606
4a	0.414	0.366	0.348	0.400	0.376
4b	0.386	0.374	0.254	0.460	0.374
4c	0.400	0.320	0.362	0.382	0.352
4d	0.344	0.267	0.254	0.257	0.292
4e	0.280	0.422	0.282	0.460	0.266
4f	0.484	0.452	0.440	0.460	0.428
5a	0.314	0.254	0.263	0.201	0.212
5b	0.574	0.402	0.508	0.424	0.462
5c	0.520	0.382	0.476	0.368	0.452
5d	0.542	0.442	0.530	0.394	0.430
5e	0.280	0.241	0.261	0.202	0.209

4.4.5.5 DDM 5

This combination is called DDM 5a and utilizes transfer function based features. Equation (15) is used to estimate the transfer functions for all combinations of two responses at a time. This

approach yields three transfer functions, whose second through fifth central moments are directly used as features in state classification. The resulting 12-D feature vector is used in combination with the Mahalanobis distance.

Two additional implementations (DDM 5b, DDM 5c), which utilize transfer functions, constructs polynomial regression models of order N_{order} about them. The $3\times\left(N_{order}+1\right)$ coefficients of these models are used as features in conjunction with the Mahalanobis distance for state classification. DDM 5b and DDM 5c are evaluated for $N_{order}=5$ and $N_{order}=10$, respectively, to yield the results shown in Table 23 through Table 25.

Another approach to implementing transfer function based features is defined as constructing polynomial regression models of order N_{order} about the transfer functions, and selecting an N_{opt} number of their coefficients to be utilized as features. The SFS process is used to reduce the $3\times\left(N_{order}+1\right)$ number of coefficients by selecting an optimal set of $N_{opt}=10$ features. The Mahalanobis distance is used for state classification. This implementation is called DDM 5d and $N_{order}=10$.

The last and final implementation (DDM 5e) is performed utilizing the second through fifth central moments of the envelopes of the transfer functions as features. This produces a 12-D feature vector which is used directly with the Mahalanobis distance for state classification. This combination is called DDM 5e. No further variations of this general DDM were evaluated due to their initial poor performance.

4.4.5.6 General Observations and Interpretations of Results

From Table 23 through Table 25, it is clearly evident that different combinations of feature extraction, feature selection, and state classification methods, yield significantly different results.

In addition, sensor layout plays an important role and this investigation reiterates the need for sensor placement optimization (SPO), which is addressed in Chapter 6.

With respect to the above implementations, the signal processing scheme that seems to provide the greatest improvement to any DDM regardless of how the features are initially extracted is the concept of identifying optimal features via feature selection. Sequential forward selection determines the optimal combination of N_{opt} features from a m-dimensional feature pool, where $N_{opt} << m$, such that some performance measure is maximized. In this investigation the chosen quality metric is $P(\text{Correct Classification})$ as defined by Equation (11). m is specified by the feature extraction method and may vary from as little as 10 to as much as 500 and more. This leaves N_{opt} to be specified by the user. The following investigation attempts to identify an optimal value of N_{opt}.

A feature pool of 28 independent and normally distributed features with N samples per structural state was randomly generated, where $N = 10, 20, 40, 70, 100, 150, 200, 300, 500, 1000$. The SFS process was used to select the N_{opt} optimal features which would maximize $P(\text{Correct Classification})$, where $N_{opt} = 1, 2, ..., 14$. The results are shown in Figure 24.

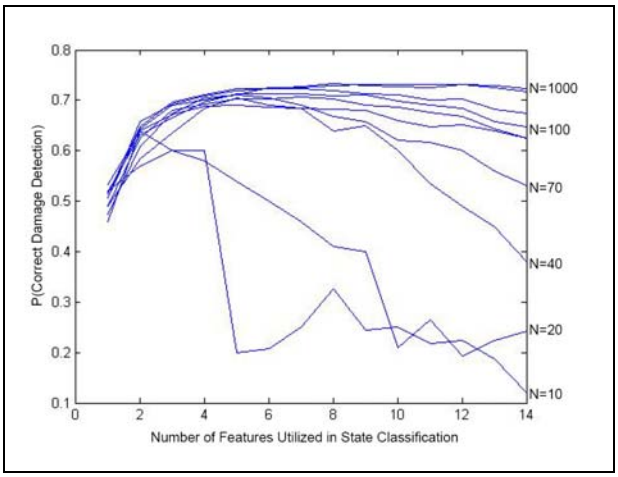

Figure 24. Optimal number of features to search for via SFS vs. DDM performance.

It is easily identified that the curse of dimensionality sets in rather quickly for problems with small sets of training data (i.e. when N is small). However, even when N is relatively large (greater than 100), there is an optimal number of features that maximizes $P(\text{Correct Classification})$. From the plot in Figure 24 it appears that this number is between 6 and 10. Even when the training data set is large (i.e. $N = 1000$), utilizing more than 10 features causes a reduction in $P(\text{Correct Classification})$. These observations instigated the investigation of an optimal number (or range) of features to be used with the test article and DDM described in the previous sections. For the problem at hand $N = 100$. Figure 25 shows the result obtained for DDM 2b and is a good example of the general trend observed with other DDM. Therefore, whenever the sequential forward selection process is utilized to identify an optimal subset of features, $N_{opt} = 25$ should be used, unless the initial feature pool is of dimension less than 25. This observation is also seen in Table 25 for combinations DDM 1e, DDM 1f, DDM 1g, and DDM 2c, DDM 2d, DDM 2e, which perform significantly better than other similar combinations with fewer numbers of optimal features utilized. It should be noted here that the reason for observing this trend only in Table 25 is due to $P(\text{Correct Classification})$

being the performance measure employed during the SFS process. It would be wise to utilize a multi-objective measure to include all probabilistic performance measures within SFS.

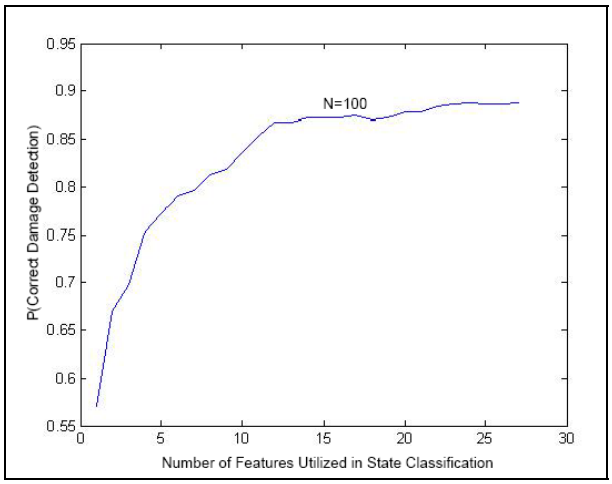

Figure 25. N_{opt} vs. P(Correct Classification) for DDM 3a.

An additional investigation that was conducted while implementing the different combinations of DDM considers the role and importance of N_{order}, the order of the polynomial regression models, whose $(N_{order}+1)$ coefficients were used as features. Similar to the SFS process analysis, a feature pool of 28 independent and normally distributed features was randomly generated with 100 samples per structural state. Polynomial regression models of order 1 through 10 were constructed and their coefficients used in classification via the Mahalanobis distance. The results are shown in Figure 26.

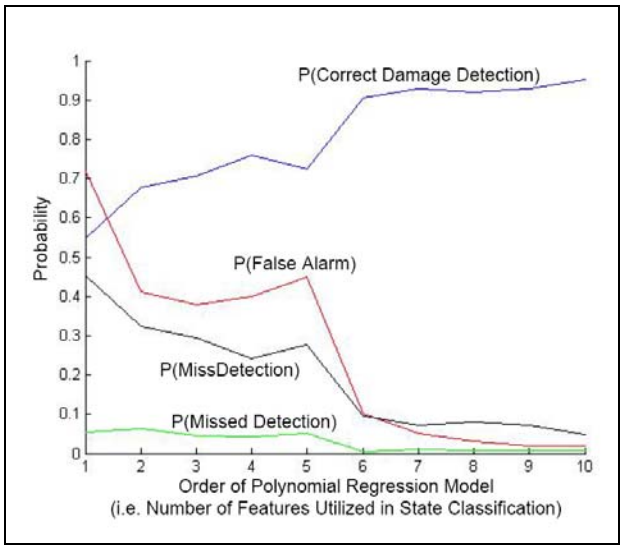

Figure 26. Order of regression model vs. performance criteria.

From Figure 26 it is evident that regression models of orders six to 10 adequately capture the set of useful features and allow for appropriate state classification. It should also be noted that using a regression model with less than seven coefficients (i.e. $N_{order} < 6$) does not provide sufficient detail about the feature space.

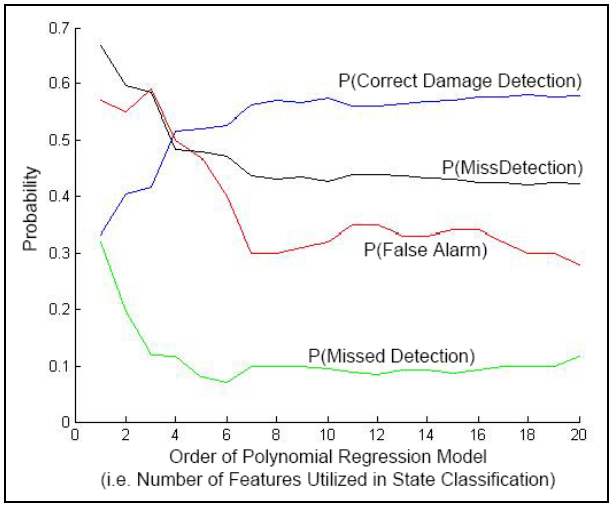

Figure 27. N_{order} vs. performance metrics for DDM 5b.

A similar investigation was performed on data obtained from the test article and the DDM described above. The results for DDM 5b are shown in Figure 27 and reflect the observations made for the analysis of the randomly generated features as well as the general trends observed for other DDM. Therefore implementations which utilize coefficients of a regression model should be performed with a polynomial regression model of order six or higher.

Table 23 through Table 25 demonstrate that more complex signal analysis and processing tools do not always yield more efficient or "better" results. It is easily seen that simple PSD-based features, which are easily extracted, are much more effective than their more complex counterparts such as coherence function and transfer function based features. In addition, as stated above, the single most important component of the implemented DDM appears to be feature selection via the SFS process. Switching from PCA to SFS in the implementation of PSD-based features, caused an average increase of 12.7% in $P(\text{Correct Classification})$. In addition, making the switch from PCA to SFS and increasing the feature pool from which to select the optimal feature set to be used for classification, caused an average increase of 14.6%. Similarly, a 39.4% increase in $P(\text{Correct Classification})$ was obtained when SFS was added to the DDM utilizing coherence function based features (i.e. DDM 4e vs. DDM 4f). Similar trends of improvement are observed for other performance criteria when SFS is utilized.

Two methods that generally do not work well for this particular problem are those implementations that utilize coherence function and transfer function based features. Generally speaking, these DDM (DDM 4a through DDM 4f, and DDM 5a through DDM 5e) do not identify the test article's state well. Even when combining these methods with PCA or SFS, do they not correctly classify the structure more than 50% of the time. $P(\text{False Alarm})$ and other

performance measures provide convincing proof that these approaches are ill behaved for this particular test application.

In general, it was observed that PSD-based features in combination with PCA or the SFS process yield the best results with respect to several performance measures. In addition it was shown that transfer function based features and coherence function based features generally performed poorly for the given example problem. Overall, feature selection methods provide the greatest increase in performance and are a worthy computational expense, regardless of the type of features utilized.

4.5 Applied Damage Detection Methodology

The SHM methodology utilized in this study employs an active vibration sensing scheme which includes the excitation of the structure via a chirp input signal and the examination of the structure's response via pattern recognition and state classification methods. This methodology compares a feature vector, extracted from the response signals of a structure in a given state, to several base line feature vectors and classifies the examined structure into the class whose base line feature vector most closely resembles the examined structure's feature vector. Classification can be done using several different discriminant functions.

From the estimated von Mises stress records of the SFEM analyses at sensor locations S2, S3, and S4 (Figure 1b and Equation (3)), a set of features is extracted. Features are characteristics unique to a signal generated under a given set of parameters. The set of features utilized for this example problem is based in the frequency-domain and is extracted via the well-known Welch method[81,86,87,88] from the power spectral densities (PSD) of the signals. With a bin size of $n_b = 100$ measurements and an overlap of 50%, the Welch method produces 51 features each

from the signals obtained at piezoelectric sensor locations S2, S3, and S4 by dividing each signal into bins of specified size, n_b, windowing each bin with a Hamming window of the same length, estimating the PSD utilizing the FFT technique with a specified length of N for each bin, and averaging the periodograms over all bins. In this study N is equal to the bin size, n_b. This generates a 153-dimensional feature vector.

Dimensionality reduction is achieved via feature selection. Feature selection provides a subset of N_{opt} features from the *m*-dimensional feature pool most effective for state classification. In general, the fewer features used in a classifier, the more likely the training set performance will be representative of test set performance.[9] A sequential forward search algorithm[84,85] is used to identify 25 optimal features from the original 153-dimensional feature pool.

The above defined feature vector is then used for state classification. The state classifier utilized in this study is derived from Bayes decision theory and minimizes the probability of classification error.[8] The discriminant functions, one for each structural state ("healthy", "damaged at bolt 1", "damaged at bolt 2", etc.), are the Mahalanobis distances as given in Equation (21).

$$d_j(x) = (x - \mu_j)^t \Sigma_j^{-1} (x - \mu_j) \tag{21}$$

where *j* indexes the structural state, *x* is a feature vector to be classified, and μ_j and Σ_j are the mean feature vector and covariance matrix of the learning data set of structural state *j*. The training data set consists of the first 50 simulations of each structural state as obtained via the stochastic FEM procedure in Chapter 2. Since the Mahalanobis distance requires the determination of the inverse of Σ_j it is necessary that the feature covariance matrix be non-singular. State classification is continued by evaluating each discriminant function for each

simulation of the testing data set, consisting of the second 50 simulations of each structural state, and assigning the state according to the discriminant function with the smallest value. This procedure yields a classification matrix as shown in Table 20, from which probabilistic performance measures may be estimated.

Applying this damage detection method to the five randomly selected sensor configurations of Table 21 and Figure 23 yields the performance measures shown in Table 26. Note that for the five sensor layouts presented, the "best" sensor configuration varies depending on which performance measure is utilized for evaluation. A multi-objective evaluation measure of the form shown in Equation (22) may be more appropriate.

$$f(x) = \alpha \cdot P(CC) + \beta \cdot P(TypeI) + \gamma \cdot P(TypeII) \tag{22}$$

This however generates the additional problem of assigning values to constants α, β, and γ, which may prove to be difficult and depending on what values are chosen may cause the optimal solution to vary significantly. Regardless, Table 26 reiterates the necessity of sensor placement optimization (SPO), which is addressed further in Chapter 6.

Table 26. Performance measures corresponding to randomly selected sensor layouts of Table 21.

Sensor Layout	P(CD)	P(Type I)	P(Type II)
SL1	0.916	0.12	0.0075
SL2	0.860	0.08	0.0050
SL3	0.866	0.12	0
SL4	0.894	0.11	0.0025
SL5	0.872	0.10	0.0075

Guratzsch and Mahadevan[89] have shown that the above damage detection algorithm works most efficiently in comparison with damage detection algorithms which utilize other feature types, feature extraction methods, dimensionality reduction schemes, and feature selection algorithms.

Therefore, this method as defined here is used for the remainder of this study – namely for sensor placement optimization (SPO), which was shown to be a necessity. However, prior to optimizing the performance measures defined in Section 4.3 with respect to the location of sensor S2, S3, and S4, a validation assessment of the damage detection method, or sensor layout performance prediction methodology, must be undertaken. Chapter 5 utilizes the validation metrics defined in Section 3.2, to assess the accuracy and usefulness of the sensor layout performance prediction methodology identified here. Chapter 6 proceeds with sensor placement optimization.

CHAPTER V

VALIDATION ASSESSMENT OF SENSOR LAYOUT PERFORMANCE PREDICTION

This chapter is related to research Objective 2 and assesses the accuracy of the damage detection. The sensor layout performance predictions computed via the damage detection method of Section 4.5 are compared with performance measures obtained directly from experimental observations. Section 5.1 provides an introduction, while Section 5.2 details the experimental procedure used to obtain laboratory observations for the validation assessment of Section 5.3.

5.1 Introduction

Similar to assessing the credibility of the SFEM, the prediction model for estimating the sensor layout performance measures requires validation assessment. In fact, the general SPO methodology consists of three hierarchical components that require validation: 1) stochastic finite element model for dynamic structural analysis, 2) damage detection and sensor layout performance prediction, and 3) optimum sensor configuration design. Figure 28 shows the hierarchical propagation of error through the general SPO methodology, where the uncertain inputs to each component, in addition to the modeling error associated with each component's process, compound and produce uncertain outputs with increasing error and variability. The validation of each component's output prior to initiating subsequent components is critical in regard to maintaining control with respect to error and uncertainty of the overall SPO methodology output.

Validation assessment of the first component (SFEM models) was reported in Chapter 3. The second stage of the SPO under uncertainty methodology (i.e. the sensor layout performance prediction method) as defined in Chapter 4, is being assessed in this chapter. In order to assess the validity of the performance prediction method, several sensor layouts are tested experimentally. Damage detection and sensor layout performance measures, as predicted by the analytical methodology and as observed in the laboratory are compared in order to validate the performance measure prediction method. Several validation metrics – the modal assurance criterion (MAC), classical and Bayesian hypothesis tests, and the model reliability metric (MRM) – are again investigated. Results are presented in Section 5.3.

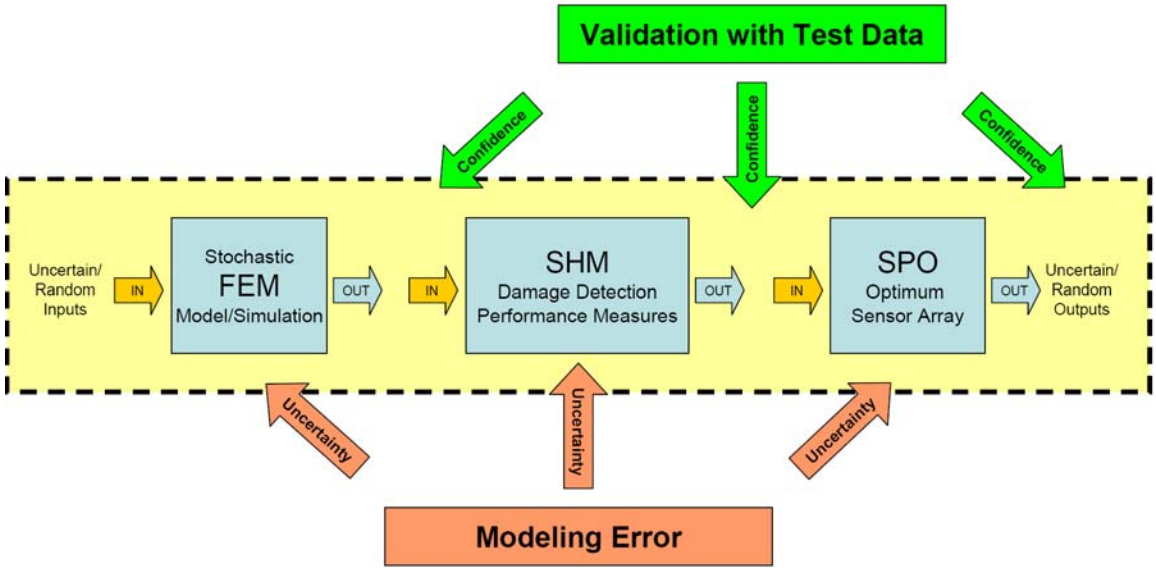

Figure 28. Propagation of error and uncertainty through general SPO methodology.

During implementation of the sensor layout performance prediction methodology, information is lost at various points (e.g. where discrete signals receive a reduction in dimensionality), while modeling and processing errors enter the procedure (e.g. where continuous transformations are applied to discrete signals). Figure 29 graphically shows each step of the prediction

methodology and isolates critical locations, where care must be taken to maintain control of the process.

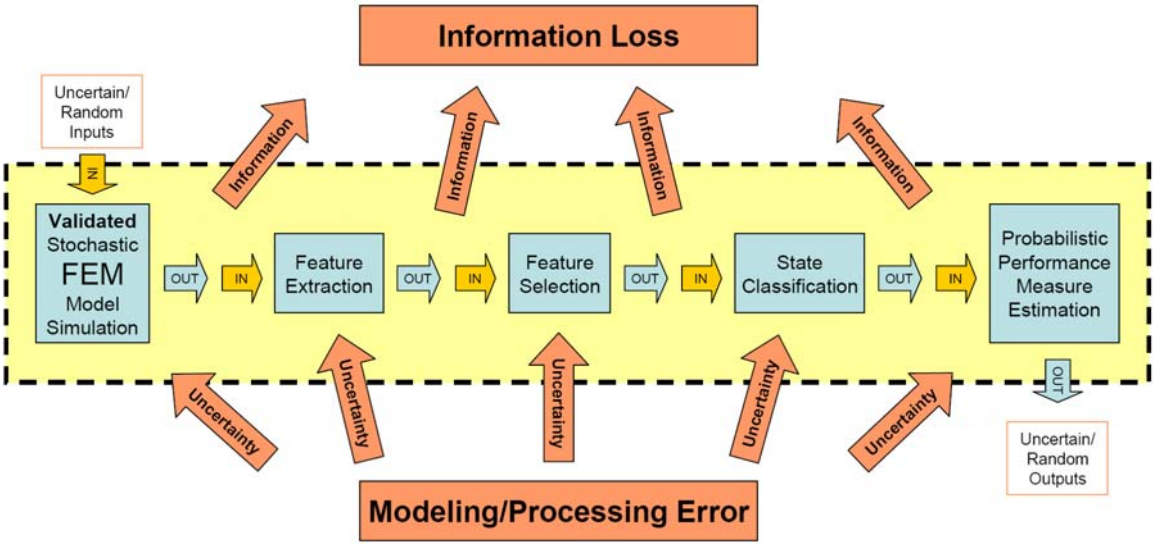

Figure 29. Sensor layout performance prediction methodology.

Although the stochastic finite element model was validated (Chapter 3), the validation was performed on the natural modes of vibration, while the model is subsequently used for the prediction of the structure's response to a sine sweep excitation. Also, the SFEM output (i.e. the structural response realization) is in the form of a time-series displacement of the FEM nodes of the model in three axial directions. An equivalent von Mises stress is estimated and utilized with the damage detection algorithm (Equation (3)). In addition, MSP is used for transient analysis of the SFEM. Modeling and processing errors are associated with this utilization of the validated stochastic FEM model.

Feature extraction and feature selection provide two levels of data reduction and transformation. Feature extraction, by definition, assesses the most descriptive characteristics of a signal and discards the remainder, causing information loss. In addition, the signal processing that takes

place to transform a finite, discrete, signal from the time domain into the frequency domain adds processing error and uncertainty. Similarly, feature selection identifies the *n* most useful features for classification and discards the remaining information. Subjectivity (and therefore uncertainty) is associated with choosing *n*. While state classification via Bayesian decision theory minimizes the probability of classification error, an inherent amount of error remains. Uncertainty is associated with choosing the training data set of appropriate size. Finally, probabilistic sensor layout performance measures are based on a discrete and finite number of samples within the classification matrix. As will be pointed out in Section 5.3.2, the performance measures can only take on a finite number of discrete values, which certainly introduces error into the performance measure prediction. The above identified locations of information loss and error introduction are shown graphically in Figure 29 and are by no means absolute and complete; other modeling and processing errors may exist and information may be generalized/discarded/lost at any step of the probabilistic sensor layout performance measure prediction methodology, and such errors should be accounted for in the analysis.

5.2 Experimental Observations

An important step is the validation of the sensor layout performance prediction method with experimental data. This section provides a description of the laboratory setup and the procedures followed during laboratory testing. Figure 30 shows the experimental SHM and data acquisition system as it is applied to the TPS test article described in Section 1.4 (Figure 1).

The sensor layout performance prediction process of Chapter 4 was carried out for the seven sensor configurations listed in Table 27. The coordinates are with respect to the bolt-4-corner of

the test article (i.e. bottom left corner of test article shown in Figure 1b) and the corresponding predicted sensor layout performances are shown in Table 27.

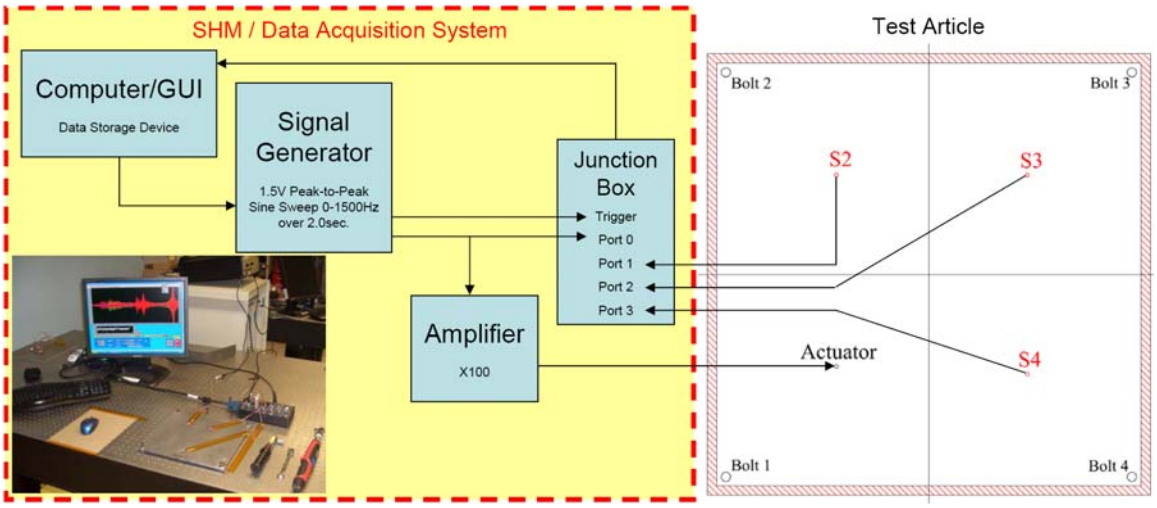

Figure 30. Experimental SHM and data acquisition systems as applied to test article.

Table 27. Results: predicted performance measures corresponding to seven different sensor layouts.

Sensor Array	Coordinates of Sensor			Analytically Predicted		
	S2	S3	S4	P(CC)	P(FA)	P(MD)
1	8.5, 8.5	8.5, 3.5	3.5, 3.5	0.898	0.13	0.0050
2	8.75, 6.75	6.0, 3.5	3.5, 0.75	0.944	0.13	0.0075
3	7.0, 8.5	11.73, 0.27	5.75, 1.25	0.916	0.01	0.0000
4	6.75, 8.75	9.25, 2.25	5.0, 5.0	0.896	0.10	0.0075
5	11.0, 11.0	11.0, 1.0	1.0, 1.0	0.874	0.08	0.0000
6	11.0, 7.0	6.5, 5.0	1.0, 5.0	0.898	0.08	0.0050
7	7.0, 11.0	7.5, 1.0	1.75, 1.0	0.878	0.08	0.0025

The SHM actuation signals (i.e. sine sweep from 0 to 1,500Hz) are generated and recorded using a Labview version 6.1 software GUI and a National Instruments PXI 6052E data acquisition card. A Fluke PM5193 Programmable Synthesizer/Function Generator produces a 1.5V, peak-to-peak, swept frequency sinusoid, 0 to 1500Hz in approximately 2.0 seconds as the broadband excitation signal. The excitation function is amplified with a Krohn-Hite 7500 amplifier by a factor of 100 and applied to the test article via a 0.25 inches in diameter piezoelectric disk

transducer (i.e. a surface-bonded piezoelectric actuator as discussed in Section 4.1) at sensor location S1 (labeled "Actuator" in Figure 30). Structural responses are collected via piezoelectric sensors S2, S3, and S4 at a frequency of 10kHz and a 16-bit analog to digital conversion.

Experimental structural response data from healthy and damaged states are collected in rounds. Each round of SHM testing and data collection consists of the following steps. Prior to each round, all bolts are loosened entirely to simulate a detached TPS panel.

- Bolt *j* is tightened to 25% nominal torque to simulate damage state *j*, while all other bolts are tightened to 100% nominal torque.
- Four stimuli in the form of the above defined sinusoid are applied via the actuator.
- Four corresponding responses are collected via piezoelectric sensors S2, S3, and S4 and recorded in the data storage device.
- Bolt *j* is tightened to 100% nominal torque to simulate the healthy condition.
- Four sine sweeps are applied via the actuator.
- Four corresponding responses are collected and recorded.

These steps are repeated for $j = 1 \ldots 4$, making up one round of data collection. A total of 50 rounds of experimental test data were collected per sensor array. The SHM damage detection algorithm as defined in Section 4.5 is applied to each sensor array's data set. Classifiers are trained on the first 25 rounds, and tested on the remaining 25 rounds of each data set. Training and testing data sets are reversed to achieve higher fidelity within the classification matrix. It should be noted that the data recorded during experimental testing consists of time-series voltage signals captured by sensors S2, S3, and S4. The signal applied via the actuator is also recorded and may be utilized for normalization purposes; however, this is not required for the damage

detection method applied in this study, which is directly implemented on the voltage signals (i.e. the voltage time-series measurements are not transformed into equivalent von Mises stress measurement). Discrepancies between performance predictions and observations are certainly introduced; however, it is assumed (blindly) that these discrepancies are negligible.

The experimentally observed performance measures corresponding to the seven sensor configurations of Table 27 are shown in Table 28. Note, that neither Table 27 nor Table 28 presents any expected values or variances of these variables, but simply shows the performance measures as obtained by applying the SHM damage detection procedure outlined in Chapter 4.

Table 28. Performance measures corresponding to sensor arrays of Table 27.

Plate	Observed Laboratory Test Performance Measures		
	P(CC)	P(FA)	P(MD)
1	0.9688	0.0200	0.0238
2	0.9231	0.1163	0.0013
3	0.9912	0.0000	0.0037
4	0.9181	0.0100	0.0625
5	0.9950	0.0000	0.0063
6	0.9087	0.0125	0.1250
7	0.9500	0.0100	0.0775

5.3 Methodology Validation

This section considers the application of the model validation metrics defined in Section 3.2 to evaluate and assess the usefulness of the sensor layout performance measure prediction methodology. The modal assurance criterion (MAC), the model reliability metric (MRM), classical and Bayesian hypothesis tests, and multivariate validation are investigated.

5.3.1 Comparison and Correlation

This section considers validation of the prediction methodology via the metrics discussed in Section 3.2.1 and Section 3.4.1. The performance measures are sorted in order of $P(CC)$, $P(FA)$, and $P(MD)$, to examine the correlation between prediction and observation. This is first investigated by plotting the experimentally observed performance measures against the predicted ones. Trend line coefficients, R^2-values, and correlation coefficients are provided in Table 29.

Table 29. Trend lines and coefficient of determination.

Sensor Array	Trend Lines			Correlation Coefficient
	Slope	Intercept	R^2	
1	1.1206	-0.0483	0.9824	0.9912
2	0.9868	-0.0088	1.0000	1.0000
3	1.0859	-0.0035	0.9998	0.9999
4	1.0325	-0.0152	0.9787	0.9893
5	1.1752	-0.0415	0.9922	0.9961
6	0.9676	0.0317	0.9639	0.9818
7	1.0706	0.0031	0.9793	0.9896

The data in Table 29 shows that the analytical predictions for the performance measures of the sensor arrays are highly correlated with their experimental counterparts. Additionally, MAC, as described in Section 3.2.1, is applied. Given a set of seven experimentally observed sensor array performance measures and a set of seven analytically predicted performance measures, the seven MAC values of Table 30 can be calculated.

Table 30. MAC values for seven sets of performance measures.

Plate Number						
1	2	3	4	5	6	7
0.9846	0.9998	0.9999	0.9865	0.9917	0.9841	0.9894

Generally speaking, a value in excess of 0.9 implies well correlated modes.[48] Table 30 shows that all sets are very well correlated, with MAC values greater than 0.98. Note that even though MAC has traditionally been applied to structural modal analysis model validation, it can be used to compare any two vectors with respect to correlation assessment. Since correlation can be viewed as a measure of the angle between two vectors, another logical extension to comparing two vectors is the investigation of the distance between them. The geometric distance given by $\left(\{\Psi_X\}-\{\Psi_A\}\right)^T \cdot \left(\{\Psi_X\}-\{\Psi_A\}\right)$ is a good measure of how close two vectors are to one another when only one measurement of each vector exists. Otherwise the Mahalanobis distance, $\left(\{\Psi_X\}-\{\Psi_A\}\right)^T \Sigma^{-1}\left(\{\Psi_X\}-\{\Psi_A\}\right)$, where Σ is the covariance matrix of either multiple analytical predictions or experimental observations, can be utilized. It should be noted that the distance between two vectors alone does not provide an assessment of how well predictions correspond to observations; a measure of the angle between the two vectors must also be considered (i.e. correlation coefficients - Table 29; MAC values - Table 30; etc.). Table 31 provides the geometric distance between the predicted sensor layout performance measurements of Table 27 and the experimentally observed ones of Table 28. As can be seen in Table 31, the distances, though small, are significant considering that the magnitude of the elements of each vector are limited to the range [0, 1].

Table 31. Geometric distance between seven performance measure vectors.

Plate Number						
1	2	3	4	5	6	7
0.132	0.026	0.076	0.108	0.141	0.138	0.125

The correlation analysis shows that the sensor layout performance prediction is well correlated with the observed performance. However, the geometric distances between the prediction and

observation vectors, indicate that differences may exist, which is indeed the case as will be shown in the following sections of this chapter.

5.3.2 Model Reliability Metric

The model reliability metric (MRM) cannot be applied directly to the data of Table 27 and Table 28, since only one measurement exists for all analytically predicted and experimentally observed performance measures. Multiple measurements of the performance measures must first be obtained. A random partitioning scheme of the analytically predicted data into training and testing sets may be applied to gather the stochastic properties of the performance measures with respect to the SHM damage detection process. Previously, partitioning was performed via an ordered 50-50 split. During random partitioning the data is grouped into equal size training and testing sets by random permutation of the data set, followed by a 50-50 split. Applying this process 100 times yields 100 unique sets of performance measure estimates for each given sensor array. The results of this random partitioning scheme as applied to the analytical predictions are summarized in Table 32.

Table 32. Results of random partitioning of analytically predicted data set.

	P(CC)		P(FA)		P(MD)	
Plate	Mean	StDev	Mean	StDev	Mean	StDev
1	0.892	0.013	0.1144	0.021	0.004	0.0025
2	0.942	0.0097	0.0887	0.0227	0.0041	0.0025
3	0.9126	0.013	0.0459	0.02	0.0035	0.0029
4	0.8904	0.0125	0.1018	0.0246	0.0039	0.0031
5	0.8455	0.017	0.1244	0.0264	0.0024	0.0029
6	0.8952	0.0151	0.0806	0.023	0.0072	0.0042
7	0.8741	0.0175	0.0895	0.0243	0.0015	0.0021

MRM is then applied directly as defined in Equation (5), where Θ is a single experimental observation given in Table 28, while $\bar{x}$ and s are the observed sample mean and sample standard deviation of the performance measure prediction, respectively, shown in Table 32. $n = 100$. Figure 31, Figure 32, and Figure 33 show the results graphically as a function of ε, which can be interpreted as an allowable difference between performance prediction and observation.

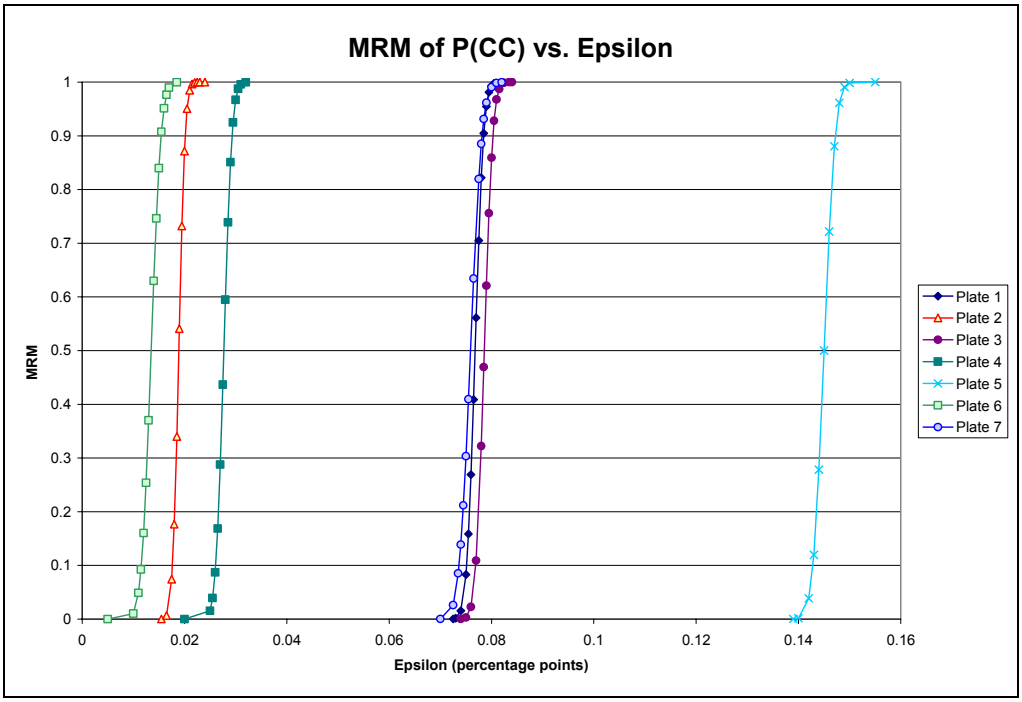

Figure 31. MRM vs. ε for P(CC) performance measure.

Figure 31 shows that for all seven sensor arrays, the experimentally observed $P(CC)$ is within 15 percentage points of the prediction with 100% probability (i.e. $r = 1.000$). Figure 31 also shows that sensor configuration 5 is likely an outlier. In fact, all sensor layouts, except sensor array 5, produce MRM scores greater than 90% (i.e. $r = 0.900$) for $\varepsilon = 0.08$. These results show that MRM is a stricter and more discriminating measure for validation and better identifies

discrepancies between performance prediction and observation than the comparisons made in Section 5.3.1. Where MAC concluded that performance measure predictions are approximately equally highly correlated to the experimentally observed ones for all sensor arrays, MRM clearly shows significant differences between analytical prediction and experimental observation. MRM, as defined by Equation (5), considers each performance measure individually; therefore differences that are not observable with MAC and trend line comparisons (slopes, y-intercepts, and R^2-values), which consider the three performance measures simultaneously, can be detected with MRM.

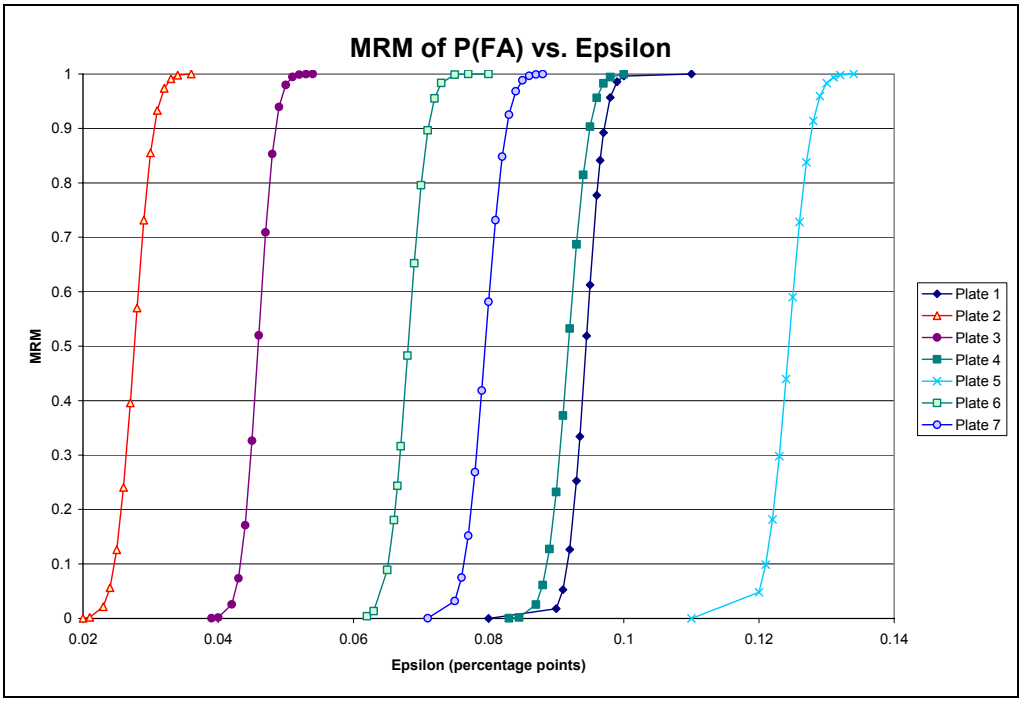

Figure 32. MRM vs. ε for P(FA) performance measure.

Figure 32 shows that the experimentally observed $P(FA)$ is within 13.5 percentage points of the prediction with 100% probability for all sensor arrays. Figure 32 also shows that sensor configuration 5 is likely an outlier.

Similarly, Figure 33 demonstrates that for all sensor layouts, the experimentally observed $P(MD)$ is within 12 percentage points of the corresponding predicted sensor layout performance with 100% probability. All sensor layouts, except arrays 4, 6, and 7 produce MRM values greater than 90% (i.e. $r = 0.900$) for $\varepsilon = 0.0202$, which corresponds to 2.02 percentage points of the performance measures. Test plate 5 does not appear to be outlier for this particular performance measure. Generally, the results shown in Figure 33 demonstrate good correlation; however, they contradict the MRM evaluations of $P(CC)$ and $P(FA)$ (e.g. MRM for $P(CC)$ and $P(FA)$ conclude that the predictions for sensor layout 5 has the greatest deviation from the experimental observation; however, MRM of $P(MD)$ shows that prediction and observation for sensor array 5 deviate by less than 0.5 percentage points with 100% confidence).

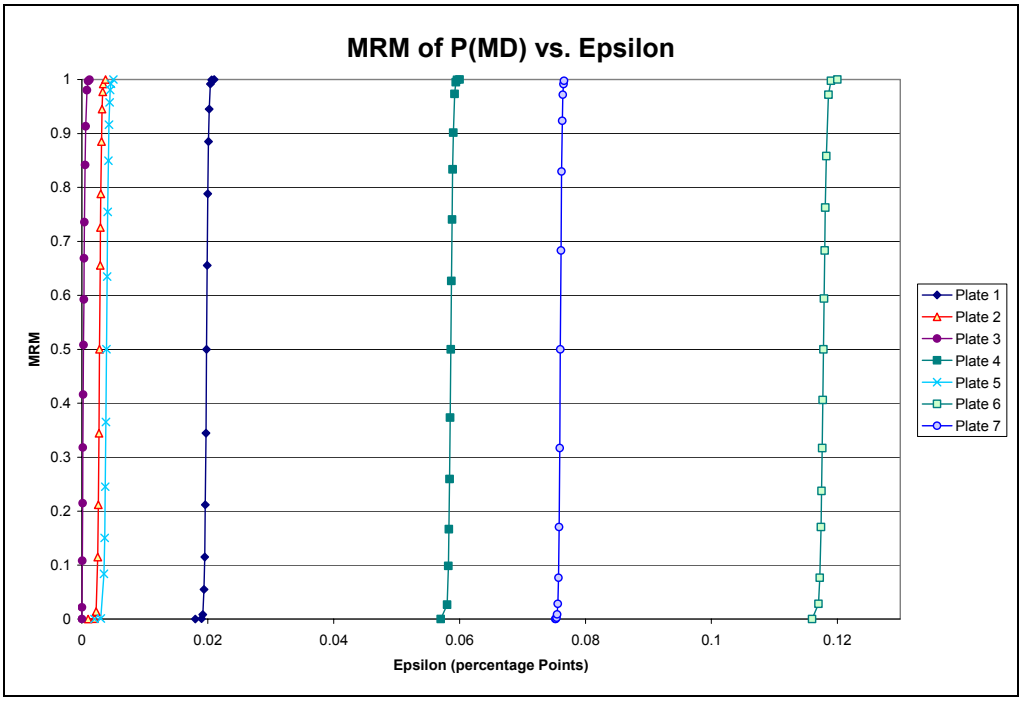

Figure 33. MRM vs. ε for P(MD) performance measure.

Applying MRM similarly to data corresponding to the experimentally observed performance measures (i.e. where Θ is a single analytically derived performance measure, while $\bar{x}$ and s are the estimated sample mean and standard deviation of the experimental performance observations, respectively) yielded erroneous results. Random partitioning of the experimentally observed training and testing data sets caused the performance measures to improve drastically in comparison to results obtained from an ordered 50-50 split. Temporal trends within the features used for classification were found (i.e. the feature space was not stationary in time presumably due to small wear and tear changes in the plate, washers, and bolts, that were observed at each fastener location). This obviously put strain on the classifier when testing data derived from a chronologically ordered 50-50 partitioning, while drastically simplifying classification when the data set is randomly permutated and then partitioned. Therefore, MRM was not applied in this fashion.

It should also be noted that the assumption of Normality does not hold for all performance measures due to several reasons. First, the performance measures are probabilistic and are limited to the range [0, 1]. Second, the particular performance measures considered in this study are either very close to zero or very close to 1.0 causing significant skewness in the distributions. Thirdly, due to the finite number of samples that are used to construct the classification matrices, the performance measures can only take on a finite number of discrete values (e.g. $P(CC) \in \left\{\frac{1}{j}, \frac{2}{j}, \ldots, \frac{j}{j}\right\}$, where j is the number of samples used to construct the classification matrix, i.e. 500). It might be argued that due to the central limit theorem, as j increases and becomes large, the performance measures approximately follow a Gaussian distribution; however, the data set utilized in this work does not illustrate this and the use of Equation (5) is loosely applicable at best.

In general, the application of the model reliability metric showed that sensor configuration 5 is likely an outlier. MRM also indicated that an allowable difference of 15 percentage points is needed to consider the predicted performance measures as equal to the observed performance measures. It should be noted that due to the violation of a major assumption of Equation (5), this MRM application may be invalid; however, as will be seen in the subsequent section, the results are consistent with other probabilistic validation assessments.

5.3.3 Classical and Bayesian Hypothesis Tests and Confidence Bounds

Paralleling classical hypothesis tests, confidence bounds may be constructed for the sensor layout performance measures via the binomial distribution, if each attempt at classifying a recorded set of signals from the group of testing data is considered an independent and identically distributed event that can have only one of two outcomes: classified correctly or misclassified. Clearly, the probability, P, that l of these n events fall into one of those groups is given by the binomial law, $P_l = \left(\frac{n}{l}\right) P^l (1-P)^{n-l}$, where the expected value for l is nP and l/n is the estimate for the probability P. Upper and lower confidence bounds can then be constructed for any given confidence level, α, by following Johnson, et al.[90] The results are presented graphically in Figure 34, Figure 35, and Figure 36, where upper and lower 95% confidence bounds for both experimentally observed and analytically derived performance measures were determined.

As can be seen from the interval plots, there is significant overlap of the confidence intervals corresponding to sensor arrays 2 and 3, while for sensor configurations 1, 4, 5, 6, and 7 little to no overlap exists. It should be noted that this type of comparison is analogous to constructing 2-sample hypothesis tests *without* the requirement of multiple independent samples from a

Gaussian distribution. The evidence supports the rejection of $H_O : \mu_A = \mu_X$ at the 5% confidence level, if there is no overlap of the confidence bounds corresponding to the two performance measures considered.

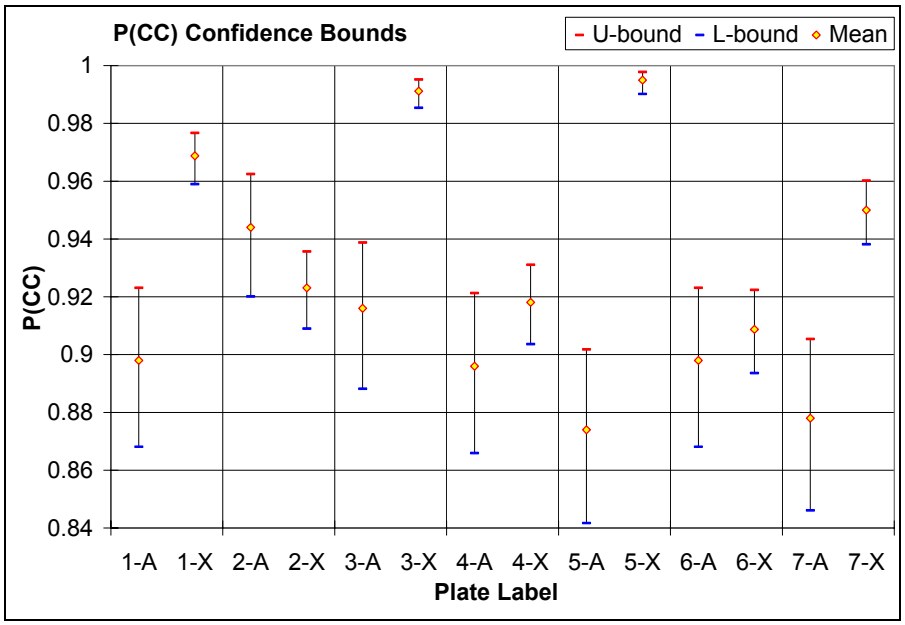

Figure 34. Graphical comparison of confidence bounds corresponding to P(CC).

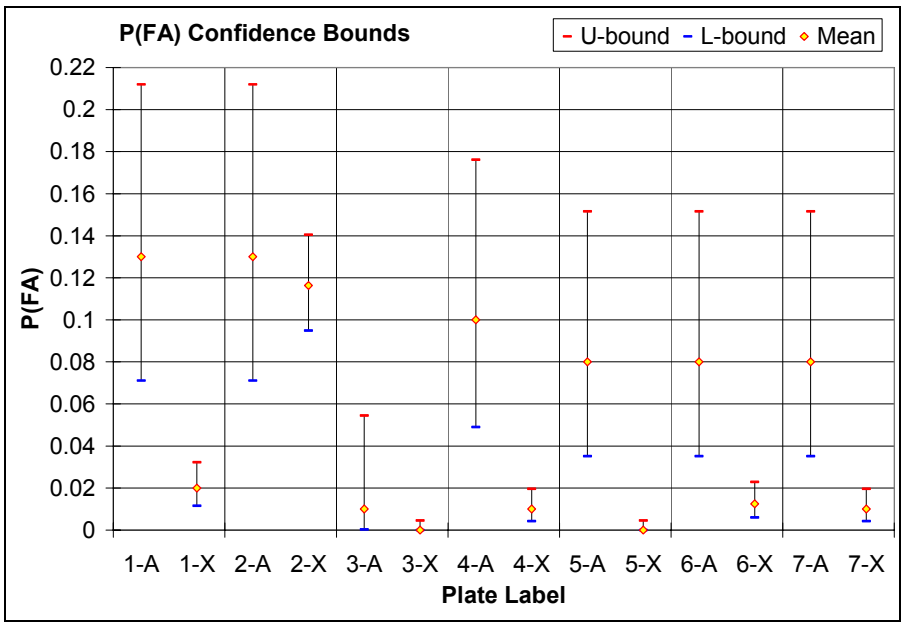

Figure 35. Graphical comparison of confidence bounds corresponding to P(FA).

In Figure 34, Figure 35, and Figure 36, a "plate label" is given to each sensor layout performance measure, where "A" represents analytical prediction and "X" represents experimental observation (e.g. the confidence interval labeled "3-A" corresponds to the analytical prediction of sensor configuration 3).

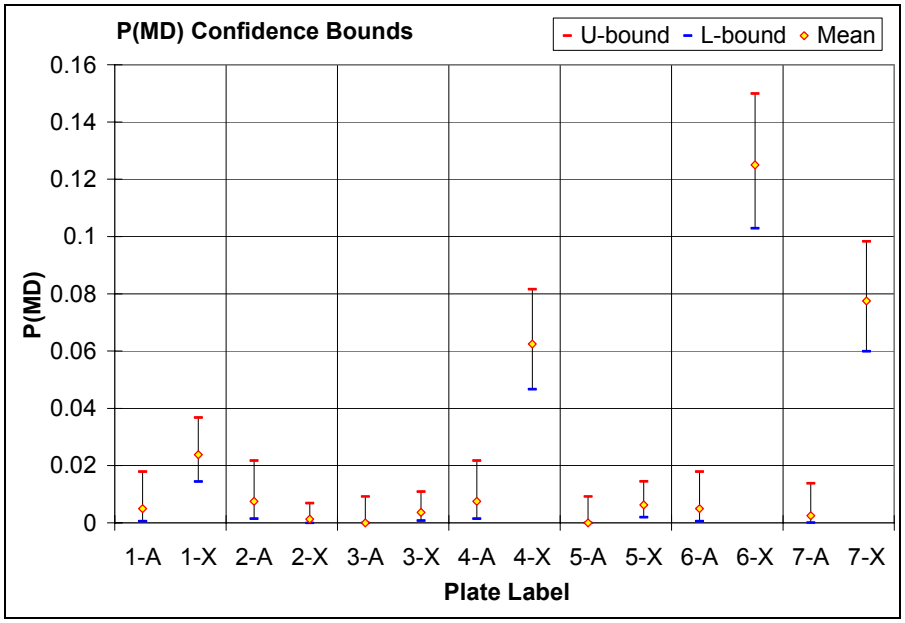

Figure 36. Graphical comparison of confidence bounds corresponding to P(MD).

Similar to the comparisons made with MRM, the results in Figure 34, Figure 35, and Figure 36 are more critical of the differences between prediction and observation than correlation analyses. Only sensor array 2 shows overlap with respect to all three performance measures. Conversely, only sensor configuration 7 contains no overlap with respect to all three performance measures, while all other sensor configurations show mixed results. Therefore it is difficult to draw a significant conclusion from these comparisons; at best one can say that although some prediction

capability exists, there is significant room for improvement of the performance measure prediction methodology.

In addition to this graphical comparison, Table 33 shows the *p*-values for the hypothesis tests constructed via Student's 1-sample *t*-statistic. Only one test has a *p*-value greater than 5%. This leads to the conclusion that the analytically predicted performance measures are statistically different from the experimentally observed ones.

Table 33. Results: hypothesis test via Student's *t*-statistic.

	P(CC)		P(FA)		P(MD)	
Plate	t-statistic	p-value	t-statistic	p-value	t-statistic	p-value
1	59.08	5.2631E-79	44.95	1.1127E-67	79.20	2.3981E-91
2	19.48	1.1896E-35	12.16	2.3531E-21	11.20	2.6947E-19
3	60.46	5.6463E-80	22.95	2.0107E-41	0.69	0.49202447
4	22.16	3.6849E-40	37.32	4.0393E-60	189.03	1.782E-128
5	85.29	1.731E-94	47.12	1.2885E-69	13.45	4.5308E-24
6	8.94	2.2329E-14	29.61	5.4842E-51	280.48	2.082E-145
7	43.37	3.2514E-66	32.72	6.9617E-55	361.90	2.344E-156

The Bayesian hypothesis testing results via the definitions of Section 3.2.3 are given in Table 34 and agree well with the results of classical hypothesis testing due to identical assumptions (i.e. the performance measures are normally distributed) and statistical strictness. All but one Bayesian hypothesis test require the rejection of the null hypothesis. Similarly to the results of classical hypothesis testing, only $P(MD)$ of sensor configuration 3 accepts H_0 with a confidence of 88.2%.

Table 34. Results: Bayes' Factor.

Plate	P(CC)	P(FA)	P(MD)
1	0	0	0
2	3.1810E-81	2.5499E-31	1.5297E-26
3	0	6.5595E-113	7.4762
4	9.5909E-106	2.6947E-299	0
5	0	0	1.1130E-39
6	4.0803E-17	3.1208E-188	0
7	0	5.3836E-229	0

The results of classical and Bayesian hypothesis tests provide evidence for the rejection of the null hypothesis test. However due to the underlying assumption of normality for both test statistics (*p*-value and Bayes' factor), it is beneficial to also consider the results of the graphical confidence intervals, which parallel two-sample hypothesis tests *without* the assumption of normality. The results of this graphical analysis are mixed and inferring a precise conclusion is difficult. Although correlation exists between analytical performance prediction and experimental observation, considerable improvement of the performance measure prediction methodology is necessary.

5.3.4 Multivariate Validation via Bootstrapping

In the previous comparisons conflicting inferences were made due to the inconsistent behavior of the validation metrics with respect to the three sensor layout performance measures and seven sensor configurations. In order to obtain an overall measure of how well the prediction methodology performs for different sensor arrays, a multivariate comparison that includes $P(CC)$, $P(FA)$, and $P(MD)$ all at once must be made for each of the seven sensor configurations. Therefore, applying MRM to all three performance measures simultaneously requires a multivariate formulation of r and the joint probability density functions describing the distribution of the performance measure vector. Similar to Section 3.4.3, it is suggested that

$r^* = P\left(|D_1| < \varepsilon_1 \cap |D_2| < \varepsilon_2 \cap \cdots \cap |D_m| < \varepsilon_m\right)$ for comparing m number of elements simultaneously and using bootstrap to estimate the joint probability density function. Here D_1 to D_m are the differences between the m sensor layout performance observations and predictions and ε_1 to ε_m are the corresponding allowable discrepancies. r^* is estimated by finding the ratio between the number of bootstrap samples for which $|D_1| < \varepsilon_1 \cap |D_2| < \varepsilon_2 \cap |D_3| < \varepsilon_3 \cap \cdots \cap |D_m| < \varepsilon_m$ is true and n_B. Utilizing the bootstrap method in this way preserves the correlation structure inherently present among the three performance measures. Figure 37 shows the joint MRM (or $P\left(|D_1| < \varepsilon_1 \cap |D_2| < \varepsilon_2 \cap |D_3| < \varepsilon_3\right)$) of the three performance measures, $P(CC)$, $P(FA)$, and $P(MD)$, for the seven sensor configuration, where $n_B = 200$, $m = 3$, $k = 100$, and $\varepsilon_1 = \varepsilon_2 = \varepsilon_3$.

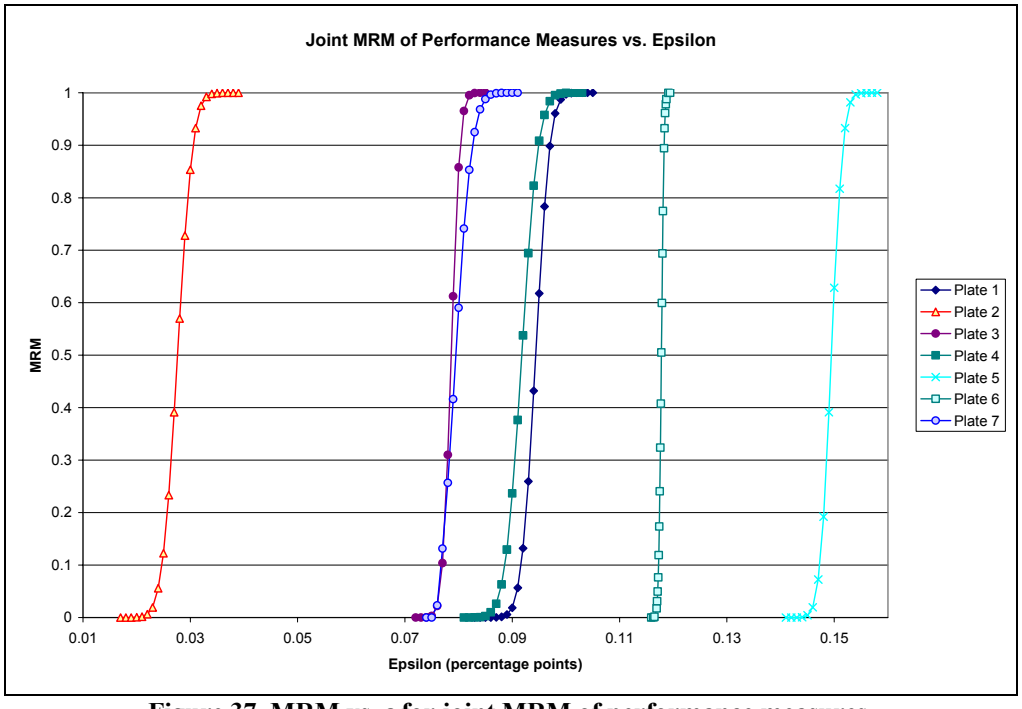

Figure 37. MRM vs. ε for joint MRM of performance measures.

As is clearly evident from the plots, a joint MRM of 1.0 for all sensor configurations simultaneously is possible only for an allowable difference between prediction and observation of approximately 15.6 percentage points (i.e. $\varepsilon_1 = \varepsilon_2 = \varepsilon_3 = 0.156$). However, if test plate 5 is considered an outlier, as it was in previous comparisons, the allowable difference needed to obtain an MRM of 1.0 is reduced to approximately 11.9 percentage points (i.e. $\varepsilon_1 = \varepsilon_2 = \varepsilon_3 = 0.119$). These results are in agreement with previous MRM conclusions. It should be noted here that although the small value of ε required to obtain a MRM of 1.0 for sensor layout 2 seems favorable, it is likely that the result for this sensor array is also an outlier. Therefore considering only test plates 1, 3, 4, 6, and 7, an allowable difference between performance prediction and laboratory observation of approximately 9.25 percentage points (i.e. $\varepsilon_1 = \varepsilon_2 = \varepsilon_3 = 0.0925$ on average) can be expected to obtain a joint probability MRM of 100%.

Due to the correlation between performance measures (see Table 35), the joint cumulative probability curves in Figure 37 closely follow the MRM curves corresponding to the performance measure with the smallest MRM (i.e. the joint MRM is most similar to the MRM corresponding to the performance measure that requires the largest ε to achieve 100% confidence) for a given sensor configuration. For example, $P\left(\left|D_1\right| < \varepsilon_1 \cap \left|D_2\right| < \varepsilon_2 \cap \left|D_3\right| < \varepsilon_3\right)$ of the performance measures for sensor configuration 6 most closely resembles the MRM curve for $P(MD)$ (see Figure 33).

Table 35. Correlation coefficients of performance measures.

	P(CC)	P(FA)	P(MD)
P(CC)	1	0.25 - 0.44	0.10 - 0.28
P(FA)	0.25 - 0.44	1	0.07 - 0.32
P(MD)	0.10 - 0.28	0.07 - 0.32	1

From the multivariate validation assessment, it can be concluded that in order to accept all three performance measure predictions with high confidence, a significant allowable difference between predictions and observations must be available. Therefore it is concluded that the difference between prediction and observation is significant, such that the prediction methodology cannot be considered validated with high confidence.

5.3.5 Validation Assessment Inferences

In this section, the methodology for SHM sensor layout performance prediction was applied to 7 different sensor configurations and evaluated with results compared to experimentally observed performance measures for the same sensor configurations. The analytically determined results were found to be correlated to experimental observations via the correlation and trend line comparisons, while significant differences between prediction and observation were found with MRM, confidence interval, and classical and Bayesian hypothesis testing. Significant improvements need to be made to the prediction method in order to reduce the discrepancies between prediction and observation corresponding to different sensor configurations (see Table 28 and Table 32).

One important insight gained regarding the hierarchical propagation of error through the SPO methodology is that second stage validation requires that the first stage is validated to a significantly high degree – much higher than previously assumed adequate. See Figure 28 and Figure 29. Seemingly insignificant discrepancies between prediction and observation at the FEM level will propagate through subsequent procedures and processes and compound with modeling and processing errors to yield substantial differences between prediction and reality at the damage detection (probabilistic performance measure) level. In Chapter 3 the stochastic

finite element model was validated based on the natural modes of vibration, whereas the model's subsequent use was to predict the structure's response to a sine sweep excitation. In addition, to reduce simulation runtime by decreasing the number of degrees of freedom of the analysis, modal superposition (MSP) is utilized for transient analysis of the SFEM. Modeling and processing errors that reduce the accuracy of the SFEM output are associated with this use of the validated stochastic FEM model. The following section provides a comparison of the predicted structural response to the sine sweep excitation and the experimentally observed response obtained via the procedure defined in Section 5.2.

5.4 Comparison of Predicted and Observed Displacement Response

In order to compare the predicted signal (displacement) to the observed signal (voltage), they must be made comparable. The piezoelectric sensors utilized in the experimental phase of this study are used as transducers in a radial expansion mode, where a voltage is applied (actuator) or measured (sensor) across the thickness of the piezoelectric material and a strain is created or sensed in the radial direction. The amount of electric field generated due to an imposed strain can be calculated based on the properties of the piezoelectric material. The sensors and actuators utilized in this study are made of APC 850 piezoelectric material with a piezoelectric constant, $C_{material} = -1.75 \times 10^{-12}$ meter/Volt, which relates the radial strain to the electric field as follows.

$$C_{material} = \frac{\left(\Delta d / d\right)}{\left(V / t\right)} \tag{23}$$

where Δd is the change in the diameter of the sensor/actuator (to be compared to the predicted displacement response), d the unstrained diameter of the sensor/actuator, V the voltage measured, and t the thickness of the sensor/actuator. For the sensors/actuators utilized in this

study, $t = 2.54 \times 10^{-4}$ meter and $d = 6.35 \times 10^{-3}$ meter. Applying Equation (23) to the experimentally observed voltage signals shown in Figure 38 and utilizing the displacement time histories of the SFEM analysis shown in Figure 39, the following comparisons may be made.

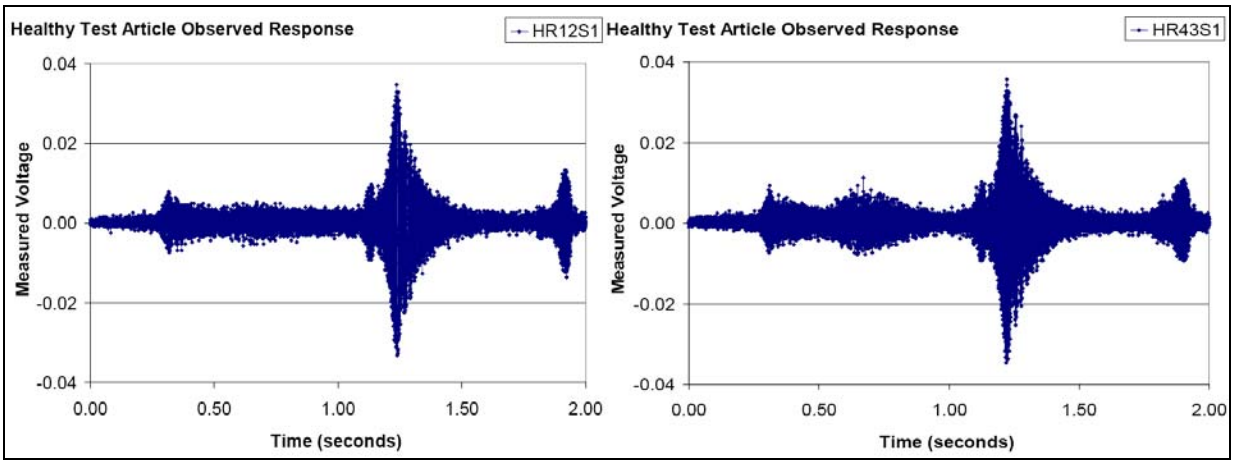

Figure 38. Healthy observed structural response for two measurements.

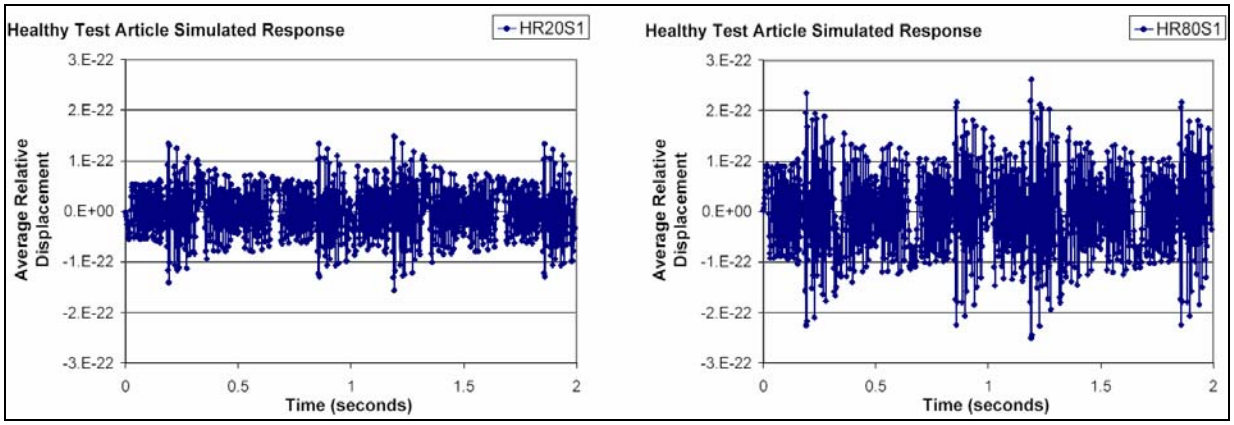

Figure 39. Healthy simulated structural response for two realizations of the random model inputs.

Figure 38 and Figure 39 show the predicted and observed structural response signals, respectively, where the predicted displacement response is obtained by averaging the relative displacement between the FEM node at a given location and its four nearest neighboring nodes.

This provides an averaged relative displacement comparable to Δd. Discrepancies between the signals shown in Figure 38 and Figure 39 are visually noticeable.

In order to compare the features of these signals, the autocorrelation functions and power spectral densities (PSD) were estimated and are shown in Figure 40 and Figure 41, respectively. Discrepancies are easily noted. It should be pointed out that the large spike at around 100 Hz in the PSD of the experimental observation likely consists of higher order frequency content folded into the lower frequency spectrum due to aliasing errors. The Shannon Sampling Theorem[80] was violated by utilizing a sampling rate not equal to twice the highest frequency at which the signal has energy thereby aliasing higher order frequency content. That is the sampling frequency of 500 Hz is much less than the Nyquist sampling rate of 3,000 Hz, which is twice the maximum input frequency of 1,500 Hz.[80] However, this still does not warrant the large discrepancies between the predicted and observed PSD's, since identical input excitation functions and sampling rates were utilized during simulation and experimentation, and one should also expect such a spike in the PSD of the simulated structural response. In addition, to quantitatively compare model predictions and experimental observations, Table 36 lists the first five central moments of the autocorrelation and PSD functions of the experimentally observed and analytically predicted structural response signals.

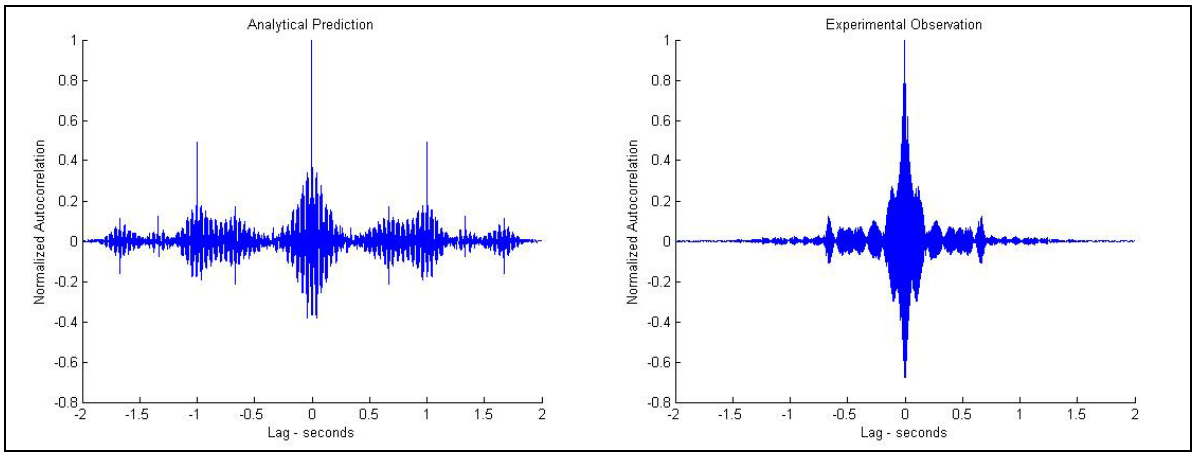

Figure 40. Autocorrelation of analytical prediction and experimental observation.

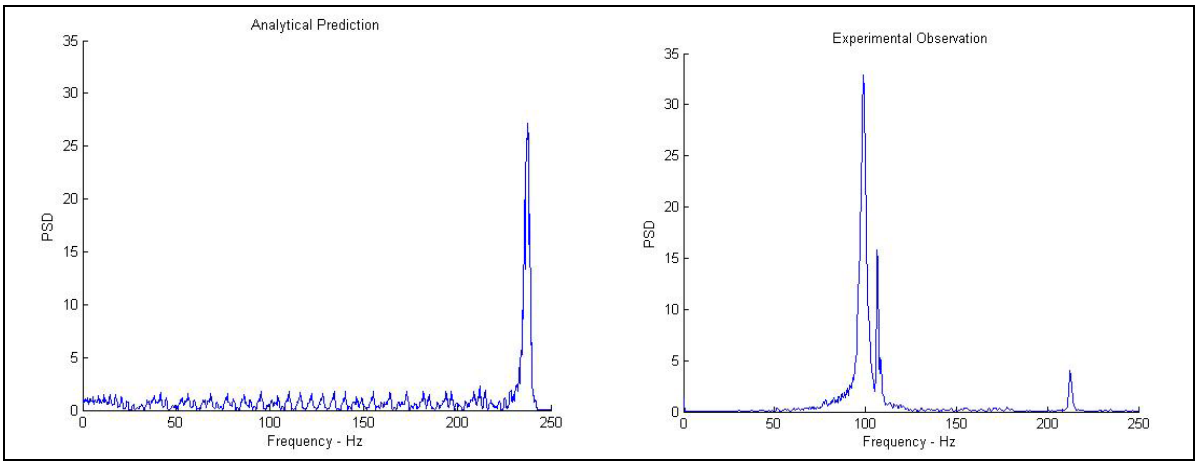

Figure 41. PSD of analytical prediction and experimental observation.

Table 36. Central moments of autocorrelation and PSD.

Moments	1	2	3	4	5
Experimental Autocorrelation	0.001071	0.00716	0.000158	0.001979	0.000465
Predicted Autocorrelation	0.000595	0.00652	0.000568	0.000822	0.000520
Experimental PSD	0.9996	12.295	261.46	6635.1	178857
Predicted PSD	0.9983	6.299	121.42	2667.3	61034

From the plots shown in Figure 38, Figure 39, Figure 40, and Figure 41, it is easily seen that the model predictions of the structural response of the test article to a sine sweep input excitation does not agree with the experimentally observed measurements of the same signal. The

discrepancies between the moments of the autocorrelation and PSD functions of the signals in Table 36 further show the model's inadequacy. These differences between prediction and observation at the FEM level obviously affect the accuracy with which the sensor layout performance prediction may be estimated.

Due to the utilization of the SFEM for predicting the response of the test article to a sine sweep excitation, model validation via modal testing is inadequate. Model calibration with respect to the response time histories is required before further analysis/design. The experimental data obtained during the laboratory test of the seven sensor configurations may be utilized for calibration and subsequent validation of the SFEM using a *leave-one-out* cross-validation approach. The model may be calibrated to different combinations of six out of the seven sensor layouts and their respective structural response time histories, while the remaining seventh sensor layout and its structural response time histories may be used for validation.

Several simulation parameters that may lend themselves to calibration efforts are structural and material damping constants, integration time step size, as well as boundary conditions. Ansys[6] notes that even small discrepancies between the model's damping constants and real damping coefficients can lead to incorrect results. Stiffness-weighted and mass-weighted damping may be defined, where generally stiffness proportional or beta damping is effective for oscillatory motion at high frequencies, while mass proportional or alpha damping is effective for low frequencies and will damp out rigid body motion. These parameters (alpha and beta) may be candidates for calibration. For the current SFEM analyses a constant damping ratio of 0.03 is utilized. Secondly, the integration time step of the transient dynamic analysis is critical with respect to solution accuracy. Several different approaches to selecting time stepping include time step bisection, response eigenvalue, response frequency, creep time increment, and

plasticity time increment.[6] Time step size, which significantly impacts the simulation time required, may also provide calibration ability. For the current SFEM analyses automatic time stepping is used within Ansys, where the load step factor is equal to 1.0 and the largest possible time step is specified as 0.002 seconds. Thirdly, boundary conditions such as stiffness constants and nodal constraints are also available for calibration. Model improvements such as better simulation of the bolted boundary conditions, as well as improved modeling of the actuator, may produce more agreeable results.

Model calibration can be achieved via manual or systematic alteration and adjustment of model input parameters. In some cases Bayesian updating may prove to be appropriate; however, for the problem at hand of matching the features of the predicted and observed time history responses (e.g. moments of their corresponding autocorrelation and PSD functions), the Bayesian perspective may not be easy to implement. A least squares optimization approach may have potential, where the model input parameters are the optimization variables and minimizing the sum of squares of the errors is the objective.

5.5 Conclusions

This chapter investigated the validation assessment of the sensor layout performance prediction. It was shown that although highly correlated, the analytical predictions were different from experimental observations. The discrepancy between prediction and observation was statistically significant.

With respect to the different types of validation metrics used in this assessment, it is observed that comparisons based on correlation (i.e. MAC, trend lines, etc.) produce much more favorable results than stricter, more discriminating validation metrics such as the MRM, and classical and

Bayesian hypothesis tests. Utilizing statistical validation metrics (i.e. metrics that include the uncertainty of the variables being compared) allows for a much more detailed and quantitative comparison.

Additionally, the need for validating the time history responses to the sine sweep input excitation, in addition to the natural modes of vibrations, of the SFEM was demonstrated. This will help reduce the compounding effect of error propagation within the sensor layout performance prediction process. Calibration of the SFEM with respect to the structural response to excitation may produce more accurate damage detection and sensor layout performance prediction.

For the sake of demonstrating the sensor placement optimization methodology developed in Chapter 6, the FEM model of Chapter 2 is utilized without any further calibration. Realistic application of the proposed optimization methodology requires the calibration and validation of the model as discussed above before use in optimization.

CHAPTER VI

SENSOR PLACEMENT OPTIMIZATION

This chapter addresses sensor placement optimization (SPO), research Objective 4. Section 6.1 presents a brief literature review of sensor/actuator placement optimization and outlines the general approach utilized in this study is outlined. Section 6.2 investigates the search domain with respect to the variability of the performance measures. The Snobit[10] approach is utilized to perform the actual SPO and is presented in detail in Section 6.3. SPO results with respect to the example application are presented in Section 6.5.

6.1 Introduction

Several studies have explored methods for sensor placement optimization during recent years. Hiramoto, et al,[91] as well as Abdullah, et al,[92] have addressed the need to place actuators in an optimal way to control the behavior of dynamic structures. The former uses the explicit solution of the algebraic Riccati equation, and the latter utilizes genetic algorithms, to solve the optimization. Genetic algorithms (GA) have also been employed to search for optimal locations of actuators in active vibration control.[93,94,95,96] With respect to SHM, Guo, et al,[97] use a GA approach and a sensor placement optimization performance index based on damage detection to search for an optimal sensor array, and Spanache, et al,[98] use GA and account for economic/cost issues in the design of a cost optimal sensor system. Gao and Rose[99] use GA in combination with evolutionary computation to develop an SPO for SHM framework. However, GA-based sensor/actuator placement optimization methods often generate invalid strings during the

evolution process and require a predefined number of discrete sensor configurations, which do not guarantee global optima.

Related more closely to SPO of SHM systems of next generation flight vehicles, Li, et al,[100] proposed an algorithm that aims to identify a sensor configuration that recognizes different modal frequencies and mode shapes most efficiently, as well as increases the signal to noise ratio. However, it is not shown that a sensor array that best identifies modal frequencies and mode shapes optimizes more traditional SHM performance measures such as the probability of correct classification. Gao and Rose[101] define a probabilistic SPO approach, where a probabilistic damage detection model that describes detection probabilities over a confident monitoring region with radius R is defined for each sensor of a given sensor set. The effectiveness of the sensor network with respect to a given damage location is then assumed to be the joint effectiveness of all sensors. It is estimated as the union of the individual sensor detection probabilities for all sensors in the network. A covariance matrix adaptation evolution strategy is used to search the decision variable domain. Major shortcomings of this approach include oversimplified probabilistic damage detection models and unspecified types and sources of uncertainty. A similar SPO framework that addresses imprecise detection probabilities as well as uncertain search domain properties is proposed by Dhillon, et al.[102]

Additionally, recent studies by Lim[103], Padula and Kincaid[104,105,106], and Raich and Liszkai[107] have provided the following insight into the problems and issues involved in SPO. Integer and combinatorial optimization methods were used extensively in their studies to optimize the placement of actuators for vibration control and noise attenuation. In general, most of the approaches identified in the literature can be summarized as: "given a set of n candidate locations, find the subset of a locations, where $a << n$ which provides the best possible

performance." This has the obvious requirement of having to select *a priori* the number and positions of possible sensor locations. Choosing values of *n* and *a*, as well as potential sensor locations, is a subjective task and, as Padula and Kincaid[104] point out, can cause significant variation of the optimal solution.

Additional discussions by Padula and Kincaid,[104,106] and Raich and Liszkai[107] point out that the performance measure can be quite different from problem to problem and may prove to be very complex. In general, however, the performance function is linear and can easily be optimized. Most often the cumbersome component of these optimizations is to satisfy all of the constraints. The optimization method must be able to balance the expected performance over all conditions. A chosen optimization approach may need to impose heuristic constraints, to satisfy operational as well as geometric constraints.

In addition to optimal sensor placement, the underlying goals of Raich and Liszkai[107] include the minimization of the number of sensors placed on a structure while simultaneously increasing the amount of information gathered by the sensors, making this optimization approach multi-objective. Raich and Liszkai use an information measure that is based on the sensitivities of the frequency response function with respect to damage indicators. This optimization method, as well as most others found in the literature, is deterministic.

Conversely, multivariate stochastic approximation using simultaneous perturbation gradient approximation allows for the inclusion of noise in function evaluations or experimental measurements and shows to be very efficient for large-dimensional problems.[108] A significant drawback of this particular methodology, however, is its gradient approximation, which, as all other gradient-based optimization methods, does not guarantee a global optimum.

In addition to the approaches briefly presented above, Tabu search[109] is a heuristic optimization scheme that uses *short* and *longer term memory* as well as *critical event memory* to identify feasible solutions that are well-distributed across the search domain and global in terms of optimum. Unfortunately Tabu search does not guarantee an optimum solution (neither locally, nor globally) and is quite computationally intensive due to its "brute force" nature.

It should be noted that "design under uncertainty," has been well established within the context of reliability-based optimization (RBO). In RBO the objective function is usually linked to weight or cost and the uncertainties of the input variables is addressed and included via reliability requirements as the constraints. These types of problems are usually solved via two loops; one loop performs the reliability calculations, while the second loop performs the optimization algorithm. Coupled and decoupled approaches have been proposed in the literature[110] in an attempt to make efficient use of computational efforts.

The literature reviewed above addresses optimization of sensors or actuators placement only in a deterministic fashion, and general optimization methods that do include uncertainty are gradient-based and do not guarantee global optimum – especially for applications with noisy objective functions. This study develops a method for SPO under uncertainty, which – although gradient-based – does search the feasible space in such a way as to produce global optima in the presence of uncertainty (i.e. noise). This is achieved via the application of Snobfit[10] to SPO.

6.2 Investigation of Performance Measure Variability

In this section, a sensitivity analysis of the performance measures (as estimated via the sensor layout performance prediction method of Chapter 4) with respect to each of the coordinates defining a given sensor configuration is investigated. Given that there are three sensors (S2, S3,

and S4) monitoring and recording the structural response of the test article from which the probabilistic performance measures are derived, six coordinates exist that describe each sensor configuration uniquely and each sensor array can be investigated with respect to each one of the six coordinates defining it. Figure 42 shows contour plots of the performance measures with respect to the location of SHM sensor S2. In the plot of $P(CC)$, which should be maximized, red areas are favorable; whereas in the plots of $P(FA)$ and $P(MD)$, which should be minimized, blue areas are favorable. Cubic interpolation was used to generate these plots from several hundred evaluations of the performance measures at various locations on the test article. The plots show that although optimal regions for sensor placement exist, the response surface is quite variable. In Figure 42 the position of sensor S3 and S4 were held constant at locations (8.5, 3.5) and (3.5, 3.5), respectively, while the coordinates of sensor S2 took values in the ranges [6.0, 11.75] and [6.0, 11.75] for coordinates $S2_x$ and $S2_y$, respectively. It should again be noted that all coordinates are given with respect to the bottom left corner of the plate as shown in Figure 1b and are specified in inches. From Figure 42 it is clearly evident that location (8.5, 8.5), as specified for sensor layout 1 in Table 27, is not the "best" location for sensor S2 with respect to all three performance measures. Considering the variability and magnitude of $P(CC)$, as well as the constraint that each sensor must remain within its quadrant, location (6.0, 6.0) appears to be a good location to place sensor S2. Under the same constraints, location (10.0, 10.0) would be a good placement for sensor S2 considering $P(FA)$, and location (7.0, 6.0) or location (10.0, 11.0) considering $P(MD)$. Figure 42 reiterates the need for SPO.

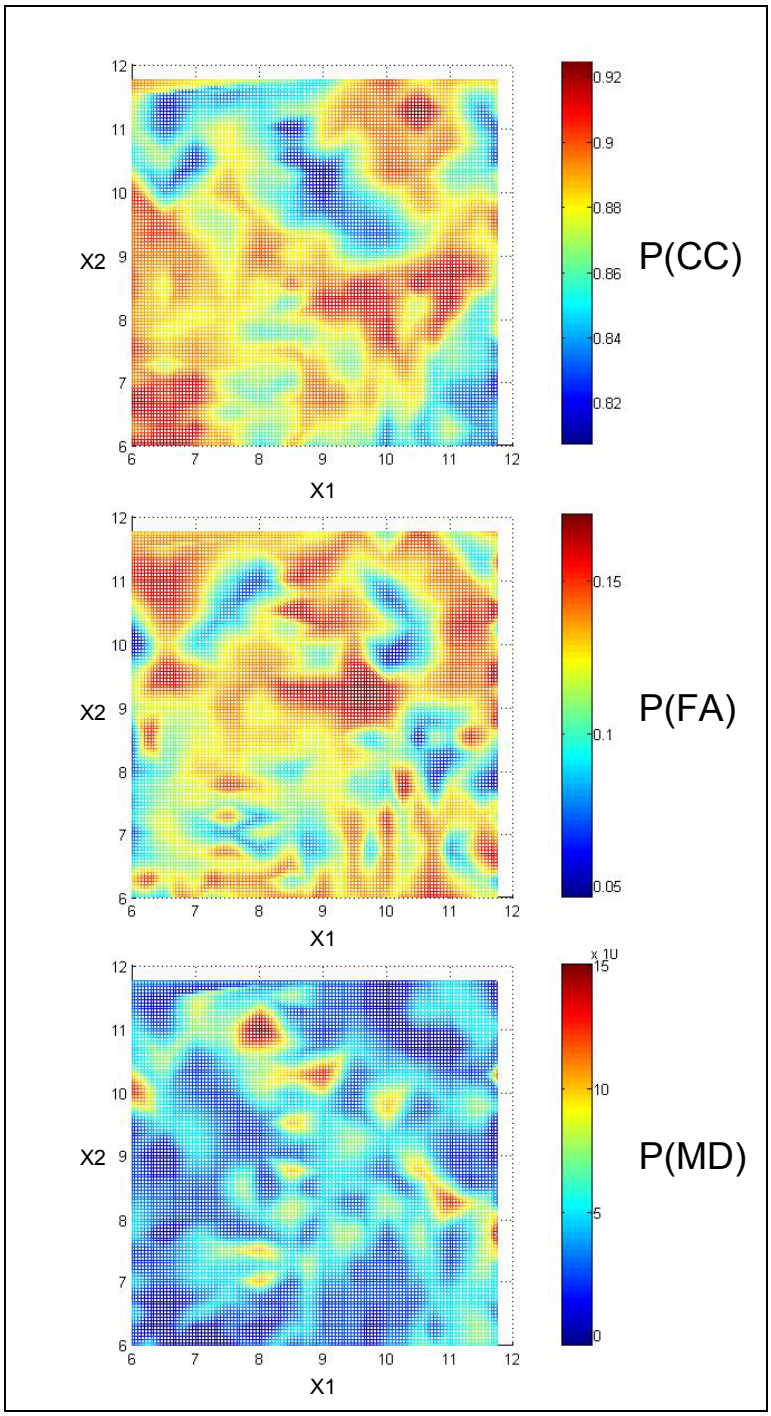

Figure 42. Performance measures versus sensor S2 location (X1, X2).

The above subjective qualitative analysis also supports the necessity of a more quantitative multi-objective assessment of the performance measures such as provided by Equation (22). Figure 43 plots the contour maps of the multi-objective performance functions listed in Table 37

(i.e. the fourth and fifth objective functions as defined in Section 6.5), which should be minimized. Blue regions are favorable. Considering the plots of Figure 43, location (6.0, 6.0) appears optimal and robust. Further investigation and analysis of these plots need to take place in a quantitative manner before conclusions can be drawn.

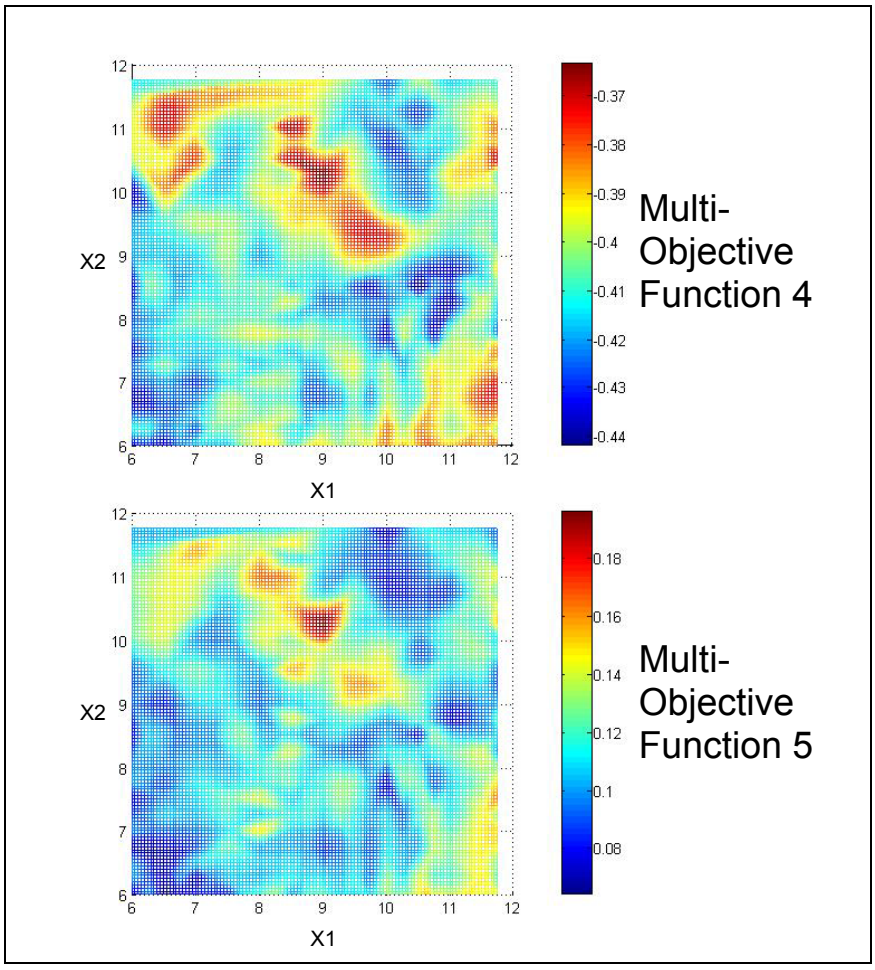

Figure 43. Multi-objective performance measures versus sensor S2 location (X1, X2).

In addition to showing that there are "optimal" regions on the test structure for placing SHM sensors, Figure 42 and Figure 43 show that the performance measures are quite noisy with respect to sensor location. This is exceptionally evident in the plots of $P(CC)$ and $P(FA)$ in

Figure 42, where the performance measures are shown to vary by as much as 240% over a distance of less than 1.0 inch. Therefore it is concluded that quantitative sensor optimization (perhaps multi-objective) is necessary and that an optimization scheme specifically designed for noisy objective functions is needed. As will be shown in the next section, Snobfit[10] is a good choice for this example application.

6.3 Snobfit Method

An appropriate approach to SPO that includes uncertainty is to employ Snobfit[10] (Stable Noisy Optimization by Branch and Fit), an optimization scheme that is designed for bound-constrained optimization of noisy objective functions, which are costly to evaluate due to computational or experimental complexity. A major advantage of using Snobfit is that the algorithm does not require a previously determined set of candidate sensor locations, but rather considers the following optimization problem.

$$\begin{aligned} &\min f(x) \\ &s.t.\ x \in [u,v] \end{aligned} \tag{24}$$

where x is continuous and $[u,v]$ is a bounded box in $\Re^n$ with a nonempty interior.[10] The Snobfit algorithm (programmed in Matlab[111]) as developed by Huyer and Neumaier[10] is used to solve the optimization formulation given by Equation (24) iteratively. Snobfit is designed specifically to handle the following difficulties that arise during the application of SPO on the test article.

- The function values are expensive to evaluate (i.e. obtaining the performance measures for a given sensor layout is computationally intensive).
- Instead of a function value requested at a point x, only a function value at some nearby point $\tilde{x}$ is returned (the finite mesh size of the FEM models restricts that "sense-able"

responses required by the damage detection algorithm to estimate the performance measures are available only at nodal locations).

- The function values are noisy (due to the finite number of simulations utilized to construct the confusion matrix, there is a finite precision/resolution with which the performance measures can be estimated).
- The objective function may have several local minima (as shown in Section 6.2, the performance measures are ill behaved with many local optima).
- Gradient information is not readily available.

Snobfit initiates each iteration by partitioning of the search domain and constructs local quadratic models of the response function. Snobfit combines local and global searches and allows the user to determine which of these searches is to be emphasized. It also produces a user-specified number of suggested evaluation points during each iteration of the optimization to inform the user of areas in the search domain that require additional information on the objective function.

The algorithm as developed by Huyer and Neumaier[10] within Matlab[111] searches for a solution to the problem in Equation (24) by repeated "calls" to a Snobfit function. In each call to Snobfit, a set of K distinct points x^k, for $k = 1,...,K$, and $K \geq 2$ (i.e. a set of K different sensor configurations), their corresponding objective function evaluations, f_k (i.e. their corresponding performance measures), the resolution of these function evaluations, Δf_k (i.e. the precision with which the performance measures were estimated), a natural number, n_{reg}, which specifies how many suggested evaluation points Snobfit should provide at the end of this iteration (i.e. Snobfit function call), two *n*-dimensional vectors *u* and *v*, where $u_i \leq v_i$, which specify the dimensions of the search domain, and a number $p \in [0,1]$, which allows the user to emphasize local (i.e. p is

close to 0.0) or global (i.e. p is close to 1.0) search, are required as inputs to the Snobfit function call.[10]

Snobfit initiates by splitting the search domain $[u,v]$ into K sub-domains, where each sub-domain contains exactly one point. When $K > 2$, the following procedure is applied.

while there is a subspace containing more than one point

choose the subspace containing the highest number of points

choose *i* such that the variance of $\frac{x_i}{v_i - u_i}$ is maximal, where the variance

is taken over all the points in that particular subspace;

sort the points such that $x_i^1 \le x_i^2 \le ...$

split the subspace in the coordinate *i* at $z_i = \lambda x_i^j + (1-\lambda)x_i^{j+1}$, where

$j = \arg\max\left(x_i^{j+1} - x_i^j\right)$ and $\lambda = \rho$ if $f\left(x^j\right) \le f\left(x^{j+1}\right)$ and

$\lambda = 1 - \rho$ otherwise; where $\rho = \frac{1}{2}\left(\sqrt{5} - 1\right)$ (i.e. the golden section number)

end while[10]

When $K = 2$, Snobfit chooses *i* such that $\frac{\left|x_i^1 - x_i^2\right|}{v_i - u_i}$ is maximal and continues as specified above.

The K subspaces $[u^*, v^*]$ are assigned *smallness* factors defined as $S = -\sum round\left(^2\log\left[\frac{v^*_i - u^*_i}{v_i - u_i}\right]\right)$, which are used to identify subspaces that are not yet well sampled (i.e. subspaces that are still relatively large with respect to other subspaces).[10]

To construct the quadratic models, a Hessian fit around the best point, x^{best} corresponding to the minimum objective function value, f_{best}, is computed by minimizing the sum of errors squared

defined as $\sum \varepsilon_k^2$, where $f_k - f_{best} = g^T s^k + \frac{1}{2}\left(s^k\right)^T G s^k + \varepsilon_k \left(s^k\right)^T H s^k$, $s^k = x^k - x^{best}$, and $H = \left(\sum s^l \left(s^l\right)^T\right)^{-1}$. G and g are determined by minimizing $\sum \varepsilon_k^2$. In order to speed up this process, the Snobfit algorithm actually performs an economy size QR-factorization $\left(s^1,...,s^K\right)^T = QR$, with an orthogonal matrix $Q \in \Re^{K \times n}$ and a square upper triangular matrix $R \in \Re^{n \times n}$. Here $K > n$ (i.e. Snobfit cannot start constructing quadratic models until there are more distinct sample points than dimension in the search domain). Then $H = \left(R^T R\right)^{-1}$ and $\left(s^k\right)^T H s^k = \left\| R^{-T} s^k \right\|^2$, for $k = 1,...,K$.[10]

Local quadratic fits around an arbitrary point *x* are determined similarly – utilizing only point *x* and its $n+5$ nearest neighbors – where a suitable multiple, γG, of the Hessian matrix *G* estimated above is utilized and the model error ε_k is defined by $f_k = f + g^T s^k + \frac{\gamma}{2}\left(s^k\right)^T G s^k + \varepsilon_k \sqrt{\Delta f_k^2 + \sigma_G^2 \beta_k^2}$, where $\beta_k = \left\| L\left(x^k - x^{best}\right) \right\|^2$ and $s^k = x^k - x$. The parameters f, $\gamma \in \Re$, and $g \in \Re^n$ are determined by the minimization of $\sum \varepsilon_k^2$. The factor $\sqrt{\Delta f_k^2 + \sigma_G^2 \beta_k^2}$ automatically adjusts, such that for points with inaccurate function values (i.e. a large Δf_k) and which are far away from x^{best} (i.e. a large β_k), a larger error in the fit is permitted.[10]

Then by minimizing the quadratic fit around the best point, x^{best}, and around all other points, *x*, in each subspace, Snobfit returns the current best point, the current best function value, a measure of the accuracy of the quadratic model at the best point, and n_{reg} suggested future evaluation points that are within the global search domain, $[u,v]$. The idea of the Snobfit

algorithm is to use these suggested points and their corresponding objective function values as the input of the next iteration of/call to Snobfit.[10]

The methods used to generate the n_{reg} points are grouped into five categories and proceed as follows. For group number 1, a single point is suggested by minimizing the quadratic model around, x^{best}, over $[\max(x^{best}-d,u),\ \min(x^{best}+d,v)]$, where d is a trust region radius. A second suggested point, of group number 2, is obtained by minimizing the quadratic model around x^{best} over $[\max(x^{best}-\rho d,u),\ \min(x^{best}+\rho d,v)]$, where ρ is the golden section number $\frac{1}{2}(\sqrt{5}-1)\approx 0.62$. For group number 1 and 2, if the suggested point of group 1 is not on the boundary of the specified search region, d is reduced such that the point falls on the new boundary and then used to specify the suggested point of group 2.

The next group of suggested points is generated by minimizing the quadratic models corresponding to points x from each of the subspaces $[u^*,v^*]$. This generates $K-1$ points, y, with corresponding model function values f_y. If for a given subspace $|x-y|<0.05(u^*-v^*)$, the new suggested point y is considered to be too close to x and must be replaced by

$$y_i'=\begin{cases} x_i+0.05(u^*-v^*) \text{ if } (y_i>x_i \text{ and } x_i+0.05(u^*-v^*)\le u^*) \text{ or } x_i-0.05(u^*-v^*)<u^*, \\ x_i-0.05(u^*-v^*) \text{ otherwise} \end{cases}$$

to yield a new suggested point and corresponding model value. A checking procedure is used to assure that these new suggested points are not copies or nearly copies of each other.

Additional points, grouped into group number 4, are taken from unexplored regions. For a subspace $[u^*,v^*]$ with corresponding point x, the point z is defined as

$$z_i = \begin{cases} \frac{1}{2}\left(u^*_i + x_i\right) & \text{if } x_i - u^*_i > v^*_i - x_i \\ \frac{1}{2}\left(x_i + v^*_i\right) & \text{otherwise} \end{cases}$$. Points z are then selected in order of increasing smallness of their corresponding subspace, where ties are broken by preferring points coming from subspaces corresponding to small function values $f(x)$. The fifth and final group of suggested points is essentially generated at random to assure that Snobfit returns a total of n_{reg} suggested points.[10]

The coordinates of all these points are rounded to integral multiples of the resolution vector, Δx, which is user specified, and a point is only accepted if it differs from all of the already sampled points by at least Δx_i in at least one coordinate direction. This has the effect that some calls to Snobfit may not return any points of group number 1 and/or group number 2.[10]

The objective function may then be evaluated at these suggested points and/or other locations for further Snobfit iterations. A stopping criterion must be defined by the user and may be heuristically applied.

6.4 Sensor Placement Optimization Method

The above defined Snobfit optimization algorithm was carried out for the example application. As discussed in Section 4.5 and again in Section 6.2, the variability of the performance measures with respect to sensor location, and the varying inferences as to which sensor array is optimum with respect to different performance measures, are best addressed via multi-objective optimization. Therefore Equation (22) is utilized in addition to three individual optimizations aiming to maximize $P(CC)$, and minimize $P(FA)$ and $P(MD)$, respectively.

SPO was initiated by applying the sensor layout performance prediction method of Section 4.5 on several randomly selected sensor configurations. The resulting performance measures (Equations (9) through (11)) and multi-objective evaluation measure (Equation (22)) are inputs, $f(x)$, to the Snobfit function (programmed in Matlab[111]). A separate Snobfit optimization was initiated for each of the individual performance measures and multi-objective performance functions. Along with $f(x)$, the coordinates of the corresponding sensor configuration, $x = (S2_x, S2_y, S3_x, S3_y, S4_x, S4_y)$, $\Delta f(x) = 1/500$, the resolution of the classification matrix as discussed in Section 5.3.2, and n_{reg}, the number of suggested evaluation points to be specified by Snobfit (chosen to equal 15 for all Snobfit iterations), are specified. Additionally, in the first function call to Snobfit for a given optimization, the dimensions of the search domain, $[u, v]$, the resolution vector, Δx, and the global-versus-local search weight factor, p, must be specified. For the example application $u = (6.0,\ 6.0,\ 6.0,\ 0.25,\ 0.25,\ 0.25)$ and $v = (11.75,\ 11.75,\ 11.75,\ 6.0,\ 6.0,\ 6.0)$, which confine sensors S2, S3, and S4 to their respective quadrants of the TPS component. $\Delta x = (0.126,\ 0.126,\ 0.126,\ 0.126,\ 0.126,\ 0.126)$, which was required due to the fact that the structural FEM model described in Chapter 2 has a finite fidelity and the temporal structural responses are only available at the FEM model nodes. The points, which Snobfit suggests, are substituted with the nearest neighboring nodal locations. Therefore, in order not to specify the same point (i.e. set of nodal locations) more than once for a finite element mesh of nominal size 0.25 (see Section 3.4) a separation of 0.126 (i.e. just slightly greater than 0.125) is required. In addition, for the example application $p = 0.5$, which proved to be a reasonable balance of the computational effort between global and local searches.

At the end of each iteration (i.e. function call to Snobfit), the algorithm produces 15 suggested sensor configurations for utilization with the subsequent iteration. The damage detection and state classification procedure described in Section 4.5 is performed for the suggested/requested sensor configurations to obtain the corresponding performance measures as objective function evaluations to the next iteration of/call to Snobfit. Again it is noted that the objective functions (i.e. the sensor layout performance measures) can be evaluated at these points and/or other locations since Snobfit is flexible with respect to new information; it simply applies the branch and fit procedure described in Section 6.3 to identify the current optimum, and to suggest additional objective function evaluation points. It is up to the user to decide whether or not to provide Snobfit with the information it suggested/requested, or to supply other new information.

A natural stopping criterion is to stop exploration if for a number of iterations no new x^{best} is generated, and the error corresponding to x^{best} as predicted by Snobfit converges to a reasonably small value. This approach was followed for the example application, where a stopping criterion was heuristically applied.

6.5 SPO Results

The above defined Snobfit sensor placement optimization approach was carried out for the objective functions listed in the first column of Table 37. The first three objective functions are single-objective. The fourth and fifth objective functions are of the form shown in Equation (22), where $\alpha = -0.5$, $\beta = 0.25$, and $\gamma = 0.25$ for the fourth objective function and $\alpha = -0.5$, $\beta = 0.25$, and $\gamma = 5.0$ for the fifth objective function. In addition, the compliment of $P(CD)$, $[1 - P(CD)]$ (i.e. $P(\text{Misdetection})$), is utilized in combination with α as the first term of the fifth objective function to adjust the relative importance of each of the three performance measures to

a ratio of approximately $2:1:1$. This brings the three individual objectives to a comparable scale without impacting the optimal solution (i.e. simply adding/subtracting a constant does not affect the objective function with respect to the design variables). The approximate ratio of relative importance of the three performance measures for the fourth objective function is $360:20:1$. Other ratios of relative importance may be achieved by adjusting α, β, and γ, and via the use of other normalization schemes for standardizing the performance measures.

Table 37. Results: optimal sensor arrays for various objective functions.

Objective Function f(x) =	*Nite*	*Nobj*	Optimal Solution Coordinates for Sensors			*E*	Corresponding Performance Measures		
			S2	S3	S4		P(CD)	P(Type I)	P(Type II)
- P(CD)	71	258	8.75, 6.75	6.0, 3.5	3.5, 0.75	0.0104	0.944	0.13	0.0075
P(Type I)	12	58	7.0, 8.5	11.73, 0.27	5.75, 1.25	0.0426	0.916	0.01	0
P(Type II)	n/a	n/a	7.0, 8.5	11.73, 0.27	5.75, 1.25	n/a	0.916	0.01	0
Function 4	55	268	6.75, 8.75	11.60, 0.40	5.75, 1.25	0.0208	0.932	0.03	0.0025
Function 5	44	196	7.0, 8.5	11.73, 0.27	5.75, 1.25	0.0375	0.916	0.01	0
Function 4 = -0.5 P(CD)+0.25 P(Type I)+0.25 P(Type II)									
Function 5 = 0.5(1 - P(CD))+0.25 P(Type I)+5.0 P(Type II)									

The results corresponding to objective functions 1 through 5 are also shown in Table 37, where *Nite* is the number of Snobfit iterations, *Nobj* is the number of objective function evaluations, and *E* is the measure of accuracy of the quadratic model at the optimal solution as estimated by Snobfit (i.e. $E = \max(|f(x) - q(x)|)$, where the maximum is taken over the best point and its $n+5$ nearest neighbors and $q(x)$ is the quadratic model). The coordinates given are with respect to the bottom left corner of the plate in Figure 1b. The results are visually presented in Figure 44.

From Table 37 and Figure 44 it can be concluded that although the solution varies for different objective functions, the optimal sensor arrays corresponding to objective functions 2 through 5

are virtually identical. Additionally, it was observed during the Snobfit iterations that the optimal solutions to objective functions 2 through 5 was robust and insensitive to small changes in the independent variables (i.e. shifting sensors S2, S3, and/or S4 by less than 0.25 inches in any direction, did not significantly alter the performance measures). However, the solution with respect to the first objective function, $f(x) = -P(CD)$, was very sensitive to small changes in the independent variables (i.e. shifting sensors S2, S3, and/or S4 by less than 0.25 inches in any direction, significantly degraded the performance measures).

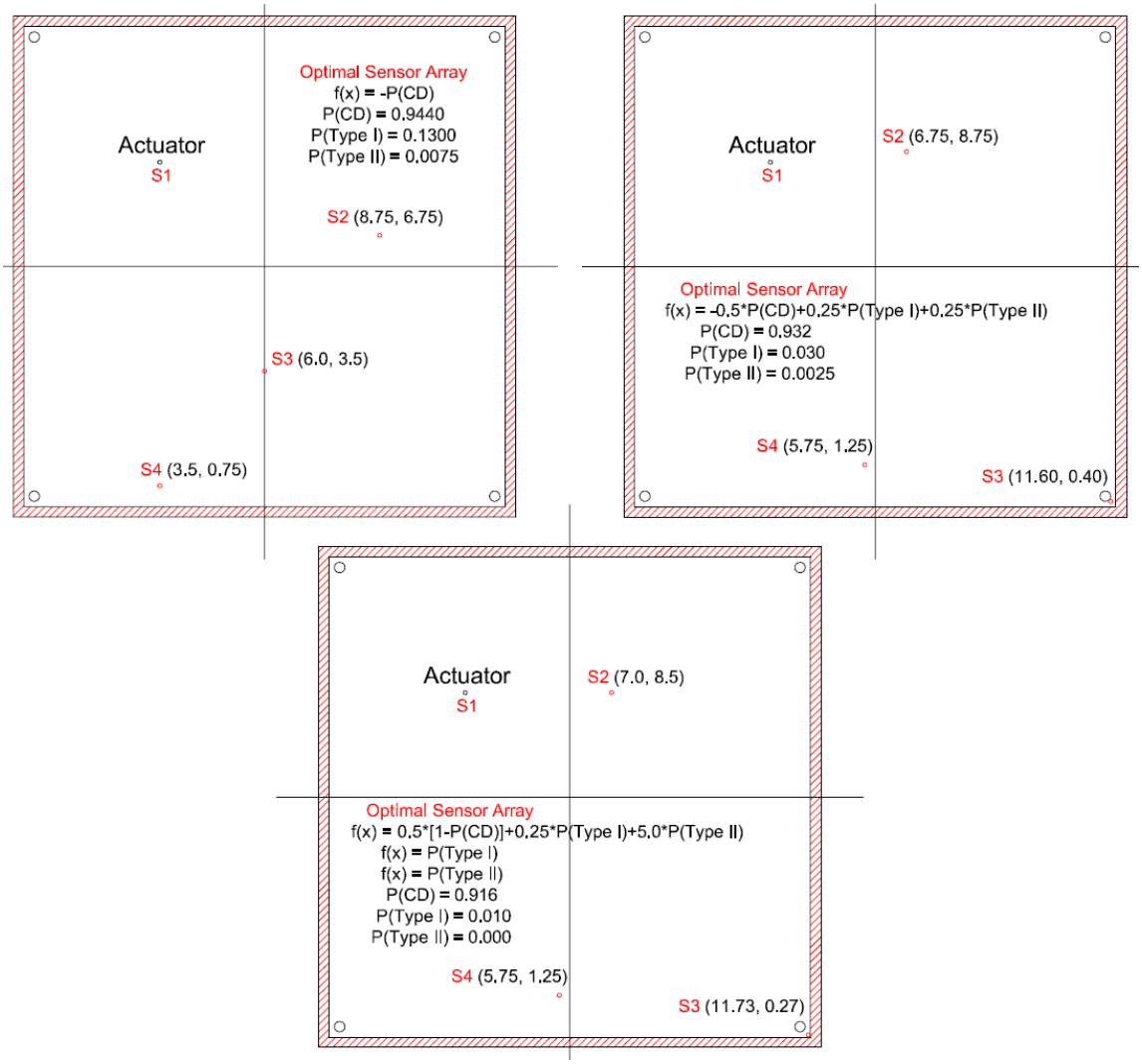

Figure 44. Optimal sensor arrays corresponding to different objective functions.

Difficulties were observed while optimizing the third objective function, $f(x) = -P(TypeII)$. Several sensor configurations produced probabilities of missed detection of zero percent, creating many global optimal solutions, since a probability of missed detection less than zero percent is not possible. Using the additional information gathered during the optimization of objective functions 2, 4, and 5, it appears that $(S2_x, S2_y, S3_x, S3_y, S4_x, S4_y) = (7.0, 8.5, 11.73, 0.27, 5.75, 1.25)$ is also the optimal solution for the third objective function.

Chapter 6 utilized the sensor layout performance prediction methodology of Chapter 4 in combination with Snobfit to optimize the probabilistic performance measures (Section 4.3) and multi-objective evaluation functions thereof (Equation (22)). The variability analysis of the performance measures with respect to sensor location showed the presence of significant noise as well as significantly differing inferences with respect to optimum locations depending on which performance measure was utilized. The SPO methodology revealed one particular solution that appeared to optimize most of the objective functions considered.

CHAPTER VII

SENSOR SENSITIVITY, RELIABILITY, REDUNDANCY

Sensor sensitivity with respect to changes in the environment and sensor reliability in general are key issues that must be considered. This chapter addresses concerns related to research objective 5. There are upper and lower thresholds of temperature and moisture where even state of the art sensors begin to record measurements improperly due to nonlinearity or stop working altogether. Additionally, the sensitivity of the data analysis methods with regard to small changes in the structural response due to environmental variability must be taken into account. For example, if the structural state has not changed, but an increase in temperature is observed that ultimately causes the response of the structure or the response as recorded by the sensor to change, the data analysis method and signal processing algorithm must be insensitive to that variability and still classify the structure into the correct structural state as identified prior. Another issue that needs to be addressed is sensor redundancy. In order to have a reliable and robust system, there needs to be redundancy.

Ongoing research at Wright Patterson Air Force Base[66,67,68] has attempted to characterize the performance of piezoelectric wafers utilized as actuators as well as sensors, with respect to operability, durability, and survivability under widely varying environmental conditions. Surface-bonded piezoelectric sensors were studied under accelerated exposure conditions typically found in operational aircraft environments. From these experiments, evidence of both gradual and abrupt sensor performance degradation was observed. Blackshire, et al,[112] constructed models to understand and explain the aforementioned degradation due to undesired

load transfer processes between the aircraft and the sensor. Critical material parameters related to bond and piezoelectric material types were identified. [112] In addition, a quantitative evaluation of the degradation due to temperature cycling was investigated.[67] A general reduction and quadratic trend in out-of-plane displacement energy levels from approximately 36 nm peak displacement for 0 freeze-thaw cycles, to about 20 nm of displacement after 40 repeated freeze-thaw exposures is observed. This represents approximately 1.8% reduction in vibration level for each consecutive freeze-thaw cycle, with an apparent leveling-off at about 20 nm peak displacement after approximately 35 cycles. An elevated temperature exposure cycling experiment was also considered, where a reduction and quadratic trend in performance with additional heat exposures was found. A leveling-off in performance reduction from roughly 35 nm to about 17 nm peak vibration amplitude was observed after approximately 20 heat cycles. This represents a reduction in vibration level for each consecutive heat cycle of approximately 4.7%. Accelerated electrochemical exposure did not seem to affect the sensor performance.[67] Considering the aforementioned observed sensor characteristics, it is necessary that damage detection classifiers be taught and calibrated using data obtained from sensors, which have experienced adequate numbers of freeze-thaw and elevated temperature cycles. Significant reductions in detection performance of any sensor configuration should otherwise be expected after just a short time of operation, since the signals that will be recorded after several freeze-thaw and elevated temperature cycles will certainly be different (even if only in magnitude leading to a decreased signal to noise ratio) than those signals that were utilized to teach the damage detection/state classification algorithm. It should be noted that the sensor performance degradation does not affect or influence sensor placement optimization (SPO), due to the fact that the aforementioned sensor degradation is independent of sensor location. All locations on a

TPS component of approximate size 12 inches x 12 inches are assumed to experience equal number of freeze-thaw and elevated temperature cycles, justifying the previous statement.

Additionally of interest is the detection of cracked and disbonded piezoelectric sensors and actuators. Blackshire, et al,[66] utilized a novel displacement-field imaging approach to understand the vibration characteristics of "piezo wafer active sensor" (PWAS). Crack and disbonding events were identified with relative ease and a high degree of precision and resolution. Disbonding of PWAS shows lobe intensified regions, where the disbonded actuator is permitted to vibrate at its own natural frequency. In addition, the displacement-field imaging technique intensifies the out-of-plane displacement of the sensor caused by cracks and other sharp, free-boundary anomalies, making their detection quite easy.[67] This allows for nondestructive testing of the sensor system prior to operation of the SHM system, as well as during general maintenance of the aircraft and its subsystems.

In addition, while there are several studies[113,114,115] that attempt to identify the performance of a piezoelectric sensor/actuator with a known level of disbond, only a limited number of studies investigated how to assess unknown bond quality online.[116,117,118] The proposed methods utilize small shifts in the natural frequency of the piezoelectric sensor/actuator to identify the amount of disbond present. However, the issue associated with how to differentiate the "sensed" frequency shift caused by structural damage from that of sensor/actuator disbonding are only addressed by Park, et al,[119] who proposes an efficient sensor self-diagnostic procedure for SHM processes, based on tracking the changes in the imaginary part of the electrical admittance of piezoelectric sensors/actuators. The degradation of a sensor/actuator (either cracks or disbonding) produces distinct changes in its measured admittance. Park, et al,[119] showed that the slope of the imaginary part of a sensor/actuator's admittance is not sensitive to structural damage, while it is

sensitive to cracking (downward shift in slope) and disbonding (upward shift in slope). Park, et al,[119] noted that the method is only efficient at lower frequency ranges (i.e. up to several kHz) and that the method is sensitive enough (at those lower frequencies) to detect cracking and disbonding sensor/actuator damage on piezoelectric patches that were still able to produce sufficient sensing and actuation capabilities.

The above leads to the following approach: since the self-diagnostic procedure proposed by Park, et al,[119] identifies even low level sensor/actuator damage, the onset of a malfunctioning sensor/actuator can easily be determined. Therefore, the errors in the measured signal of a sensor, due to the onset of cracking or disbonding, which traditionally lead to bias and trend characteristics in the measured signal, may be addressed. A normalization procedure, such as the one employed by DeSimio, et al,[120] is appropriate. Additionally, it is possible to detrend the measured signal (removing trend) and to center the mean on zero (removing bias) prior to its utilization within an SHM process. The amount of trend and bias removed from the signal might indicate the level of sensor/actuator malfunction. No analytical or experimental research work has been done to verify this hypothesis and further investigation is needed.

The issues discussed in the previous paragraphs cover sensor/actuator performance degradation; however, they do not encompass the robustness (with respect to environmental variability) of the SHM/damage detection/signal processing methods employed to classify the structure into its corresponding structural states. Olson, et al,[121] have developed a method to normalize the frequency scale of the measured data as a function of temperature. This method is based on analytical and experimental modal analyses across a given range of temperatures. This compensation process accounts for environmental variability with respect to temperature. Similarly, a normalization method to compensate for moisture/humidity variability may be

developed. These additional signal processing schemes can account for the stochastic nature of environmental parameters such as temperature and humidity (or similar) and add robustness to SHM.

The following scheme may be explored to add redundancy to the SHM system with respect to sensors/actuators. An additional sensor is placed on the structure such that it optimally monitors the response of the remaining sensors/actuators. After teaching this additional sensor the expected measured response of each of the remaining sensors, its response may be used by a prediction model to estimate the response of the remaining sensors/actuator. Any discrepancies between the model predictions and true sensor measurements and actuation input may then be linked with structural damage and actuator malfunction, respectively. A minimum/maximum threshold approach may be implemented, such that when the difference between model prediction and true sensor measurement reaches/surpasses a specified value/threshold, damage is declared. This approach can be generalized by constructing a prediction model for each of the applied sensors (i.e. each sensor keeps the remaining sensors in check). Prediction models may consist of simple autoregressive processes or consider complex time series models for spectral density.[80] Simple models require less training, while more complex models are needed to predict sophisticated signals.

The above procedures, methods, and processes encompass sensor sensitivity, reliability, and add robustness to SHM with respect to sensing capabilities. Additional research is required to implement these concepts within the proposed SPO for SHM under uncertainty methodology.

CHAPTER VIII

SUMMARY, CONCLUSIONS, AND FUTURE WORK

This research developed a methodology for the probabilistic analysis and optimization of structural health monitoring (SHM) systems for hot aerospace structures such as next generation flight vehicles known as space operations vehicles (SOV's). Specifically, the study focused on the sensor placement optimization (SPO) under uncertainty for the SHM system of a thermal protection system (TPS) component. In concept, the fuselage of an SOV would be protected by a TPS consisting of mechanically attached panels made from heat resistant materials such as carbon-carbon composites. A simple prototype test article consisting of a 12 inch square aluminum plate fastened via four 0.25 inch bolts to an optical table was considered as an example application to help develop the design methodology, which included the uncertainties of design inputs such as thermal and mechanical loads, and geometric and material properties.

An effective design optimization approach has been proposed via a methodology that integrates advances in various individual disciplines to strive for an optimum design of SHM sensor layouts under uncertainty. The proposed method includes the following steps: (1) structural simulation, (2) probabilistic analyses, (3) damage detection, and (4) sensor placement optimization (SPO). For most realistic structures, the response due to various loads cannot be determined via a closed-form function of the input variables, but must be computed through numerical procedures such as a finite element method (FEM). The probabilistic FEM analysis of analytical models incorporates uncertainty via the utilization of discretized random fields and processes as model input parameters to generate stochastic finite element models (SFEM). From a stochastic FEM

analysis the statistics of model outputs such as stresses, strains, and deformations are known and a damage detection method is applied to numerous realizations of the SFEM output to construct a classification matrix and estimate probabilistic performance measures such as the likelihood of correctly identifying the structural state of a component for a given sensor layout. SPO then identifies the sensor configuration for which the performance measures are optimized. Multi-objective optimization formulations are of particular interest. Figure 45 graphically summarizes the proposed SPO under uncertainty for SHM systems methodology.

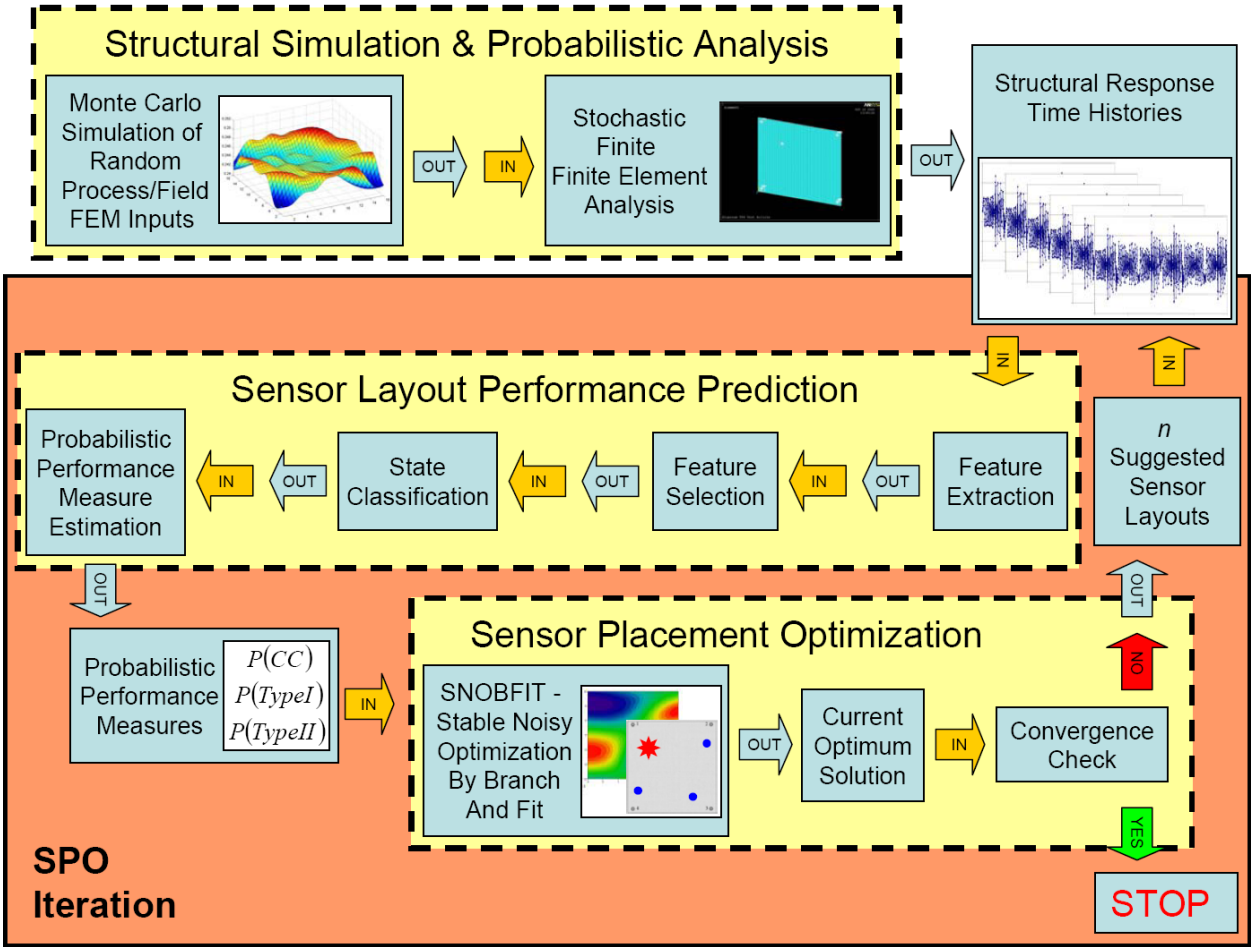

Figure 45. Graphical presentation of SPO under uncertainty for SHM systems methodology.

In addition to the SPO under uncertainty methodology for SHM systems, this study addressed model and methodology validation. A hierarchical validation assessment was introduced and applied to individual components of the SPO for SHM under uncertainty methodology. Section 8.1 of this chapter summarizes general insights gathered during the development of the proposed methodology and the conclusions of this dissertation. Section 8.2 discusses possible future work and research topics.

8.1 Conclusions

During the development and implementation of the SPO for SHM under uncertainty methodology on the example application, valuable insights are gained. Generally the methodology is very computationally intense, rendering it currently infeasible for realistic design applications. Computational expense is mainly derived from analytical modeling of the SFEM, but can also be attributed to the signal processing required to estimate the probabilistic performance measures. Due to the high excitation frequency of the input function required for active SHM, the time step of transient dynamic analyses is reduced to near zero values. Mode superposition (MSP) transient analysis may aid in reducing the degrees of freedom of the analytical simulation, thereby reducing the computational time required per time step; however, MSP does not reduce the total number of time steps of the transient analysis. Additionally, realistic structures are likely to require an active SHM excitation input with frequency content at least one magnitude greater than is used in the example application of this study, compounding the problem of excessive computational requirements of analytical analyses.

Computational expense associated with the sensor layout performance prediction methodology is also significant. Due to the large amount of data generated during the probabilistic FEM

analysis, which yields a strain on data storage requirements in itself, damage detection methods used to predict the probabilistic performance measures of a given sensor array are burdened with significant amounts of signal processing. A major portion of the approximately 12 minutes it takes to estimate the probabilistic performance measures corresponding to a given sensor configuration of the example test article is utilized for I/O operations. Accessing the hard drive, which contains approximately 90GB of FEM output, and reading/loading the necessary data files corresponding to a given sensor layout, is most time consuming. Although technology is advancing rapidly and faster computing machines will be available in the future, it may not offset the computational effort required to manage the additional FEM output that will be generated by more complex models, which are inevitably needed for the simulation of realistic TPS components.

Also, a significant signal processing time is necessary to perform the state classification of the 500 realizations of the model responses (100 per structural state). The application of this methodology to more realistic structures would certainly include more damage states than the test article application (four damage states, each corresponding to a loose bolt condition of 25% nominal torque) and would therefore require more FEM simulations/analyses. Also, 100 realizations of the SFEM outputs per structural state may not be sufficient for applications where several 10's of structural states must be identified and the featurs space is more complex (higher dimensions). An additional burden that came to light during the implementation of the SPO under uncertainty methodology via Snobfit is the transformation of a continuous optimization problem (Equation (24)) into one that considers discrete design variables. Due to the finite fidelity of the FEM model, the structural response is readily available only at discrete locations – namely the nodal locations of the FEM model. Therefore, when Snobfit requests the evaluation

of the objective function at a location that does not correspond to a nodal location of the FEM mesh, the nearest neighboring node is instead substituted; the discretization of the search domain is inevitable. The trivial solution of utilizing an infinitely fine FEM mesh is infeasible due to the issues discussed above. Design variable fidelity and computational expense must be objectively evaluated. All of these requirements associated with the application of the proposed methodology on realistic design problems compound the computational expense currently rendering it infeasible for practical application.

Additional insight was gathered with respect to model and methodology validation. Assessing the accuracy of analytical models and prediction methodologies is complex and highly dependent on the subsequent utilization of the model and/or prediction methodology. Hierarchical utilization of models and prediction methodologies brings an additional degree of difficulty by compounding modeling errors and input uncertainties. This topic is addressed graphically in Figure 28 and Figure 29 in Chapter 5. In general it can be concluded that small allowable differences between prediction and observation at a low level within a hierarchical methodology can produce unacceptably large discrepancies between prediction and observation at higher levels. What may seem an allowable difference at the finite element analysis level, can yield undesirable results at the sensor layout performance prediction level. The sensitivity of each component's output with respect to the uncertainty of the inputs and its effects on subsequent utilization are currently not well defined; however, their significance with respect to accuracy has been established within this study.

8.2 Future Work

Future related research work needs to investigate computationally efficient methods to implement the SPO under uncertainty methodology for SHM. In addition, an investigation into model validation and the degree of accuracy required for FEM models and sensor layout performance prediction methodologies to be of use in subsequent employment is necessary.

Future implementations of the methodology should investigate efficient analytical modeling techniques, such as the utilization of boundary element models[122] and surrogate modeling. Efficient structuring and perhaps compression of the model outputs may yield an additional computational saving, which may have been sacrificed in this study. More efficient data organization and storage may also yield more effective I/O utilization and cut down the signal processing time to estimate the probabilistic performance measures, a large part of which was consumed by I/O processes in the test article implementation of this study. Reducing the computational effort of estimating the performance measures for a given sensor configuration will also add to the efficiency of SPO, making a more thorough search of the design variable domain feasible.

Future work should also investigate the significance of the degree to which the finite element model was validated and to what level small discrepancies between finite element and experimental modal analysis compound to yield large discrepancies between the results of subsequent applications of the FEM model and corresponding experimental observations. This may require a stricter validation assessment of the SFEM, as well as an evaluation of the components of the sensor layout performance prediction methodology. Additional validation assessments might be required between each of the components shown in Figure 29. Future research should also consider the tradeoffs between the number of steps of a methodology that

are validated (i.e. time and effort required) versus the accuracy of the final methodology results (i.e. discrepancies between prediction and reality).

Future research topics also need to include the investigation of methods to account for the degradation and variability of the system over extended periods of time and their appropriate inclusion into the methodology. Other future related research work might include the investigation of a more complex/realistic structural test article. A structure that might be considered in future research is a more convincing prototype component of a thermal protection system (TPS) and consists of a carbon-carbon heat resistant panel that is attached to a titanium backing structure (which simulates the structural frame of a flight vehicle) via 15 silicon carbon-carbon brackets and 45 bolts (three bolts per bracket). An experimental setup of this TPS component already exists at AFRL in Dayton, Ohio, and is shown in Figure 46. It is currently undergoing testing.[9] In Figure 46, bracket locations 1 through 15 are shown dark gray, while sensor locations 1 through 4 are shown yellow.

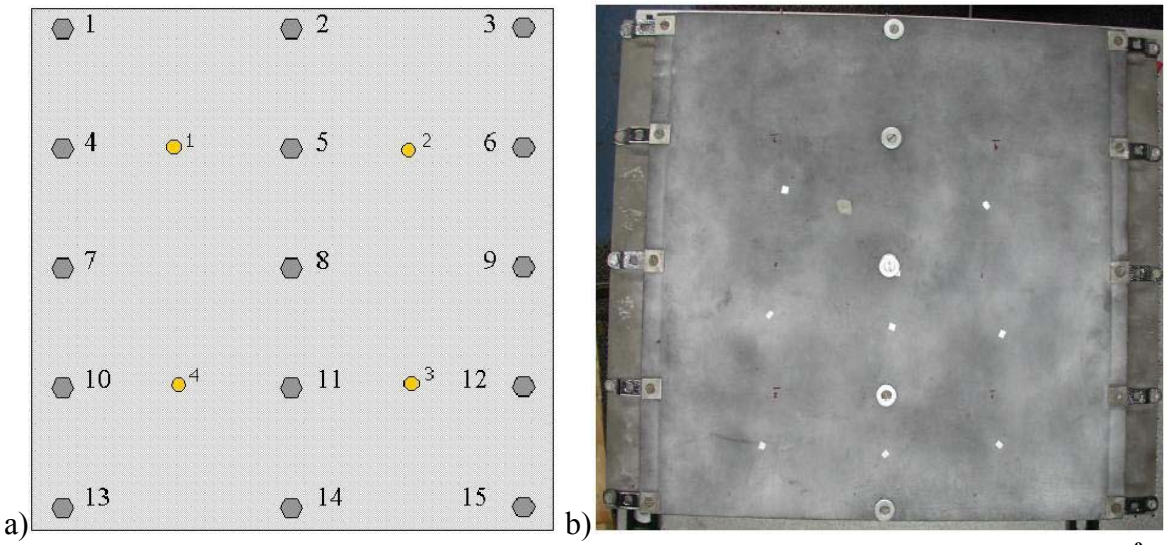

Figure 46. Laboratory setup of realistic TPS panel and sensor layout. a) schematic; b) photograph[9].

A portion of the already existing FEM model is shown in Figure 47. The FEM model is constructed in Ansys and consists of approximately 54,000 Shell-43 (carbon-carbon panel) and Shell-63 (steel backing structure) 4-noded shell elements. The analysis is transient and includes a dynamic mechanical load consisting of a sinusoidal swept frequency deformation, exciting the structure from 0 to 7,000 Hz in approximately 3.0 seconds. This is identical to the excitation used in the laboratory at WPAFB. Internal stresses due to transient temperature differentials within the TPS plate are included in the FEM analysis.

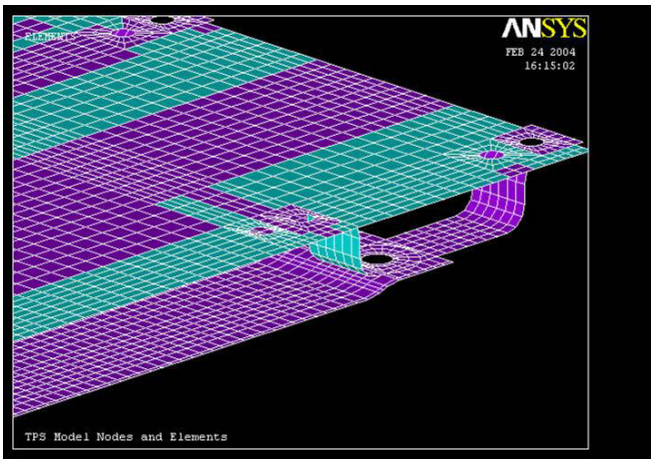

Figure 47. Realistic TPS component model.

Other aspects of the structural modeling and analyses that require future investigation and research are the methods used to model the connections between the TPS plate and brackets, as well as between the brackets and the steel backing structure. Methods under consideration are nodal equivalencing and the insertion of massless and dimensionless springs in combination with contact elements. This test article is much more comprehensive and complex in the sense that it considers a structure that has stiffening ribs, attachment brackets, and is manufactured from composite materials. A backing structure that simulates the structural frame of the flight vehicle

is also included in the test setup and FEM models. Damage detection of this TPS component considers a 16 state classification problem (15 brackets where damage can occur and the healthy condition), rather than the five state classification problem considered in this research. Also the excitation frequency for this component is much higher. All these issues drive up the computational expense and a way to deal with these issues must first be identified before attempts to implement this methodology on such a testing structure are initiated.

REFERENCES

[1] Shkarayev, S., Krashantisa, R., and A. Tessler, "An Inverse Interpolation Method Utilizing In-Flight Strain Measurements for Determining Loads and Structural Response of Aerospace Vehicles." in proceedings of 3rd International Workshop on Structural Health Monitoring, Stanford, CA, September 12-14, 2001.

[2] Brown, T., Wood, K., Childers, B., Cano, R., Jensen, B., and R. Rogowski, "Fiber Optic Sensors for Health Monitoring of Morphing Aircraft." in proceedings of SPIE 6th Annual International Symposium on Smart Structures and Materials, Newport Beach, CA, March 1-5, 1999.

[3] Adams, D.E., "Diagnostics & Prognostics in Structural Systems." short course at Wright Patterson Air Force Base, Dayton, OH, August 9-11, 2004.

[4] Cruse, T., "Conference Keynote: Integrated System Health Management." in a speech at Air Force Research Laboratory Integrated Systems Health Management Conference, Dayton, OH, August 17-19, 2004.

[5] Woodard, S.E., Foffey, N.C., Gonzalez, G.A., Woodman, K.L., Weathered, B.W., Rollins, C.H., Taylor, B.D., and R.R. Brett, "Development and Flight Testing of an Adaptable Vehicle Health Monitoring Architecture." NASA TM-2003-212139, January 2003.

[6] Ansys. ANSYS Release 9.0 Documentation. ANSYS, Inc., 2004.

[7] Doebling, S.W., Farrar, C.R., Prime, M.B., and D.W. Shevitz, *Damage Identification and Health Monitoring of Structures and Mechanical Systems from Changes in Their Vibration Characteristics: A Literature Review.* Los Alamos National Laboratory, Los Alamos, NM, 1996.

[8] Duda, R.O., Hart, P.E., and D.G. Stork, *Pattern Classification*. 2nd Edition, John Wiley & Sons, Inc., New York, 2001.

[9] DeSimio, M., Miller, I., Derriso, M., Brown, K., and M. Baker, "Structural Health Monitoring Experiments with a Canonical Element of an Aerospace Vehicle." in proceedings of 2003 IEEE Aerospace Conference, Big Sky, MT, March 8-15, 2003.

[10] Huyer W., and A. Neumaier, "SNOBFIT – Stable Noisy Optimization by Branch and Fit." submitted for review to *ACM Transactions on Mathematical Software*, online at http://www.mat.univie.ac.at/~neum/software/snobfit/, accessed on May 25, 2004.

[11] Olson, S., DeSimio, M., and M. Derriso, "Fastener Damage Estimation in a Square Aluminum Plate." submitted for review to *Structural Health Monitoring Journal*, May 13, 2005.

[12] Rosenstengel, J., I. Miller, M. DeSimio, M. Derriso, K. Brown, W. Braisted, and S. Olson, "Detection of Fastener Failure in a Thermal Protection System Panel." in proceedings of 2004 IEEE Aerospace Conference, Big Sky, MT, March 6-13, 2004.

[13] Derriso, M., S. Olson, W. Braisted, M. DeSimio, J. Rosenstengel, and K. Brown, "Detection of Fastener Failure in a Thermal Protection System." in proceedings of SPIE 11th Annual International Symposium on Smart Structures and Materials, San Diego, CA, March 14-18, 2004.

[14] Derriso, M., S. Olson, W. Braisted, M. DeSimio, J. Rosenstengel, and K. Brown, "Structural Health Monitoring to Detect Fastener Failure." in proceedings of 2004 International Conference on Computational & Experimental Engineering & Sciences, Madeira, Portugal, July 26-29, 2004.

[15] Olson, S.E., "Structural Health Monitoring of Thermal Protection Systems." in proceedings of Air Force Research Laboratory Integrated Systems Health Management Conference, Dayton, OH, August 17-19, 2004.

[16] Derriso, M., S. Olson, M. DeSimio, and B. Sanders, "Development of Automated Damage Detection Techniques." in proceedings of Materials, Science, and Technology 2004 Conference, New Orleans, LA, September 23-26, 2004.

[17] MSC.Software, *MSC.Nastran*. MSC.Software Corporation, Santa Ana, CA, 2001.

[18] MSC.Software, *MSC.Dytran*. MSC.Software Corporation, Santa Ana, CA, 2002.

[19] Abaqus. ABAQUS/Standard Version 6.5. ABAQUS, Inc., 2006.

[20] Dhondt, G., and K. Wittig, *CalculiX Version 1.4*, online at http://www.calculix.de, accessed on May 1, 1998.

[21] Forssell, J. *Imapct*. GNU General Public License, 2002.

[22] Haldar, A., and S. Mahadevan, *Reliability Assessment Using Stochastic Finite Element Analysis.* John Wiley & Sons, Inc., New York, 2000.

[23] Ghanem, R., and P. Spanos, *Stochastic Finite Elements: a Spectral Approach*. Springer, New York, 1991.

[24] Mahadevan, S., and R. Rebba, "Simulation of Stochastic Processes: A Review Paper." Technical Report, Department of Civil and Environmental Engineering, Vanderbilt University, Nashville, TN, 2003.

[25] Huang, S., "Simulation of Random Processes Using Karhunen-Loeve Expansion." Ph.D. dissertation, The National University of Singapore, Singapore, 2001.

[26] Einstein, A., "On the Movement of Small Particles Suspended in a Stationary Liquid Demanded by the Molecular Kinetic Theory of Heat." *Annalen der Physik*, Vol. 17, pp. 549-66, 1905.

[27] Rice, S.O., "Mathematical Analysis of Random Noise." *Selected Papers on Noise and Stochastic Processes*, (Edited by Nelson Wax), Dover, pp. 133-294, 1954. (paper originally appeared in two parts in *Bell System Technical Journal*, Vol. 23, July, 1944, and Vol. 24, January, 1945.)

[28] Shinozuka, M., "Monte Carlo Solution of Structural Dynamics." *Computers and Structures*, Vol. 2, No. 5, 6, pp. 855-74, 1972.

[29] Shinozuka, M., and C-M. Jan, "Digital Simulation of Random Processes and its Applications." *Journal of Sound and Vibration*, Vol. 25, No. 1, pp. 111-28, 1972.

[30] Yang, J.-N., "Simulation of Random Envelope Processes." *Journal of Sound and Vibration*, Vol. 25, No. 1, pp. 73-85, 1972.

[31] Yang, J.-N., "On the Normality and Accuracy of Simulated Random Processes." *Journal of Sound and Vibration*, Vol. 26, No. 3, pp. 417-28, 1973.

[32] Shinozuka, M., "Digital Simulation of Random Processes in Engineering Mechanics with the Aid of FFT Technique." *Stochastic Problems in Mechanics*, (Edited by S.T. Ariaratnam and H.H.E. Leipholz), University of Waterloo Press, Waterloo, pp. 277-286, 1974.

[33] Deodatis, G., and M. Shinozuka, "Simulation of Seismic Ground Motion Using Stochastic Waves." *Journal of Engineering Mechanics*, ASCE, Vol. 115, No. 12, pp. 2723-37, 1989.

[34] Yamazaki, F., Shinozuka, M., and G. Dasgupta, "Neumann Expansion for Stochastic FEM Analysis." *Journal of Engineering Mechanics*, ASCE, Vol. 114, No. 8, pp. 1135-354, 1988.

[35] Yamazaki, F., and M. Shinozuka, "Simulation of Stochastic Fields by Statistical Preconditioning." *Journal of Engineering Mechanics*, ASCE, Vol. 116, No. 2, pp. 268-87, 1990.

[36] Shinozuka, M., "Stochastic Fields and Their Digital Simulation." *Stochastic Methods in Structural Dynamics*, (Edited by G.I. Schueller and M. Shinozuka), Martinus Nijhoff Publishers, Dordecht, pp. 93-133, 1987.

[37] Shinozuka, M., and G. Deodatis, "Stochastic Process Models for Earthquake Ground Motion." *Journal of Probabilistic Engineering Mechanics*, Vol. 3, No. 3, pp. 114-23, 1988.

[38] Tedesco, J.W., McDougal, W.G., and C.A. Ross, *Structural Dynamics: Theory and Application.* Addison Wesley Longman, Inc., Menlo Park, CA, 1999.

[39] Sakamoto, S., and R. Ghanem, "Polynomial Chaos Decomposition for the Simulation of Non-Gaussian Nonstationary Stochastic Processes." *Journal of Engineering Mechanics,* Vol. 128, No. 2, pp. 190-201, February 2002.

[40] Deodatis, G., and R.C. Micaletti, "Simulation of Highly Skewed Non-Gaussian Stochastic Processes." *Journal of Engineering Mechanics,* Vol. 127, No. 12, pp. 1284-95, December 2001.

[41] Shinozuka, M., and G. Deodatis, "Simulation of stochastic processes by spectral representation." *Applied Mechanics Review*, Vol. 44, No. 4, pp. 191-204, 1991.

[42] VanMarcke, E., *Random Fields: Analysis and Synthesis*. The MIT Press, Cambridge, 1983.

[43] The Royal Aeronautical Society, *Material Properties Handbook: Volume I Aluminum Alloys*. North Atlantic Treaty Organization Advisory Group for Aerospace Research and Development, London, with Amendments from 1959 and 1966.

[44] Rebba, R., and S. Mahadevan, "Probabilistic Assessment of CAE Models." in proceedings of SAE World Congress, Detroit, MI, April 3-6, 2006.

[45] Coleman, H.W., and F. Stern, "Uncertainties in CFD Code Validation." *ASME Journal of Fluids Engineering*, Vol. 119, pp. 795-803, 1997.

[46] Hills, R.G., and T.G. Trucano, "Statistical Validation of Engineering and Scientific Models with Applications to CTH." Sandia Technical Report, SAND2001-0312, Sandia National Laboratories, Albuquerque, NM, 2001.

[47] Urbina, A., Paez, T.L., Hasselman, T.K., Wathugala, G.W., and K. Yap, "Assessment of Model Accuracy Relative to Stochastic System Behavior." in proceedings of 44th AIAA Structures, Structural Dynamics, Materials Conference, Norfolk, VA, April 7-10, 2003.

[48] Ewins, D.J., *Modal Testing: Theory, Practice and Application*. 2nd Ed., Research Studies Press LTD., Philadelphia, PA, 2000.

[49] Zhang, R., and S. Mahadevan, "Bayesian Methodology for Reliability Model Acceptance." *Reliability Engineering and System Safety*, Vol. 80, No. 1, pp. 95-103, 2003.

[50] Higdon, D., Kennedy, M.C., Cavendish, J., Cafeo, J., and R.D. Ryne, "Combining Field Data and Computer Simulations for Calibration and Prediction." *SIAM Journal on Scientific Computing*, Vol. 26, pp. 448-66, 2004.

[51] Rebba, R., Mahadevan, S., and S. Huang, "Validation and Error Estimation of Computational Models." in proceedings of 4th International Conference on Sensitivity Analysis of Model Output, Santa Fe, NM, March 8-11, 2004.

[52] McFarland, J., and S. Mahadevan, "Model Validation Metrics for the New Thermal Challenge Problem." Technical Report submitted to Sandia National Labs, Albuquerque, NM, May 2006.

[53] Srivastava, M., *Methods of Multivariate Statistics*. John Wiley & Sons, Inc., New York, 2002.

[54] Gelman, A., *Bayesian Data Analysis*. Chapman and Hall/CRC, Boca Raton, FL, 2004.

[55] Mahadevan, S., and R. Rebba, "Validation of Reliability Computational Models using Bayes Networks." *Reliability Engineering and System Safety*, Vol. 87, No. 2, pp. 223-32, 2005.

[56] Schwarz, B.J., and M.H. Richardson, "Experimental Modal Analysis." in proceedings of CSI Reliability Week, Orlando, FL, October, 1999.

[57] Rajakumar, C. and C.R. Rogers, "The Lanczos Algorithm Applied to Unsymmetric Generalized Eigenvalue Problems." *International Journal for Numercial Method in Engineering*, Vol. 32, pp. 1009-26, 1991.

[58] Richards, S.A., "Completed Richardson Extrapolation in Space and Time." *Communications in Numerical Methods in Engineering*, Vol. 13, pp. 558-73, 1997.

[59] Mahadevan, S., and R. Rebba, "Inclusion of Model Error in Reliability-Based Optimization." *Transactions of the ASME*, Vol. 128, pp. 936-44, 2006.

[60] Efron, B., and R. Tibshirani, *An Introduction to Bootstrap*. Chapman & Hall, New York, 1993.

[61] Blevins, R.D., *Formulas for Natural Frequency and Mode Shape*. Van Nostrand Reinhold Company, New York, 1979.

[62] Leissa, A.W., "Vibration of Plates." NASA SP-160, Scientific and Technical Information Division, NASA, Washington, D.C., 1969.

[63] Wood, K.H., Brown, T.L., Wu, M.C., and C.B. Gause, "Fiber Optic Sensors for Cure/Health Monitoring of Composite Materials." in proceeding of 3rd International Workshop on Structural Health Monitoring, Stanford, CA, September 12-14, 2001.

[64] Prosser, W.H., Brown, T.L., Woodard, S.E., Fleming, G.A., and E.G. Cooper, "Sensor Technology for Integrated Vehicle Health Management of Aerospace Vehicles." in proceedings of 29th Annual Review of Progress in Quantitative Nondestructive Evaluation, Bellingham, WA, July 14-19, 2002.

[65] Forth, S.C., and A. Staroselsky, "Fracture Evaluation of In-Situ Sensors for High Temperature Applications." in proceedings of 10th International Congress of Fracture, Honolulu, HI, December 2-6, 2001.

[66] Blackshire, J.L., Giurgiutiu, V., Cooney, A., and J. Doane, "Characterization of Sensor Performance and Durability for Structural Health Monitoring Systems." in proceedings of SPIE 12th International Symposium on Smart Structures and Materials, San Diego, CA., March 2005.

[67] Blackshire, J.L., and A. Cooney, "Characterization of Bonded Piezoelectric Sensor Performance and Durability in Simulated Aircraft Environments." in proceedings of 32nd Review of Progress in Quantitative NDE, Brunswick, ME, 2005.

[68] Blackshire, J.L., and A. Cooney, "Evaluation and Improvement in Sensor Performance and Durability for Structural Health Monitoring Systems." in proceedings of SPIE's 13th International Symposium on Smart Structures and Materials, San Diego, CA., March 2006.

[69] Piezocryst Advanced Sensorics GmbH, "Basics: Piezoelectric Sensors." online at http://www.piezocryst.com, accessed on August 24, 2006.

[70] Corbin, M., Hera, A., and Z. Hou, "Location Damage Regions Using Wavelet Approach." online at http://wusceel.cive.wustl.edu/asce.shm/pdfs/corbin_hera_hou.pdf, accessed on October 29, 2003.

[71] Au, S.K., Yuen, K.V., and J.L. Beck, "Two-Stage System Identification Results for Benchmark Structure." online at http://wusceel.cive.wustl.edu/asce.shm/pdfs/au_yuen_beck.pdf, accessed on October 29, 2003.

[72] Banks, H.T., Joyner, M.L., Bincheski, B., and W.P. Winfree, "Real time computational algorithms for eddy-current-based damage detection." *Institute of Physics Publishing*, Vol. 18, pp. 795-823, 2002.

[73] Lew, J.S., and J.N. Juang, "Structural Damage Detection Using Virtual Passive Controllers." NASA/TM-2001-211251, December 2001.

[74] Kohavi, R. and F. Provost, "Glossary of Terms." *Machine Learning*, Vol. 30, No. 2/3, pp. 271-74, 1998.

[75] Therrien, C.W., *Decision Estimation and Classification: An Introduction to Pattern Recognition and Related Topics*. John Wiley & Sons, New York, 1989.

[76] Farrar, C. and H. Sohn, "Pattern Recognition for Structural Health Monitoring." in proceedings of Workshop on Mitigation of Earthquake Disaster by Advanced Technologies, Las Vegas, NV, November 30-December 1, 2000.

[77] Sammon, J.W., "A nonlinear Mapping Algorithm for Data Structure Analysis." *IEEE Transactions on Computers*, Vol. C-18, No. 5, pp. 401-9, May 1969.

[78] Koontz, W.L.G., and K. Fukunaga, "A Nonlinear Feature Extraction Algorithm Using Distance Transformation." *IEEE Transactions on Computers*, Vol. C-21, No. 1, pp. 56-63, January 1972.

[79] Nigam, N.C., *Introduction to Random Vibrations*. MIT Press, Cambridge, MA, 1983.

[80] Shiavi, R., *Introduction to Applied Statistical Signal Analysis*. Academic Press, San Diego, CA, 1999.

[81] Welch, P.D., "The Use of Fast Fourier Transform for the Estimation of Power Spectra: A Method Based on Time Averaging Over Short, Modified Periodograms." *IEEE Transactions on Audio Electroacoustics*, Vol. AU-15, pp. 70-3, June 1967.

[82] Futierrez-Osuna, R., "Dimensionality Reduction (PCA)." in lecture 5 from course motes to Introduction to Pattern Recognition, Write State University, Dayton, OH, 2004.

[83] Lew, J.S., "Using Transfer Function Parameter Changes for Damage Detection of Structures." *AIAA Journal*, Vol. 33, No. 11, pp. 2189-93, November 1995.

[84] Somol, P., Pudil, P., Novovicova, J., and P. Paclik, "Adaptive Floating Search Methods in Feature Selection." *Pattern Recognition Letters*, Vol. 20, pp. 1159-63, 1999.

[85] Jain, A., and D., Zongker, "Feature Selection: Evaluation, application and small sample performance." *IEEE Transactions on Pattern Analysis and Machine Intelligence*, Vol. 19, 153-8, 1997.

[86] Oppenheim, A.V., and R.W. Schafer, *Digital Signal Processing*. Prentice-Hall, Englewood Cliffs, NJ, 1975.

[87] Hayes, M., *Statistical Digital Signal Processing and Modeling*. John Wiley & Sons, New York, 1996.

[88] Stoica, P., and R.L. Moses, *Introduction to Spectral Analysis*. Prentice-Hall, Englewood Cliffs, NJ, 1997.

[89] Guratzsch, R.F., and S. Mahadevan, "Feature Extraction and Selection Algorithms for Structural Damage Detection." submitted for review to *Structural Control & Health Monitoring*, June 27, 2006.

[90] Johnson, N.L., Kotz, S., and A.W. Kemp, *Univariate Discrete Distributions*. 2nd Ed., John Wiley & Sons, New York, pp. 129-32, 1992.

[91] Hiramoto, K., Doki, H., and G. Obinata, "Optimal sensor/actuator placement for active vibration control using explicit solution of algebraic Riccati equation." *Journal of Sound Vibration*, Vol. 229, No. 5, pp. 1057-75, 2000.

[92] Abdullah, M., Richardson, A., and J. Hanif, "Placement of sensor/actuators on civil structures using genetic algorithms." *Earthquake Engineering & Structural Dynamics*, Vol. 30, pp. 1167-84, 2001.

[93] Yan, Y.J., and L.H. Yam, "Optimal design of number and locations of actuators in active vibration control of a space truss." *Smart Materials & Structures*, Vol. 11, No. 4, pp. 496-503, 2002.

[94] Simpson, M.T., and C.H. Hansen, "Use of genetic algorithms to optimize vibration actuator placement for active control of harmonic interior noise in cylinder with floor structure." *Journal of Noise Control Engineering*, Vol. 44, pp. 169-84, 1996.

[95] Peng, F., "Actuator Placement Optimization and Adaptive Vibration Control of Plate Smart Structures." *Journal of Intelligent Material Systems and Structures*, Vol. 16, No. 3, pp. 263-71, 2005.

[96] Demetriou, M.A., "Integrated Actuator-Sensor Placement and Hybrid Controller Design of Flexible Structures Under Worst Case Spatiotemporal Disturbance Variations." *Journal of Intelligent Material Systems and Structures*, Vol. 15, No. 12, pp. 901-21, 2004.

[97] Guo, H.Y., Zhang, L., Zhang, L.L., and J.X. Zhou, "Optimal placement of sensors for structural health monitoring using improved genetic algorithms." *Smart Materials & Structures*, Vol. 13, pp. 528-34, 2004.

[98] Spanache, S., Escobet, T., and L. Trave-Massuyes, "Sensor Placement Optimization Using Genetic Algorithms." in proceedings of 15th International Workshop on Principles of Diagnosis, Carcassonne, France, June 23-25, 2004.

[99] Gao, H., and J.L. Rose, "Sensor placement optimization in structural health monitoring using genetic and evolutionary algorithms." in proceedings of SPIE Smart Structures and Materials, San Diego, CA, February 26, 2006.

[100] Li, D., Li, H., and C.P. Fritzen, "A New Sensor Placement Algorithm in Structural Health Monitoring." in proceedings of 3rd European Workshop on Structural Health Monitoring, Granada, Spain, July 5-7, 2006.

[101] Gao, H., and J.L. Rose, "Ultrasonic Sensor Placement Optimization in Structural Health Monitoring Using Evolutionary Strategy." in proceedings to AIP Conference on Quantitative Nondestructive Evaluation, Vol. 820, pp. 1687-93, March 6, 2006.

[102] Dhillon, S.S., Chakrabarty, K., and S.S. Iyengar, "Sensor placement for grid coverage under imprecise detection." in proceedings of International Conference on Information Fusion, Annapolis, MD, July 7-11, 2002.

[103] Lim, K.B., "A Disturbance Rejection Approach to Actuator and Sensor Placement." *Journal of Guidance, Control and Dynamics*, Vol. 20, No. 1, pp. 202-4, January-February 1997.

[104] Padula, L.S., and R.K. Kincaid, "Optimization Strategies for Sensor and Actuator Placement." NASA TM-1999-209126, April 1999.

[105] Padula, L.S., and R.K. Kincaid, "Optimal Sensor/Actuator Locations for Active Structural Acoustic Control." in proceedings of 39th AIAA/ASME/ASCE/AHS/ASC Structures, Dynamics and Materials Conference, Long Beach, CA, April 20-23, 1998.

[106] Padula, L.S., and R.K. Kincaid, "Aerospace Applications of Integer and Combinatorial Optimization." NASA TM-110210, October 1995.

[107] Raich, A.M., and T.R. Liszkai, "Multi-Objective Genetic Algorithm Methodology for Optimizing Sensor Layouts to Enhance Structural Damage Detection." in proceedings of 4th International Workshop on Structural Health Monitoring, Stanford, CA, September 15-17, 2003.

[108] Spall, J.C., "An Overview of the Simultaneous Perturbation Method for Efficient Optimization." *Johns Hopkins APL Technical Digest.* Vol. 19, No. 4, pp. 482-92, 1998.

[109] Glover, F., and M. Laguna, *Tabu Search.* Kluwer Academic Publishers, Boston, 1997.

[110] Royset, J.O., Der Kiureghian, A., and E. Polak, "Reliability-based optimal structural design by the decoupling approach." *Reliability Engineering & System Safety,* Vol. 73, pp. 213-21, 2001.

[111] The MathWorks, Inc., *MATLAB Version 7.0.4.365 (R14) Service Pack 2*, January 29, 2005.

[112] Blackshire, J.L., Martin, S., and A. Cooney. "Characterization and Modeling of Bonded Piezoelectric Sensor Performance and Durability in Simulated Aircraft Environments." in proceedings of 3rd European Workshop on Structural Health Monitoring, Granada, Spain, July 5-7, 2006.

[113] Crawley, E.F., and J. de Luis, "Use of Piezoelectric Actuators as Elements of Intelligent Structures." *AIAA Journal*, Vol. 25, pp. 1373-85, 1987.

[114] Park, C., Walz, C., and I. Chopra, "Bending and Torsion Models of Beams With Induced-Strain Actuators." *Smart Materials and Structures*, Vol. 5, pp. 98-113, 1996.

[115] Sirohi, J., and I. Chopra, "Fundamental Understanding of Piezoelectric Strain Sensors." *Journal of Intelligent Materials, Systems, and Structures*, Vol. 11, pp. 246-57, 2000.

[116] Saint-Pierre, N., Jayet, Y., Perrissin-Fabert, I., and J.C. Baboux, "The Influence of Bonding Defects on Electric Impedance of Piezoelectric Embedded Element." *Journal of Physics D*, Vol. 29, pp. 2976-82, 1996.

[117] Giurgiutiu, V., Zagarai, A., and J.J. Bao, "Piezoelectric Wafer Embedded Active Sensors for Aging Aircraft Structural Health Monitoring." *International Journal of Structural Health Monitoring*, Vol. 1, pp. 41-61, 2002.

[118] Sun, D., and L. Tong, "Closed-Loop Based Detection of Debonding of Piezoelectric Actuator Patches in Controlled Beams." *International Journal of Solids and Structures*, Vol. 40, pp. 2449-71, 2003.

[119] Park, G., Farrar, C.R., Rutherford, A.C., and A.N. Robertson, "Piezoelectric Active Sensor Self-Diagnostics Using Electrical Admittance Measurements." *Journal of Vibration and Acoustics*, Vol. 128, pp. 469-76, 2006.

[120] DeSimio, M., Olson, S., and M. Derriso, "Decision Uncertainty in a Structural Health Monitoring System." in proceedings of SPIE Smart Structures and Materials 2005: Smart Structures and Integrated Systems, Vol. 5764, pp. 530-41, 2005.

[121] Olson, S.E., DeSimio, M.P., and M.M. Derriso, "Structural Health Monitoring Incorporating Temperature Compensation." in proceedings of 5th International Workshop on Structural Health Monitoring, Stanford, CA, September 12-14, 2005.

[122] Kaljevic, I., and S. Saigal, "Stochastic boundary elements for two-dimensional potential flow in non-homogeneous media." *Computer Methods in Applied Mechanics and Engineering*, Vol. 121, No. 1-4, pp. 211-30, 1995.